Safety in Mines Research Advisory Committee

Final Project Report

The meaningful use of peak particle velocities at excavation surfaces for the optimisation of the rockburst criteria for tunnels and stopes

A.M. Milev, S.M. Spottiswoode, B.R. Noble, L.M. Linzer, M. van Zyl, A. Daehnke & E. Acheampong

Research agency: CSIR: Division of Mining Technology

Project number: GAP 709

Report number: 2002 - 0305

Date: March 2002

Executive Summary

The aim of this project is optimisation of rockburst support systems by the systematic evaluation and quantification of the peak particle velocity recorded underground. To achieve this goal, a number of research tasks were carried out.

(i) Development and manufacture of a Peak Particle Velocity (PPV) measuring instrument.

A cost-effective instrument especially designed for recording strong ground motion was developed and manufactured. The instrument, a Peak Velocity Detector (PVD), is a portable battery powered stand-alone device with backed-up memory capable of storing up to 512 peak particle velocities for the largest excursion exceeding some threshold during each time window of 25 seconds. Five parameters are stored per event: peak particle velocities; time of the peak; slope at the first zero crossing; slope at the second zero crossing; and peak width, measured between the nearest zero crossings - before and after.

(ii) An enlarged database of measured PPVs in stopes and tunnels in various geotechnical areas was accumulated.

Extensive underground seismic measurements at Carbon Leader Reef and Ventersdorp Contact Reef sites were carried out. A total number of 41 sites were monitored:

- TauTona gold mine: a total number of 15 139 seismic events with a maximum PPV of 3 m/s was recorded during 2 437 site days;
- Kloof gold mine: a total number of 6 066 seismic events recorded during 659 site days with a maximum PPV of 3 m/s; and
- Mponeng gold mine: a total number of 1183 seismic events recorded during 403 site days with a maximum PPV of 2.3 m/s.

(iii) Back-analyses of mine network data to derive the velocity amplification factors on the skin of the excavations were conducted.

The site response obtained at the surface of excavations was found to attenuate with the hypocentral distance. The exponential attenuation of the following type;

$$x = a\,e^{-bR}$$

where *a* and *b* are coefficients different for the different geotechnical areas; is proposed. However, due to the limited number of seismic events correlated at hypocentral distances longer then 500 m, the correlation coefficient for the exponential trend line is very low.

The relationship between the site response and additional seismological parameters, such as hypocentral distance, source radius, wavelength (Lambda) and maximum velocity are discussed in this report. In addition, the relationship between source radius and hypocentral distance, and source radius and magnitude was outlined in an attempt to characterise the comprehensive rock mass behaviour under dynamic loading.

(iv) A statistical procedure to estimate the probability of the occurrence of a particular PPV, was applied.

The maximum likelihood curve fits, using a maximum and a minimum, appeared to match the data recorded at TauTona very well, whereas the trend calculated using just the minimum predicted unrealistically high PPVs.

The curve fits to PPV data recorded at Kloof and Mponeng were less satisfactory, particularly towards the high end of the velocity range. This is possibly as a result of the recording period being four to six times lower than that of TauTona.

The maximum expected PPVs estimated using the maximum likelihood approach (with a minimum and a maximum) were 3 548 mm/s at TauTona; 3 311 mm/s at Kloof and 3 162 mm/s at Mponeng.

The frequency-log (PPV) distributions for Kloof and Mponeng appeared to be bimodal. The source of the bimodality is not known, and could be an effect introduced by the instrumentation or an indication of a fundamental difference in the physical mechanism of failure. It is strongly suggested that further work be done to investigate the source of the bimodality so that the appropriate statistics can be applied.

(v) Investigation was conducted into improved rockburst support criteria (in addition to the PPV criterion) for stopes and tunnels.

A rockburst model, which takes the discontinuous nature of the hangingwall into account, was developed. The model focuses on the stress changes caused by the passage of Rayleigh waves along a stope. The importance of maintaining horizontal compressive stress, to ensure hangingwall stability, is emphasised.

(vi) The PPV results and the improved rockburst support criteria were applied to formulate a new rockburst support design methodology.

The velocity criterion of 3 m/s was found to be an adequate value to meet the requirements of support systems during a rockburst. In general, the present support systems and technologies do not need to be modified significantly to cater for rockfall and rockburst conditions.

A new physical model explaining the near-field and far-field distribution of the strong ground motion was proposed.

An Improved Stope Support Design Methodology (ISSDM) was developed for rockburst conditions combining zones of support influence with hangingwall stability controlled by buckling, rotating and shearing keyblocks and the physical processes during the interaction between the hangingwall and propagating Rayleigh waves.

Preface

The knowledge gained during the course of this study was used in the development of extended support design methodology and an alternative rockburst model. An M.Sc. thesis was successfully completed on this topic (Van Zyl, M. 2001. Development of an Extended Support Design Methodology and Alternative Rockburst Model. M.Sc. research project, the University of the Witwatersrand).

The results and the key findings of this project will be disseminated through the publication of papers co-authored by the mine personnel of TauTona, Kloof and Mponeng gold mine. Three prospective papers have been outlined:

> Milev, A.M., Murphy S.K., Spottiswoode, S.M. 2002. Evaluation of the nature and the magnitude of the site response on the skin of the underground mining excavations at TauTona mine, Int. J. of Rock Mechanics and Mining Sci. & Geomech. Abstr., in preparation.
>
> Milev, A.M., Geyser, D., 2002. Some insights on peak particle velocities measured in seismically active areas at Kloof gold mine. Journal of The South African Institute of Mining and Metallurgy, proposed.
>
> Milev, A.M., Ward, A. 2002 Dynamic behaviour of underground mining workings exposed to strong ground motion. Journal of The South African Institute of Mining and Metallurgy, proposed.

Acknowledgements

The authors of this report would like to express their thanks to SIMRAC for financial support and their encouragement. To the rock engineering staff of the following mines we wish to express our sincere appreciation for their assistance and co-operation:

- TauTona mine
- Kloof mine
- Mponeng mine
- East Driefontein mine, # 1 Shaft

The authors would like to thank Mr A.J. Jager, Dr M.K.C. Roberts and Dr J.A.L. Napier for their review and valuable technical suggestions.

Table of contents

List of figures

Page

List of tables

Page

Glossary of abbreviations, symbols, terms and definitions

A = amplitude of P-wave potential

a = particle acceleration

B = amplitude of S-wave potential

C_R = Rayleigh wave velocity

C_S = S-wave velocity

H = keyblock height

k = Rayleigh wave number

L = length of block

g = acceleration due to gravity

PPV = peak particle velocity

S = maximum unsupported span = width of block

u = particle displacement

v	=	wave velocity
W	=	weight of the keyblock
ε	=	strain
ϕ	=	potential for p wave
μ_f	=	coefficient of friction
μ	=	modulus of rigidity
$\boldsymbol{k}$	=	force-correction
λ	=	Lame's constant
σ	=	stress
σ_x	=	*in situ* compressive stress
σ_{11}	=	stress associated with Rayleigh wave
σ_h	=	resultant horizontal stress
ρ	=	density of rock
ω	=	angular frequency
ψ	=	potential for S-wave
$\boldsymbol{x}$	=	site response attenuation

1 Introduction

1.1 Motivation

In seismic and rockburst-prone mines, sudden fault rupture or the failure of highly strained rock leads to energy being radiated in the form of seismic waves. The seismic waves interact with mining excavations, leading to interface and surface waves, energy channelling and wave focussing. The rock is subjected to rapid accelerations, resulting in rock-fabric failure, keyblock ejection and stope closure.

The most widely used support design criterion for rockburst-prone mines is based on work of Wagner (1984), which takes into account the kinetic and gravitational potential energy of the keyblocks. The criterion for effective rockburst-resistant support systems is to absorb the kinetic and potential energy (Roberts, 1999) associated with the hangingwall moving with an initial velocity of 3 m/s. Previously it was assumed that during a rockburst the hangingwall must be brought to rest within 0.2 m of downward movement.

The energy-absorption requirements of a support system are linearly related to the downward hangingwall displacement, and are a function of the square of the peak particle velocity (PPV). Therefore, a comparatively small decrease in peak particle velocity results in a large decrease in the energy-absorption requirements of a rockburst-resistant support system. For example, if the velocity criterion is decreased from 3 m/s to 2 m/s, the energy-absorption requirement is decreased from 20.93 KJ/m^2 to 12.83 KJ/m^2 (assuming a maximum allowable displacement of 0.2 m and a fallout height of 1.2 m). As a result, a decrease in peak particle velocities would allow for considerably lower energy-absorption demands on rockburst-resistant support systems.

A number of studies on peak particle velocities and site response were conducted in two previous SIMRAC projects, GAP 201 and GAP 530 (‘Improvement of worker safety through the investigation of site response to rockbursts’). Many important results were obtained. For example, it was found that the peak particle velocity on the skin of the excavation may be larger by four to ten times than the PPV at a point in solid rock at a similar distance from the source. In addition, points less than a metre apart show differences in amplitude and phase, which can only be accounted for by large strain across fractures.

A simulated rockburst experiment on the wall of an underground tunnel showed that peak particle velocities of 3.3 m/s measured on the blasting wall had affected, but not totally destroyed, the existing tunnel support (Milev et al., 2001). Because of insufficient data regarding the peak particle velocities on the skin of stopes, limited success was achieved in the measurement of large peak particle velocities, generated by mining induced seismic events, and quantifying the effect on the existing support system. As a result, much scope exists for improved understanding of support behaviour under extreme seismic loading.

Up to now, however, no systematic investigations have been conducted to relate practical and theoretical findings, and to quantify the risk implications of a modified velocity criterion.

The aim of this study is to systematically evaluate the peak particle velocity variations over a number of geotechnical areas, and to improve the velocity criterion, thereby increasing safety in the work place and allowing for the optimisation of rockburst support systems.

1.2 Project outputs

The primary output is optimisation of the velocity criterion for rockburst-resistant support systems by the systematic evaluation and quantification of peak particle velocities during dynamic events in various geotechnical areas.

Other outputs include:

- Development and manufacture of a PPV measuring instrument. The comparatively low cost of the instrument will enable the wide deployment thereof.

- Enlarged database of measured PPVs in stopes and tunnels in various geotechnical areas and an analysis of the support behaviour in these situations.

- Back-analyses of mine network data to derive the velocity amplification factors on the skin of the excavations and to derive the scaling equations between the PPVs measured in the stope or tunnel vicinity and the PPVs measured by the mine network.

- Application of a statistical procedure to estimate the probability of the occurrence of a particular PPV.

- Investigation into improved rockburst support criteria (in addition to the PPV criterion) for stopes and tunnels.

- Application of the PPV probability results and improved rockburst support criteria to formulate a new rockburst support design methodology.

1.3 Structure of the report

Section 1 is the introduction including the motivation, project outputs, and structure of the report.

Section 2 describes development and manufacture of a peak particle velocity measuring instrument. This includes: a preliminary analysis to determine the specifications for the instrument; a description of the instrument; laboratory and underground testing; and an analysis to ensure the quality of the data.

Section 3 describes the properties of a large database of PPVs measured in different geotechnical areas during the course of this project. The power-law of distribution of PPVs for each monitored area is outlined in this section.

Section 4 describes the results of back-analyses of mine network seismic data to derive the site response for different geotechnical areas. The site response scaling equations as a function of the hypocentral distance was derived in this section.

The relationship between the site response and other relevant seismological parameters, such as source radius, hypocentral distance, magnitude, PPV and wavelength, is also highlighted.

Section 5 describes a statistical procedure used to enhance the distribution of the extreme values and calculate the annual probability of occurrence of potentially damaging PPVs.

Section 6 describes a new innovative model of hangingwall stability based on the Rayleigh wave interaction with the surface of underground excavations. A review and evaluation of the dynamic response of support systems used in stopes and tunnels is also included.

Section 7 describes a new rockburst support design methodology based on the probability results and the model of Rayleigh wave interaction with the hangingwall.

Section 8 contains conclusions and recommendations.

2 Development and manufacture of the peak particle velocity measuring instruments

2.1 Preliminary analysis of the existing data sets recorded in stopes and tunnels to determine the specs of the instrument

Preliminary analyses were carried out to estimate the amplitude and frequency ranges on the existing data set of several thousand events recorded underground.

The existing underground data previously recorded using the Ground Motion Monitor (GMM) under project GAP 615 were analysed. Most of the data were recorded in the stopes at about 10 m from the face. The dynamic limitations of the GMM were partially reduced by applying a correction for the saturated traces using the algorithm proposed and tested by Spottiswoode, 1997 (GAP 201).

The cumulative number of events is plotted in Figure 2.1 as a function of the peak particle velocities.

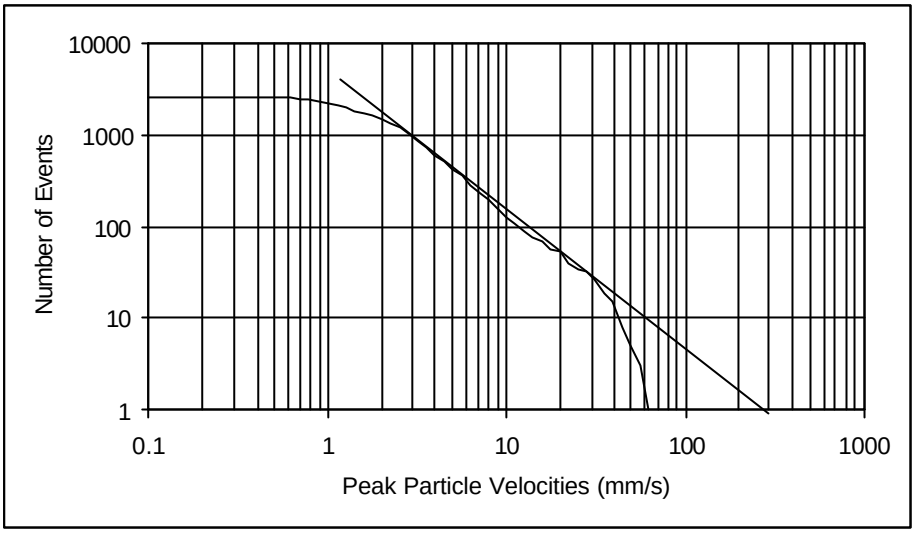

Figure 2.1 Peak particle velocities recorded by GMM at TauTona mine during a period of four months

It can be seen from Figure 2.1 that the maximum-recorded PPVs is 70 mm/s. This value is well below the velocity criterion of 3 m/s used in support design. To fulfil the requirements of this study, a further expansion of dynamic range between 0.015 m/s and 4 m/s was proposed.

To estimate the frequency range for the new instrument, the peak accelerations were plotted as a function of peak velocities. The results are shown in Figure 2.2.

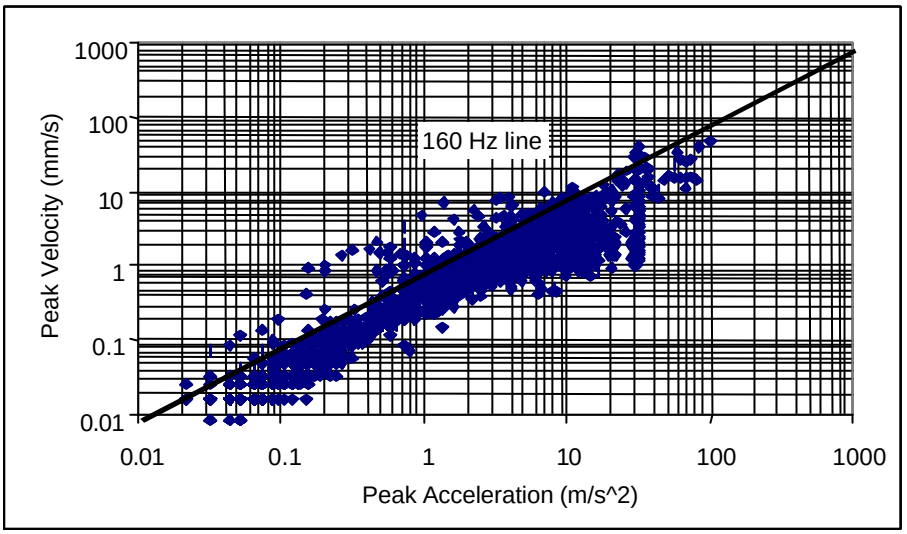

Figure 2.2 Frequency ranges for the seismic events recorded at TauTona mine during a four-month period. The relationship $w = a_{max} / v_{max}$ was used to calculate the frequency ranges

It was found that most of the events plotted around the f = 160 Hz (ω = 1000 $^{s-1}$) line and the overall frequency ranged between 30 Hz and 800 Hz. It was suggested, therefore, that geophones with a natural frequency of 14 Hz or 28 Hz could be used to cover this frequency range.

2.2 Feasibility study of the application of shockwatch devices in underground conditions

The Shockwatch is a simple, relatively cheap device used in the shipping industry to indicate specified levels of accelerations. The applicability of these devices was studied by comparing the specifications of the shockwatch devices with the level of the vibrations normally recorded underground. Two devices were found to have ranges close to the expected vibrations generated underground by strong mining tremors: Shockwatch type 85 and the MAG 2000. The critical accelerations and velocities required triggering of the Shockwatch type 85 and the MAG 2000 monitors were calculated, and are shown in Figure 2.3.

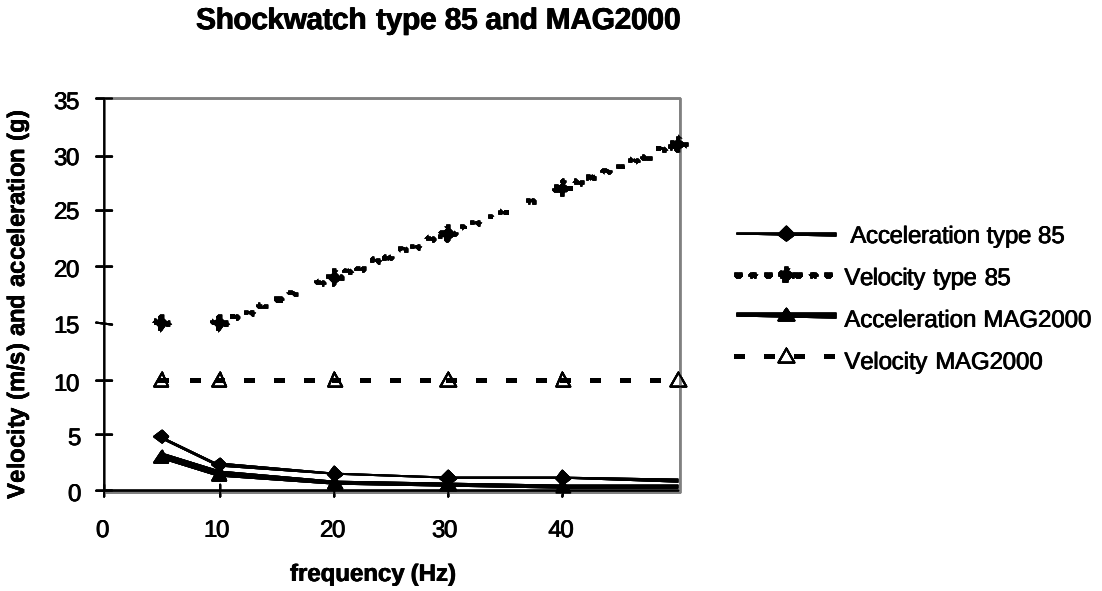

Figure 2.3 Critical accelerations and velocities required for triggering the Shockwatch type 85 and the MAG 2000 monitors as a function of frequency

As is evident from Figure 2.3, the sensitivity of the shockwatch devices is not sufficient to trigger on small and intermediate ground motions. However, they may respond well to large magnitude rockbursts. A number of shockwatches type 85 was installed underground at panel E2, Level 102 and Panel E1, Level 94, TauTona. The installation was done on the Peak Velocity Detector (PVD) described below. In this way, the range of PPVs associated with triggering of the shockwatch could be estimated. One out of four shockwatches went off during the experiment. However, the maximum PPV recorded at this site was 342 mm/s, well bellow the shockwatches trigger level shown in Figure 2.3. Therefore, it was assumed that additional factors like high pressure and high temperature were the reason for triggering, rather than the PPVs. It was also found that all types of shockwatches are very difficult to transport underground as many of them went off during the shipping to the site.

2.3 Development and manufacturing of a cost-effective instrument for recording large peak particle velocities in various geotechnical areas

A cost-effective instrument especially designed for recording of strong ground motion was developed and manufactured: a Peak Velocity Detector (PVD). The instrument measures the peak particle velocity of a seismic wave propagating underground.

The PVD is a portable battery powered stand-alone device with backed-up memory capable of storing up to 512 peak particle velocities for the largest excursion exceeding some threshold during each time window of 25 seconds. Five parameters are stored per event:

- peak particle velocities;
- time of the peak;
- slope at the zero crossing immediately before the peak;
- slope at the zero crossing immediately after the peak; and
- peak width, measured between the nearest zero crossings - before and after.

These parameters also enable the estimation of frequency, ground accelerations and displacement. The corresponding times were used to link the recorded peak particle velocities to data recorded by ground motion monitors and mine seismic networks.

An important feature of the PVD is the “graceful decline” – an overwriting procedure whereby once the memory is full the incoming pulses overwrite the existing pulses only if they are larger. This will shift the minimum record of the recorded data towards the stronger ground motions without missing larger events.

A diagram of the PVD construction is shown in Figure 2.4.

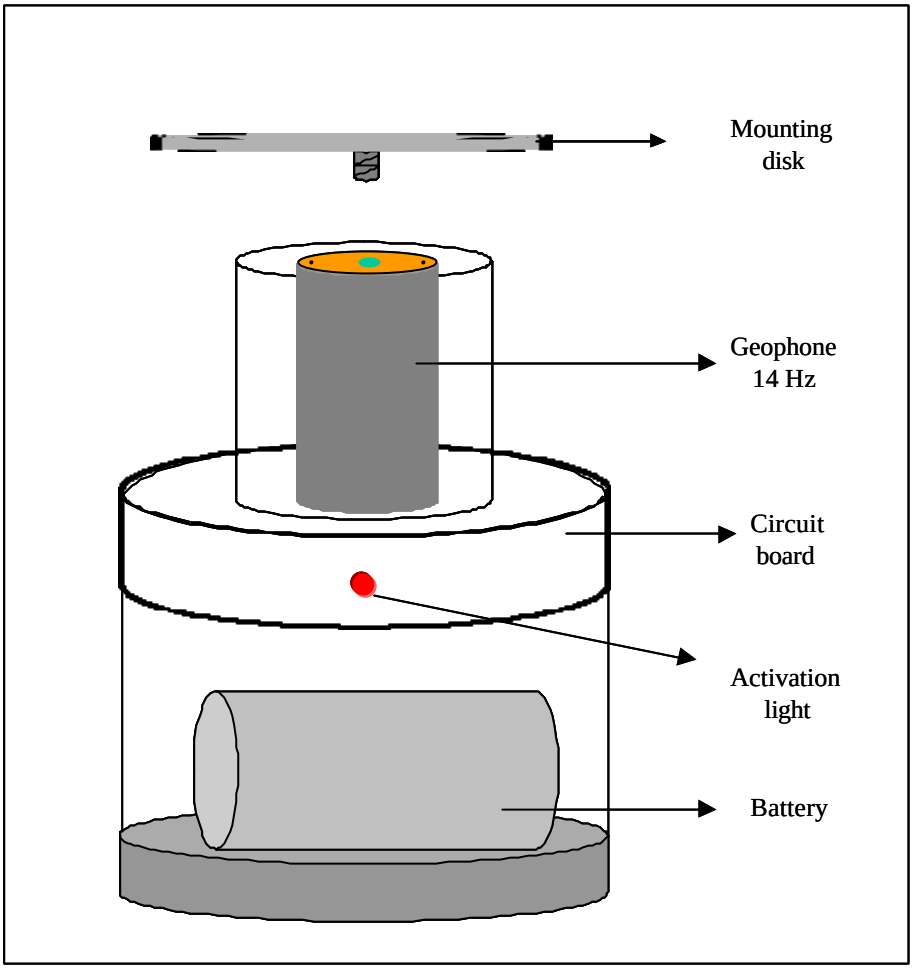

Figure 2.4 Peak Velocity Detector

The block diagram of the Peak Velocity Detector is shown in Figure 2.5.

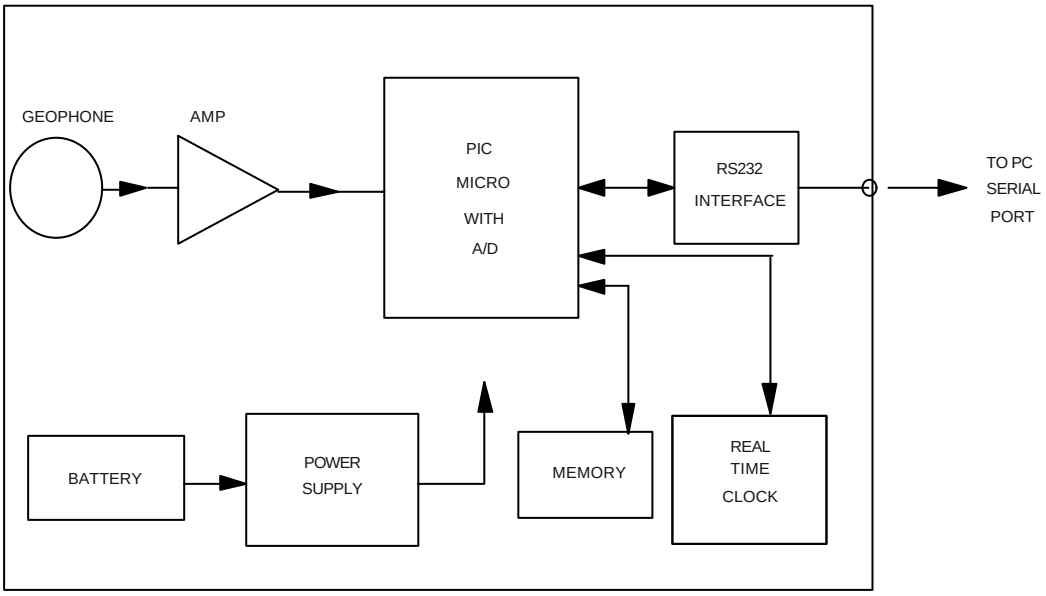

Figure 2.5 Principle diagram of the Peak Velocity Detector

During the processes of underground monitoring, an additional improvement of the PVD was made: the time history of the strongest seismic event in a particular data set could now be stored. This process has a potential advantage of enormously improving the quality of data recorded without severely reducing the total number of events.

2.4 Laboratory and underground testing of the PPV recording instrument

The geophone transducers type HS-J 28 Hz were excited on a vibration shaker that was controlled with a signal generator. A calibrated accelerometer was placed on the shaker next to the transducers to determine the actual excitation parameters for each test.

All transducers were excited at 25 Hz with an amplitude of approximately 40 mm/s for a full 25-second monitoring period. Two transducers were also excited at various amplitudes at this frequency to determine the linearity of the response of the units. The amplitudes were also varied at 25, 70, and 160 Hz to determine the maximum amplitude the transducer could measure before physical saturation took place. To determine the frequency response over the operating frequency range the transducers were tested from a frequency of 4 Hz to 512 Hz. An engineering unit defined as Volt (V) per velocity unit (m/s) was calculated.

Figure 2.6 displays the engineering unit and frequency variation for various amplitudes of excitation. The frequency has been determined from the period dT and the threshold-crossing values stored during the test.

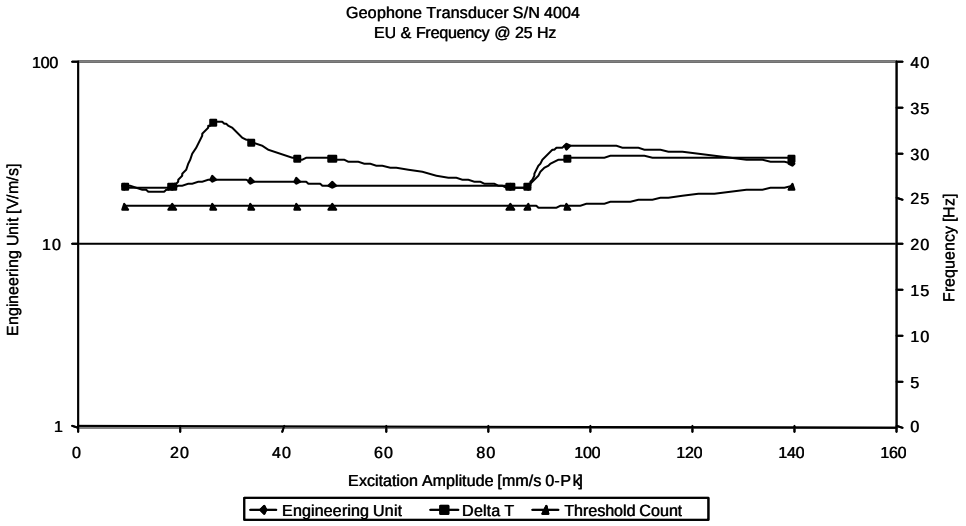

Figure 2.6 Engineering unit within a frequency range versus excitation amplitude

The frequency response of the transducers (in this case Unit 4004) is depicted in Figure 2.7.

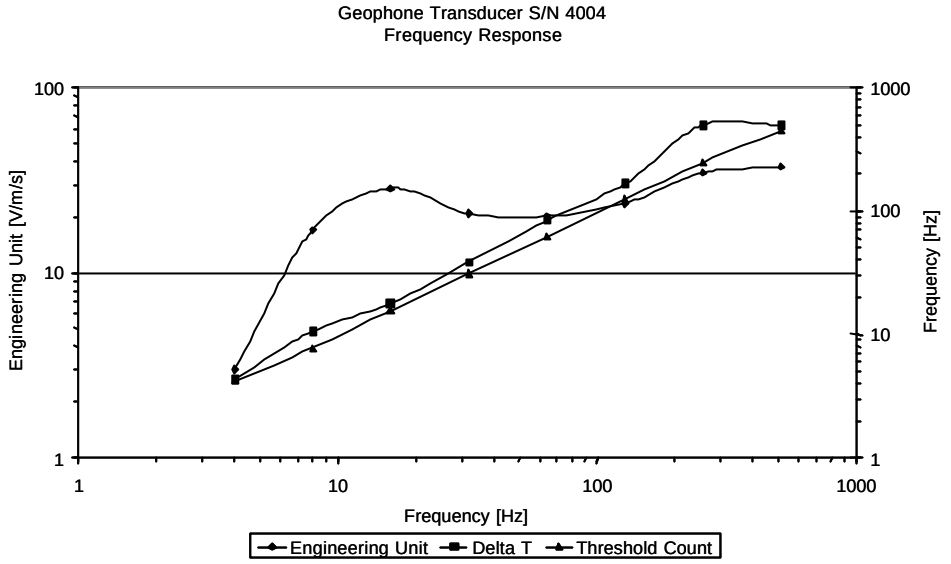

Figure 2.7 Frequency response and frequency check

The calibration procedure shows that all units determined the amplitude of response reasonably consistently. The units show saturation at approximately 87 mm/s. It is not certain whether the actual magnet in the geophone was striking the ends of the casing, or if this was due to some other mechanism, e.g. over-excitation of the main power switch. The physical saturation levels monitored are subjective, as this is based on where the unit starts emitting a noise that sounds like the magnet inside the geophone impacting on the ends of the transducer. Thereafter, 14 Hz geophones were recommended due to the longer distance of movement (up to 4 mm) of the magnet before it reaches the stop and the stiffer spring supporting the magnet.

The PVD was tested underground in Kloof gold mine. Figure 2.8 shows the underground site.

Figure 2.8 Underground site in Kloof gold mine illustrating the installation of the PVD

In addition, a Groung Motion Monitor (GMM) was installed in close proximity and the recordings of the PVD and the GMM were compared.

2.5 Analysis to ensure the quality of the data

The recorded values of V_{max} were verified against the calculated values of the acceleration obtained in the beginning and in the end of the peak, and the time between the crossover. A real seismogram in Figure 2.9 illustrates that a significant difference in the slopes of the peaks, marked A, B, C, and D, can occur.

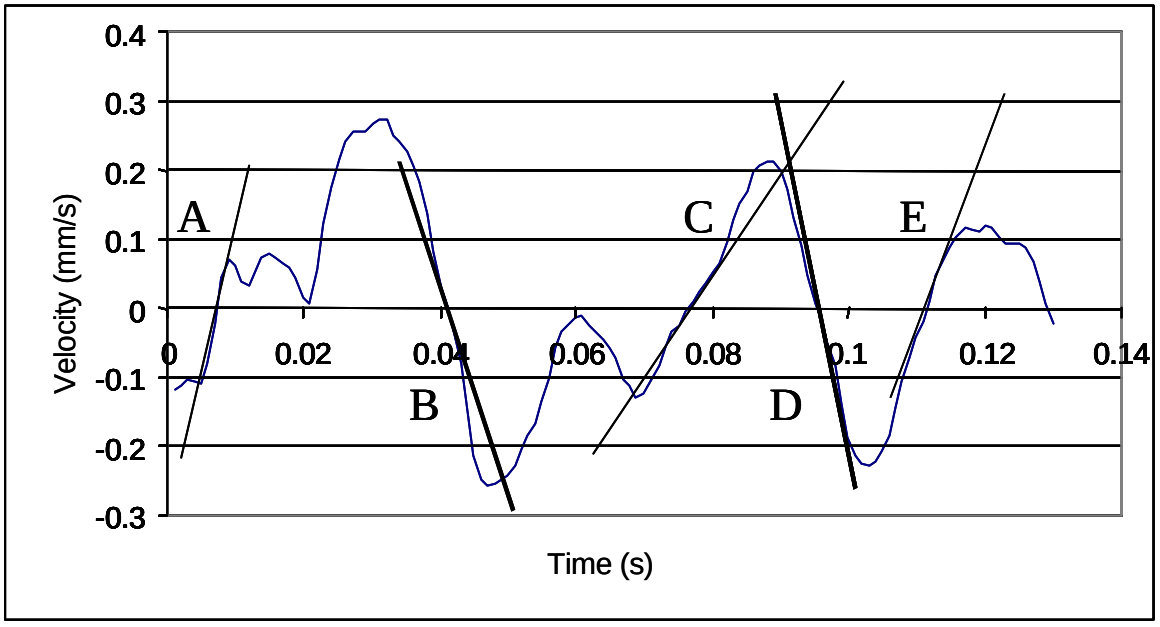

Figure 2.9 Sketch of a portion of a seismogram with zero crossings and peaks marked

The peak velocity V_{max} was calculated using the following equation:

$$V_{max} = A_{max} /(2 * \pi f) \qquad (2.4)$$

where A_{max} is the acceleration calculated from the slope of the peak, and f is frequency in Hz calculated from the half-period measured between the two zero crossings.

In the case of the pure sine wave the A_{max} would be the same whether measured before or after the peak. However, in many cases the real seismograms have complicated waveforms. As is shown in Figure 2.9, different slopes (marked A, B, C, D and E) can be identified.

The value of V_{max} measured was compared with two calculated values using equation (2.4) and the slope in the beginning and in the end of the peak. The calculated values were averaged by applying the following equation:

$$V_{\max} = 2/(1/V^{b}_{\max} + 1/V^{e}_{\max}) \quad (2.5)$$

where $V^{b}_{\max}$ is the velocity calculated from the acceleration obtained at the beginning of the peak and the $V^{e}_{\max}$ is velocity calculated from the acceleration obtained at the end of the peak. Therefore, the $V_{\max}$ was checked for consistency between calculated and measured values.

2.6 Change in specs and motivation for further improvements

The original specifications were true to the concept of a device to record PPV values for support design. However, during the interpretation of data a need to change the specification was recognised. In particular, if window over which PPV values were estimated were smaller ($T = \delta t$), than data for all the largest swings could be stored. In this case, the largest events will contain many of the largest swings. This leads to a very important question:

If $T = \delta t$, how will the peaks be distributed amongst the events with large and small ground motions?

Some suggestions to answer this question, using scaling behavior that has appeared from previous studies, are listed below.

Consider, for any seismogram:

v_e = Peak velocity of entire seismogram

v_p = Peak velocity of each positive- or negative-going pulse

v_T = Trigger threshold above which all pulses are recorded

N_p = Number of pulses for which $V_P \geq V_T$

N_s = Number of samples for which $V_P \geq V_T$

When dealing with a suite of events of all events over a period of time at any site:

N_v = is the number of seismograms from a suite of event with peak velocity >= v_T

N_{vp} = is the number of pulse for which $V_P \geq V_T$ over N_v seismograms

Numerous recordings of PPV (e.g. GAP 530 and GAP 709) have shown that:

Nv ~ VT -1 (2.6)

where "~" means "scales as".

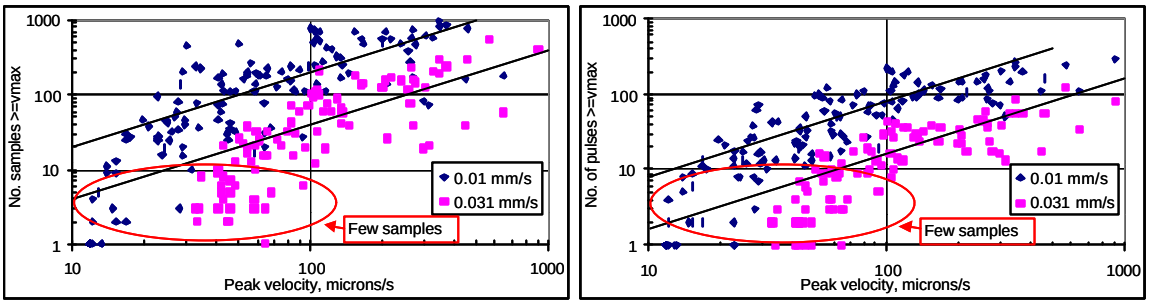

(*a*) N_S, V_e, V_p (*a*) N_P, V_e, V_p

Figure 2.10 (a, b) Number of samples greater than two amplitude values (0.01 and 0.031 mm/s) (a) and number of swings that cross the same amplitude values (b) as a function of PPV. (Data from file PRISM system at ERPM)

From Figure 2.10 (b), it can be seen that the number of pulses (N_p) within any single seismogram that cross any trigger threshold (v_T) scales as:

$$N_p \sim v_e^{+1} \qquad (2.7)$$

Actually, the scaling seems to flatten out to a slope less than 1 at higher peak velocities (v_p) in Figure 2.10 (*b*), whereas the plot in Figure 2.10 (*a*) with the number of samples persists with a slope of 1 at higher v_p. The lower slope for higher v_p in Figure 2.10 (*b*) can be attributed to the lower frequency content of seismograms from larger events.

From equations (2.6) and (2.7),

$$N_{v\,p} \sim N_v * N_p \sim v_e^{\,0} \qquad (2.8)$$

Following the power-law relationships in equations (2.6) and (2.7), the logarithmic ranges of v_e will result in equal numbers of recordings. An example is given in tabular form in Table 2.1

Table 2.1 An example following the power low relationship given in equation (2.6 and 2.7)

Range of PPV	1 to 10 mm/s	10 to 100 mm/s	100 mm/s to 1 m/s
Number of events	100	10	1
Number of pulses per event	1	10	100
Number of recorded pulses	100	100	100

Current recording would result in 111 events. If every pulse is recorded, 300 events would be recorded, with the larger events recorded in much more detail. In other words, if graceful decline is activated, the smallest 100*(300-111)/300 = 63% of the current events would be overwritten. From equation (2.6), this would move the effective threshold level (v_T) up by a factor of 2.7 or 0.43 units of $\log_{10}$.

For the largest events, there might even be an opportunity to reconstruct a simplified seismogram. This could take place in several ways. For example, after a threshold has been exceeded, the time and amplitude of all peak values that exceed the threshold could be recorded until a defined window length has been reached. This would be a major departure from the current recording philosophy, but could still be used to estimate peak acceleration a_{max} and pulse half-width t_2 for the bigger events.

2.7 Conclusions

A cost-effective instrument especially designed for recording of strong ground motion was developed and manufactured.

The instrument is a portable battery powered stand-alone device with backed-up memory capable of storing up to 512 peak particle velocities. Five parameters are stored per event:

- peak particle velocities;
- time of the peak;
- slope of the peak in the beginning;
- slope of the peak in the end; and
- peak width, measured between the nearest zero crossings - before and after.

An overwriting procedure was implemented whereby once the memory is full the incoming pulses overwrite the existing pulses only if they are larger than the smaller amplitude stored in memory. Recording all the largest pulses has the potential advantage of enormously increasing the amount of data recorded from the largest events without severely reducing the number of events recorded.

A calculation procedure to verify the quality of recorded data was created. The procedure is based on a comparison of measured velocities and calculated velocities from acceleration obtained in the beginning and in the end of the peak, and the frequency calculated from the half-period measured between two zero crossings.

3 Enlarged database of measured PPVs in stopes and tunnels in various geotechnical areas and an analysis of the support behaviour in these situations

A number of studies (Wagner, 1994; McGarr et al. 1981; McGarr, 1991; Roberts, 1999) carried out during the last few decades have suggested that the peak particle velocity of 3 m/s is an appropriate value that the support systems in South African gold mines have to sustain during rapid dynamic loading. This criterion is routinely used to estimate the energy-absorption requirements for support systems in rockburst-prone mines. However, no detailed investigations

have been made to date to determine the validity of the velocity criterion across various reef types and different geotechnical areas.

One of the main objectives of this study is to create a large volume data set of PPVs measured in different geotechnical areas that can be used to re-evaluate the velocity criterion.

Extensive underground seismic measurements at Carbon Leader Reef and Ventersdorp Contact Reef sites were carried out. A total number of 41 sites located at TauTona, Kloof, Mponeng and East Driefontein gold mines were monitored. A summary of these sites is given in Table 3.1.

Table 3.1 Summary of the underground monitoring sites

Mine	Number of sites	Total recording time (site days)
TauTona	22	2 437
Kloof	10	659
Mponeng	7	403
East Driefontein # 1 Shaft	2	46

The PPVs measured at each mine were categorized in three statistical groups:

- PPVs less than 100 mm/s;
- PPVs greater than 100 mm/s; and
- PPVs greater than 800 mm/s.

The last group of seismic events was considered as damaging. The values of 100 mm/s and 800 mm/s used for definition of these groups were based on the observations obtained from the simulated rockburst experiment made under the SIMRAC project GAP 530 and published by Milev et. al, 2001. Figure 3.1 illustrates the PPVs generated by the simulated rockburst on the wall of underground tunnel.

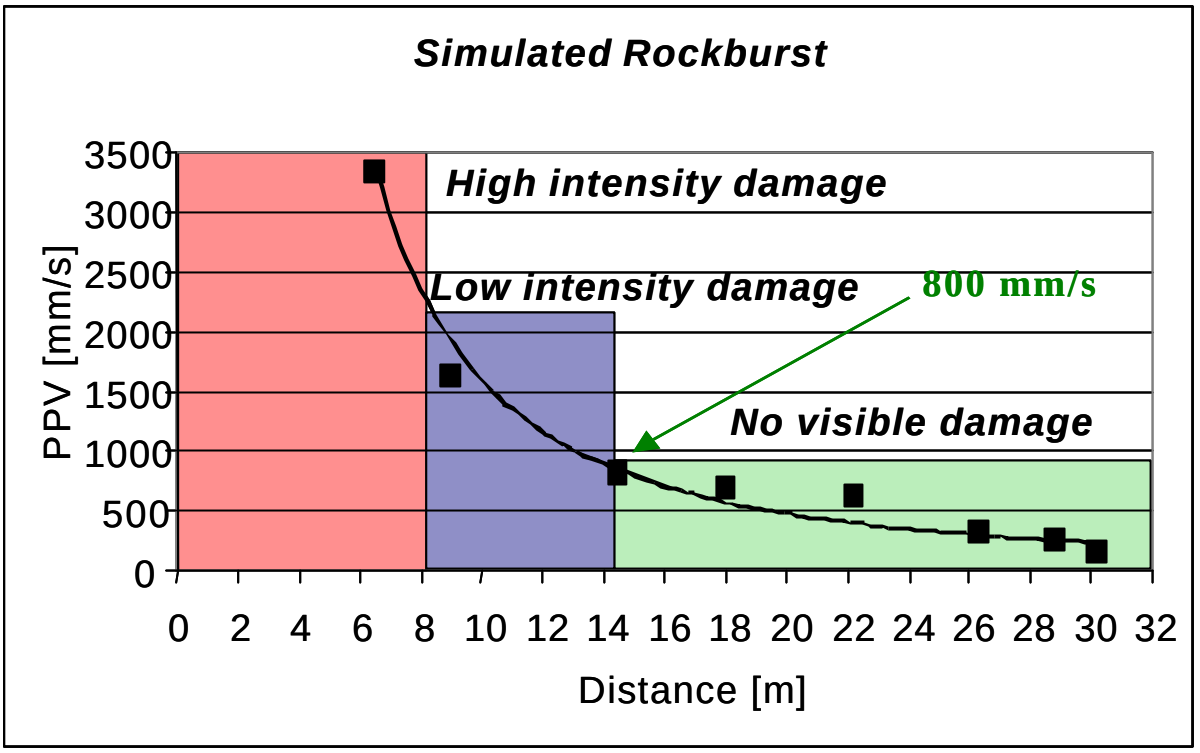

Figure 3.1 The attenuation of the PPVs in the wall of underground tunnel

The PPVs measured on the blasting wall were related to the rockburst damage. Figure 3.1 clearly indicates the areas of high and low intensity damage followed by an area where no visible damage was observed. A PPV of 800 mm/s was measured in the transition from low intensity to no rockburst damage. The value of 100 mm/s was subjectively chosen to separate the events with noticeable PPVs from the rest of the events which have an insignificant effect on the support system. However, in some isolated cases damage was observed at PPVs in the range of 100 mm/s (Mponeng gold mine; Ward, 2002).

3.1 TauTona gold mine

Twenty-two seismically active sites in five sections were instrumented following a discussion with Mr. S. Murphy, rock engineering manager, at TauTona mine. All stopes monitored were on the Carbon Leader Reef at depth ranging from 2 600 m to 3 600 m. Most of the sites were mined longwalls protected by strike stabilising pillars (SSP) and well-placed backfill.

The positions of these sites are illustrated in Figure 3.2.

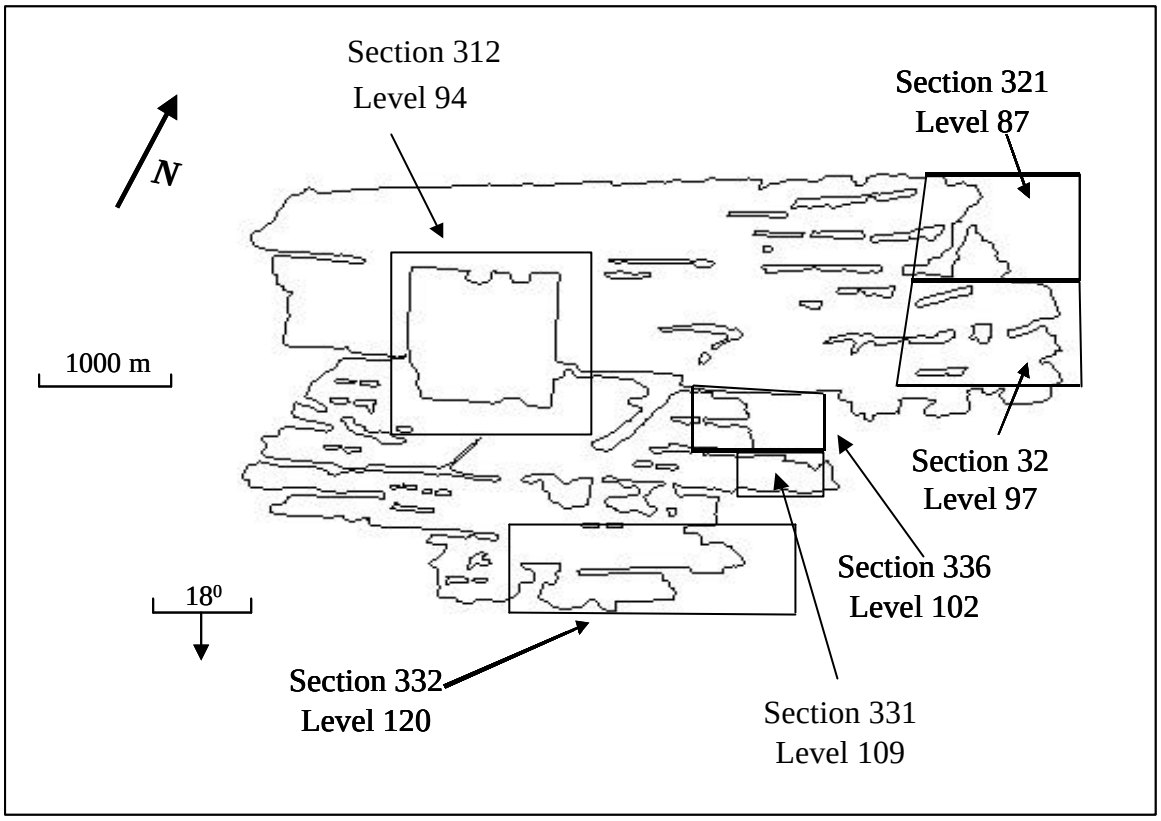

Figure 3.2 Mine-wide positions of the monitoring areas

A detailed description of the monitored panels, summary of the data collected is given in Table 3.2.

Table 3.2 The PPVs experienced at TauTona mine during the period of observation

Level	Panel	Time (days)	PPV G.T. 100 (mm/s)	PPV G.T. 800 (mm/s)	PPV (mm/s)	Beginning	End
L 87	E1	232	111	10	2 863	29-Jan-01	29-Oct-01
	E1A HW	118	39	1	931	29-Jan-01	4-Nov-01
	E1A FW	15	0	0	55	27-Sep-01	11-Oct-01
	E2	41	1	0	344	30-Jan-01	19-Apr-01
L 94	E1	162	38	6	1 980	24-Nov-00	22-Aug-01
	E2 HW	254	32	7	3 054	21-Nov-00	23-Aug-01
	E2 FW	13	5	1	783	7-Aug-01	20-Aug-01
	E3	17	1	0	163	25-Nov-00	12-Dec-00

Table 3.2 (continuation) The PPVs experienced at TauTona mine during the period of observation

Level	Panel	Time (days)	PPV G.T. 100 (mm/s)	PPV G.T. 800 (mm/s)	PPV (mm/s)	Beginning	End
L 97	E2 HW	19	1	0	165	17-Nov-01	5-Dec-01
	E2 FW	21	78	14	2820	17-Nov-01	7-Dec-01
	E3 HW	144	381	37	2036	27-Jun-01	31-Jan-02
	E3 FW	100	49	5	2174	29-Aug-01	31-Jan-02
	E5	86	393	1	1074	24-Nov-00	8-Mar-01
	E6	141	78	1	859	23-Nov-00	29-May-01
	E7	93	3	1	1384	24-Nov-00	26-Feb-01
L 102	E1	25	38	0	335	10-Dec-00	5-Jan-01
	E2	72	30	0	342	25-Jul-01	22-Oct-01
	E3 HW	82	46	8	1670	13-Aug-01	9-Jan-02
	E3 FW	86	87	12	2820	13-Aug-01	10-Jan-02
	E4 HW	95	29	14	2742	12-Dec-00	10-Jan-02
	E4 FW	15	2	0	185	25-Oct-01	10-Nov-01
L 109	Tunnel	34	7	3	2887	13-Mar-01	24-May-01
L 120	E3	207	118	9	1932	25-Jan-01	3-Nov-01
	E4	185	742	13	3029	26-Jan-01	10-Oct-01
	E5	180	127	19	2195	26-Jan-01	10-Sep-01

The results listed in Table 3.2 illustrate large variations in PPVs for the different areas. Values of up to 3 m/s were recorded at some of the areas.

The recorded PPVs are shown in a form of power-law distribution plot per monitoring area. The number of events was normalised by the period of observations and then multiplied by 365 to obtain the annual figures.

Peak particle velocities recorded for a period of 406 site days at Level 87, Panels E1, E1A HW, E1A FW and E2 are shown in Figure 3.3.

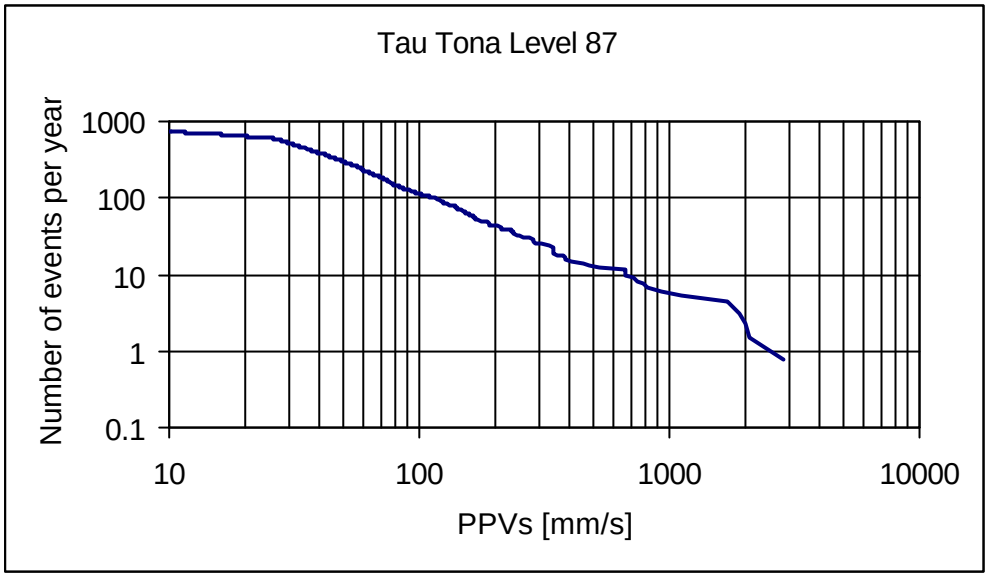

Figure 3.3 Peak particle velocities recorded at TauTona mine: Level 87, Panels E1, E1A HW, E1A FW and E2

A linear distribution of PPVs is evident from Figure 3.3. A maximum value close to 3 m/s was recorded during the monitoring period.

Peak particle velocities recorded for a period of 446 site days at Level 94, Panels E1, E2 HW, E2 FW and E3 are shown in Figure 3.4.

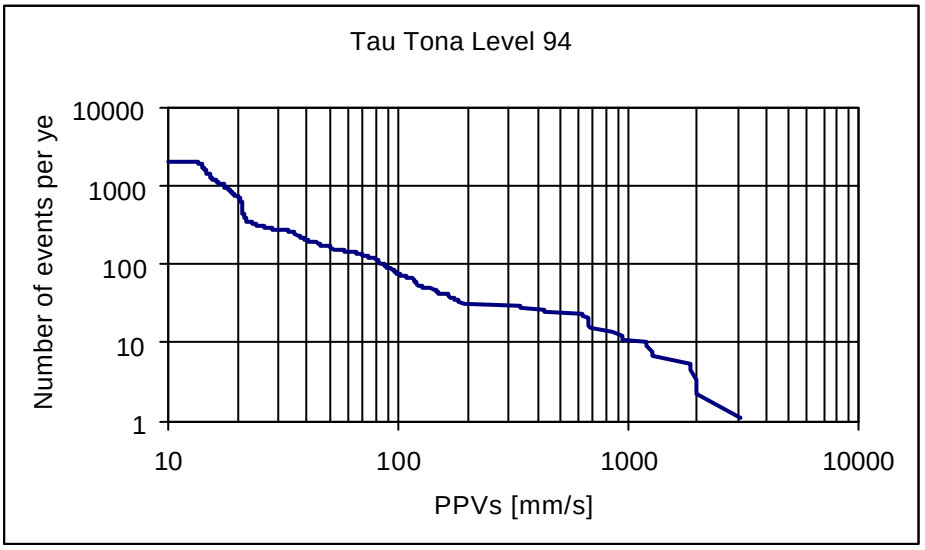

Figure 3.4 Peak particle velocities recorded at TauTona mine: Level 94, Panels E1, E2 HW, E2 FW and E3.

A linear distribution of PPVs is evident from Figure 3.4. A maximum value of 3 m/s was recorded during the monitoring period.

Peak particle velocities recorded for a period of 602 site days at Level 97, Panels E2 HW, E2 FW, E3 HW, E3 FW, E5, E6 and E7 are shown in Figure 3.5.

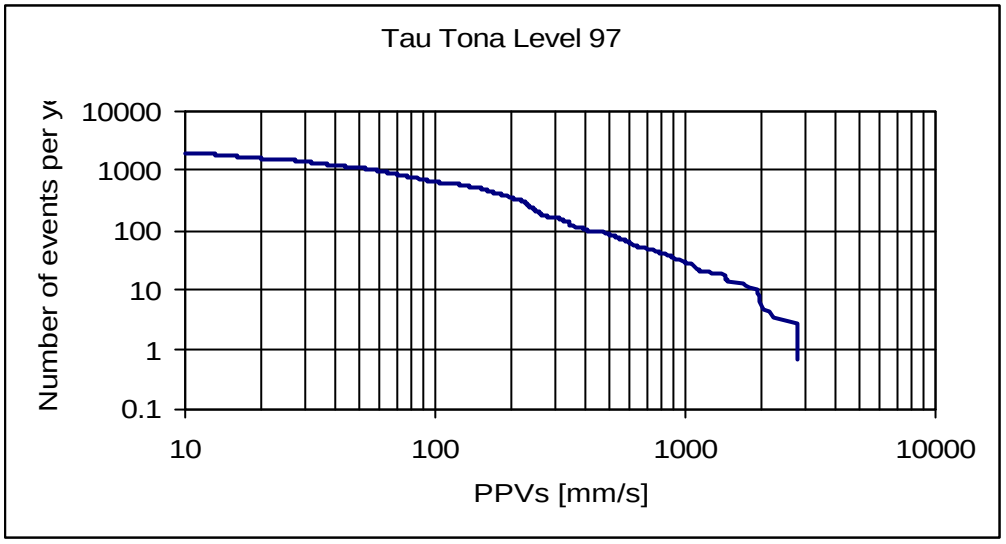

Figure 3.5 Peak particle velocities recorded at TauTona mine: Level 97, Panels E2 HW, E2 FW, E3 HW, E3 FW, E5, E6, and E7

A maximum value of about 2.8 m/s was recorded during the monitoring period (Figure 3.5). However, the data shows deviation from the linear distribution at that level.

Peak particle velocities recorded for period of 375 site days at Level 102, panels E1, E2, E3 HW, E3 FW, E4 HW and E4 FW are shown in Figure 3.6. Level 102 was mined with lagging longwalls with strike stabilising pillars and backfill.

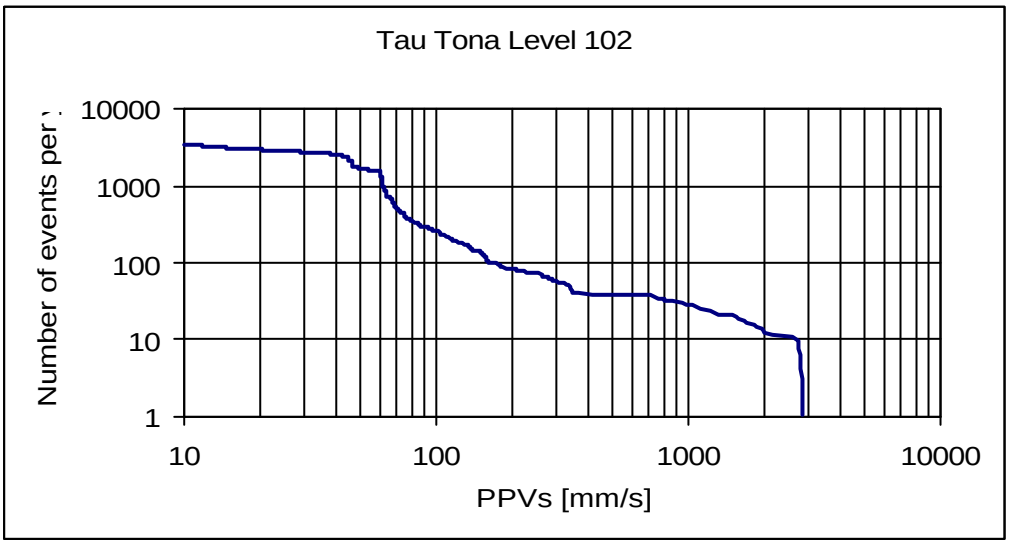

Figure 3.6 Peak particle velocities recorded at TauTona mine:, Level 102, Panels E1, E2, E3 HW, E3 FW, E4 HW and E4 FW

A maximum value of about 2.8 m/s was recorded during the monitoring period (Figure 3.6). Similar to the PPVs recorded at Level 97, this data set shows deviation from the linear distribution at level of 1.8 m/s.

Peak particle velocities recorded for period of 34 site days at Level 109, tunnel, are shown in Figure 3.7.

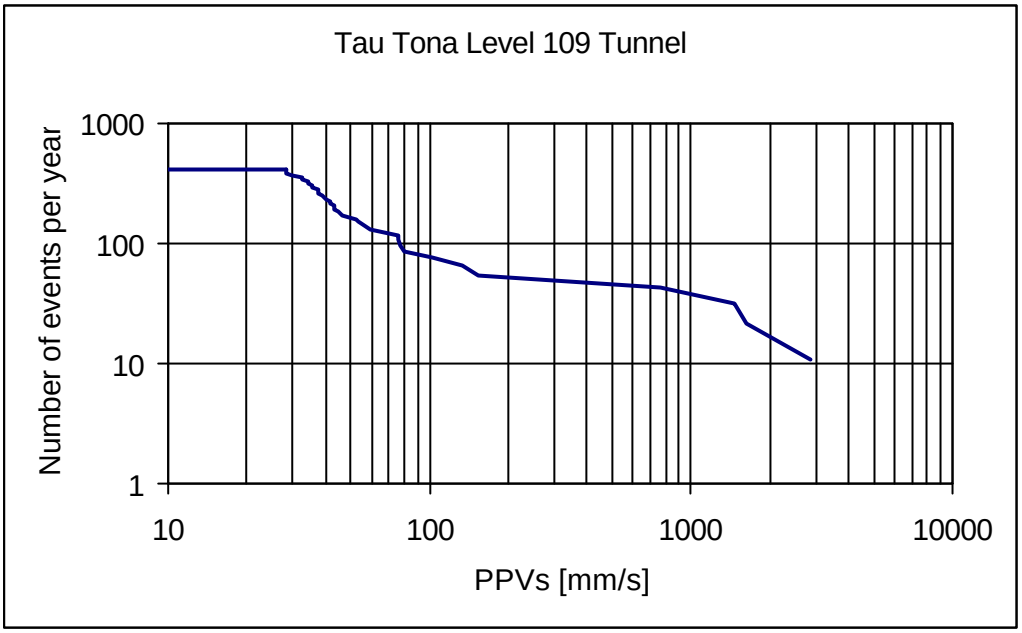

Figure 3.7 Peak particle velocities recorded at TauTona min: Level 109, tunnel

The PPVs recorded at Level 109 indicated very large values (Figure 3.7), most probably owing to the proximity of a very active seismic source below the site. The maximum value recorded was around 2.8 m/s, however, the monitoring period of this site was very short and the data are not statistically representable. The plot generally follows the characteristic slope of $N = 10V^{1}$ (where V = PPVs in m/s). This site had the highest rate of velocities greater than 800 mm/s. As only four of these events were recorded, the significance is low.

Peak particle velocities recorded for a period of 571 site days at Level 120, Panels E3, E4 and E5 are shown in Figure 3.8.

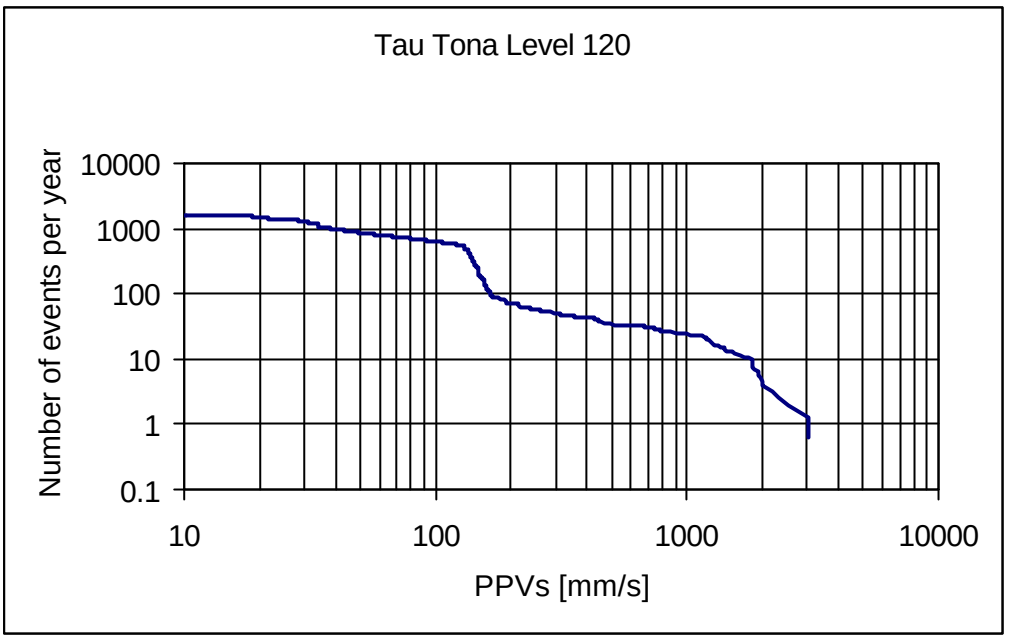

Figure 3.8 Peak particle velocities recorded at TauTona mine: Section 332, Level 120, Panels E3, E4 and E5

Maximum values of 3.0 m/s were recorded during the monitoring period (Figure 3.8). Slight deviation from the linear distribution is visible at that point.

3.1.1 Case study of footwall heaving at Level 102

Recent studies of the rock mass behaviour in TauTona mine have indicated strong footwall heaving in some of the areas (Murphy, 2001). A rapid footwall bulking was observed in several cases when the source of the seismic events is located beneath the reef. The suggested mechanism of footwall heaving is given by Murphy in Figure 3.9.

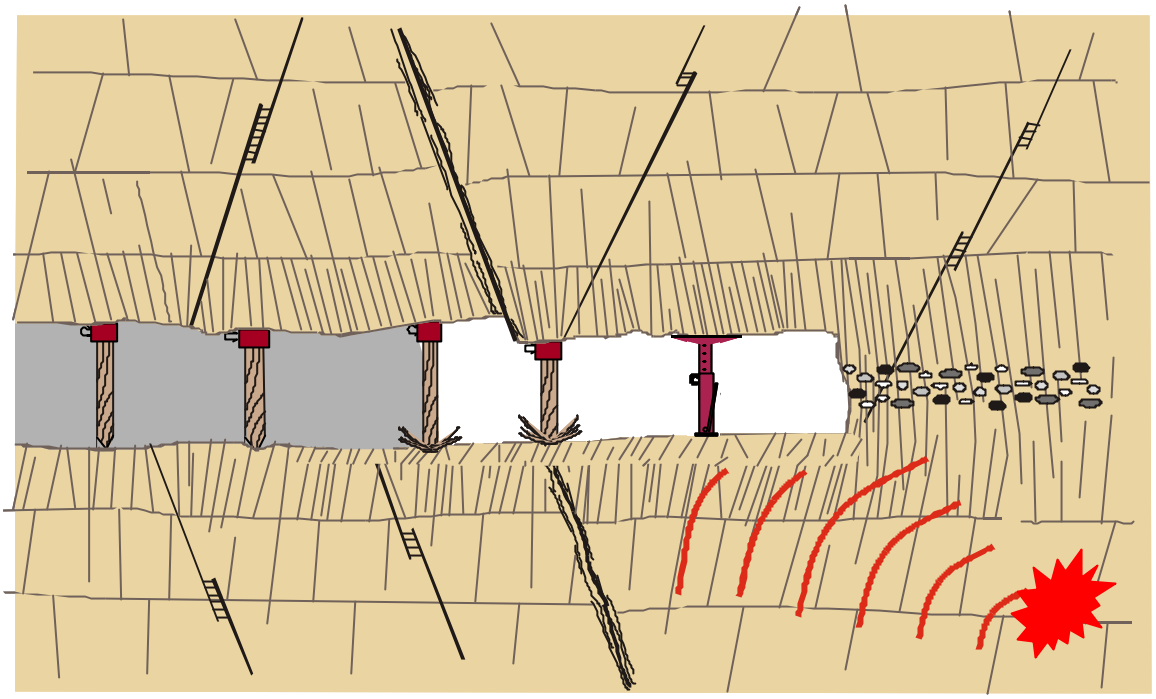

Figure 3.9 Schematic diagram illustrating the process of footwall lifting (Murphy, 2002)

Based on studies of support vibration during the seismic events, several authors (Milev, GAP 201, 1997; Cichowicz, GAP 709b 2001) show that some of the energy is transmitted though the support and returns to the rock mass. This indicates that not all of the energy can be absorbed by the support and in some cases could cause damage. This process is very well illustrated in Figure 3.10 where the seismic waves after bulking the footwall (Figure 3.9) initiated substantial damage to the hangingwall.

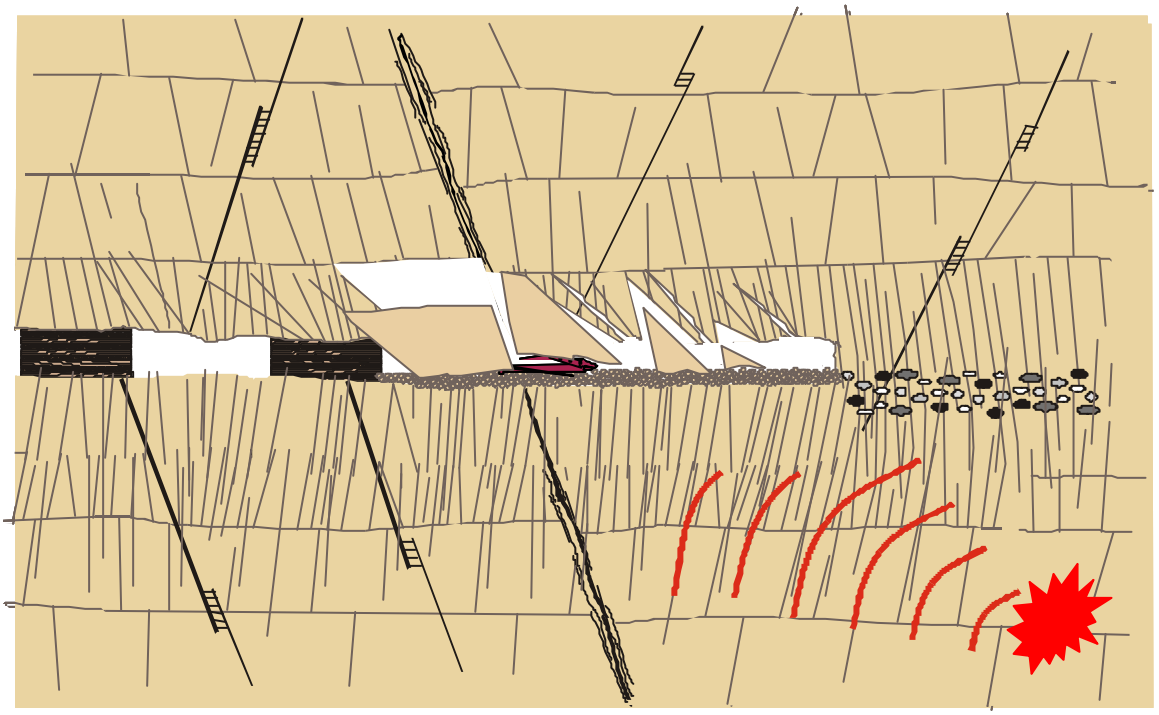

Figure 3.10 Fotwall heaving following by haningwall damage (Murphy, 2002)

To investigate this hypothesis PVDs were installed on the hangingwall and the footwall at Level 102 Panel E3. The recorded peak velocities recorded in both hangingwall and footwall are compared in Figure 3.11.

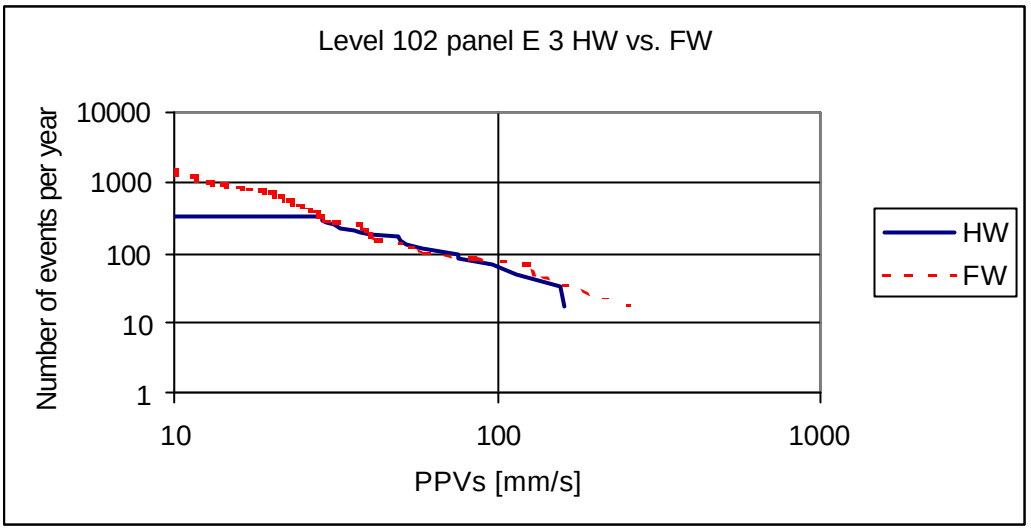

Figure 3.11 PPVs recorded at both the footwall and the hangingwall at Level 102, Panel E3

The results shown in Figure 3.11 indicate slightly larger PPVs in the footwall. However, no damaging events were recorded during the monitoring period.

3.2 Kloof gold mine

Ten seismically active sites in three sections of the mine were instrumented, following a discussion with the rock mechanics manager, Mr D. Geyser. The sites were all on VCR with depths ranging from 2 900 m to 3 000 m. The sections were on the North and South sides of a well-established longwalls. Backfill was not used in any of the sites.

The data and the current results obtained for Kloof gold mine are summarised in Table 3.3.

Table 3.3 PPVs measured at Kloof gold mine during the period of observation.

Section	Panel	Time (days)	PPV G.T. 100 (mm/s)	PPV G.T. 800 (mm/s)	PPV (mm/s)	Beginning	End
37-34 North	13050	92	17	2	1 749	20-Aug-01	7-Dec-01
	13090	106	10	4	2 846	20-Aug-01	11-Jan-02
	13096	70	0	0	99	20-Aug-01	13-Nov-01
37-34 South	13058	94	80	6	1 551	17-Aug-01	27-Dec-01
	13075	84	54	0	235	17-Aug-01	10-Nov-01
	13151	21	4	1	2 167	10-Nov-01	1-Dec-01
37-61 South	37-61 S1	17	0	0	42	21-Aug-01	8-Sep-01
	37-61 S2	37	0	0	61	21-Aug-01	3-Oct-01
	37-61 S3	40	2	0	171	21-Sep-01	31-Oct-01
	37-61 S4	98	9	0	287	21-Aug-01	8-Dec-01

The results listed in Table 3.3 illustrate large variations in PPVs for the different areas. Values of up to 2.8 m/s were recorded at Section 37-34 North.

The position of the monitoring Sections 37-34 South and 37-34 North are illustrated in Figure 3.12.

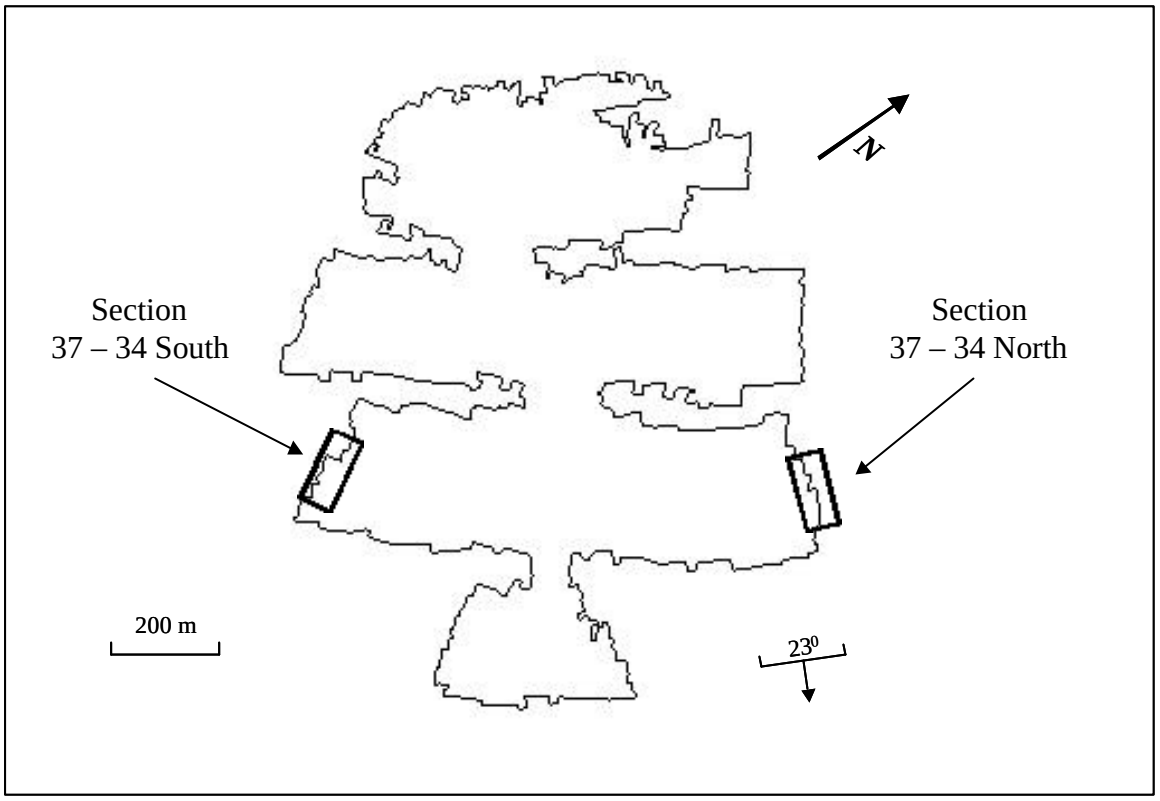

Figure 3.12 Position of the monitoring sites at Sections 37-34 South and 37-34 North

Peak particle velocities recorded for a period of 268 site days at Kloof gold mine: Section 37-34 North, Panels 13050, 13090 and 13096 are shown in Figure 3.13.

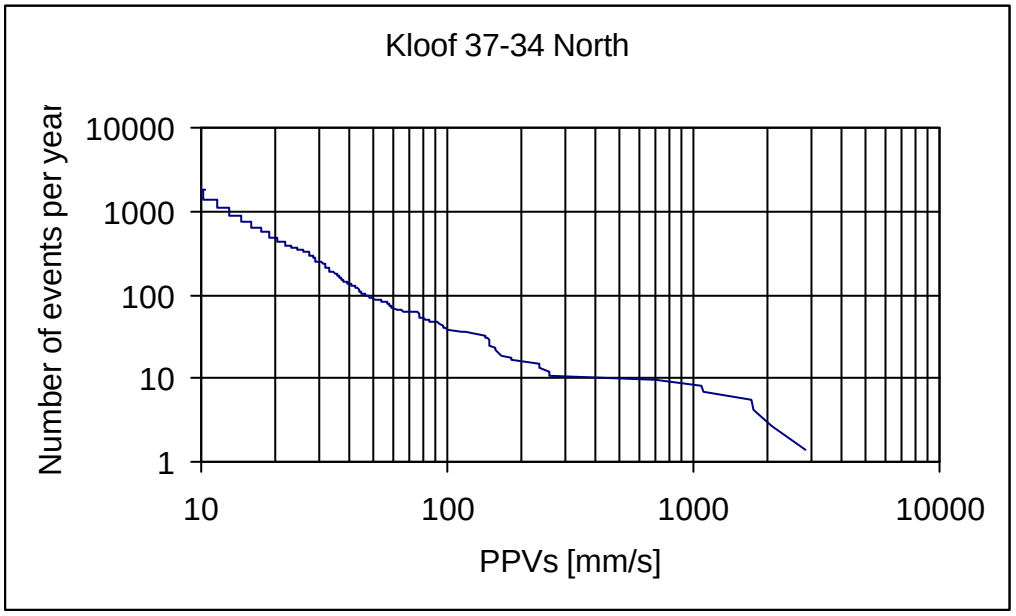

Figure 3.13 Peak particle velocities recorded at Kloof gold mine: Section 37-34 North, Panels 13050, 13090 and 13096

Maximum values of 2.8 m/s were recorded during the monitoring period (Figure 3.13).

Peak particle velocities recorded for period of 199 site days at Kloof gold mine: Section 37-34 South, Panels 13058, 13075 and 13151 are shown in Figure 3.14.

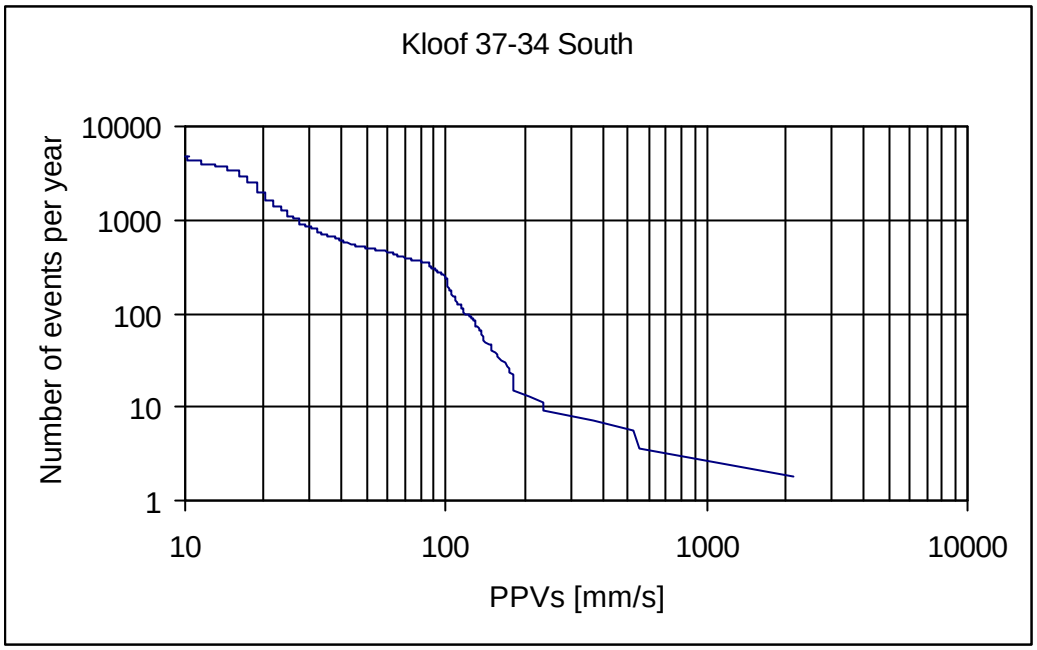

Figure 3.14 Peak particle velocities recorded at Kloof gold mine: Section 37-34 South, Panels, 13058, 13075 and 13151

Maximum values of about 2.2 m/s were recorded during the monitoring period (Figure 3.14).

The position of the monitoring Section 37-61 South is illustrated in Figure 3.15.

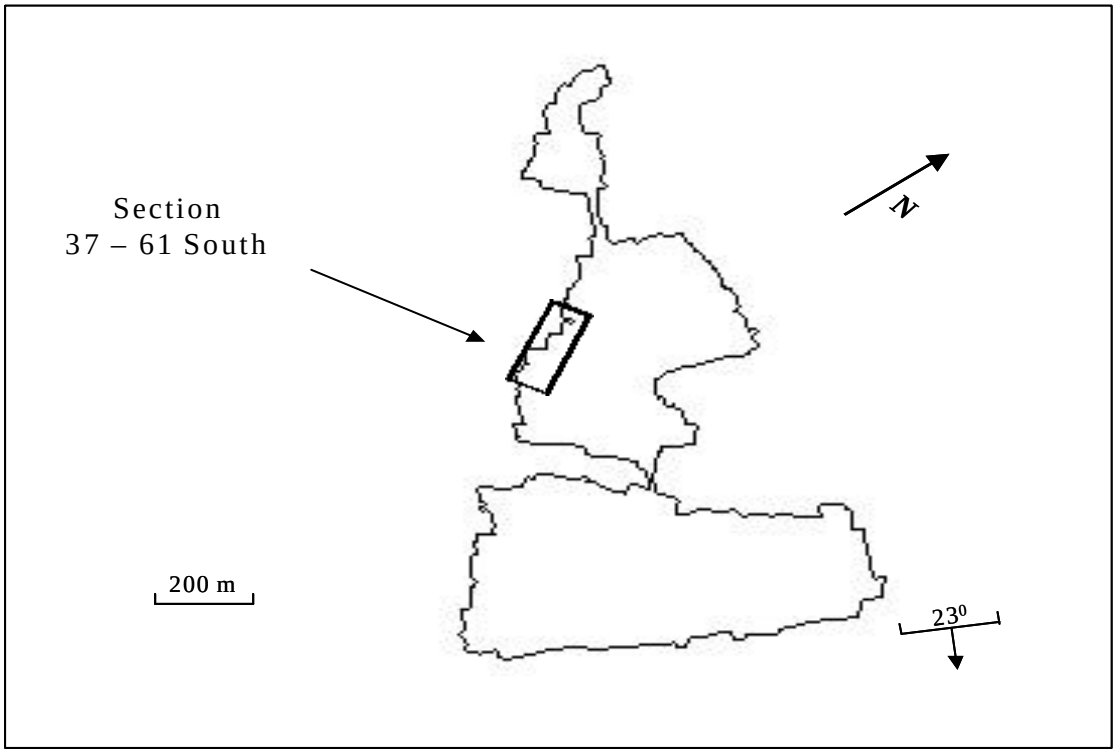

Figure 3.15 Position of the monitoring sites at Section 37-61 South

Peak particle velocities recorded for a period of 192 site days at Kloof gold mine: Section 37-61 South, Panels S1, S2, S3 and S4 are shown in Figure 3.16.

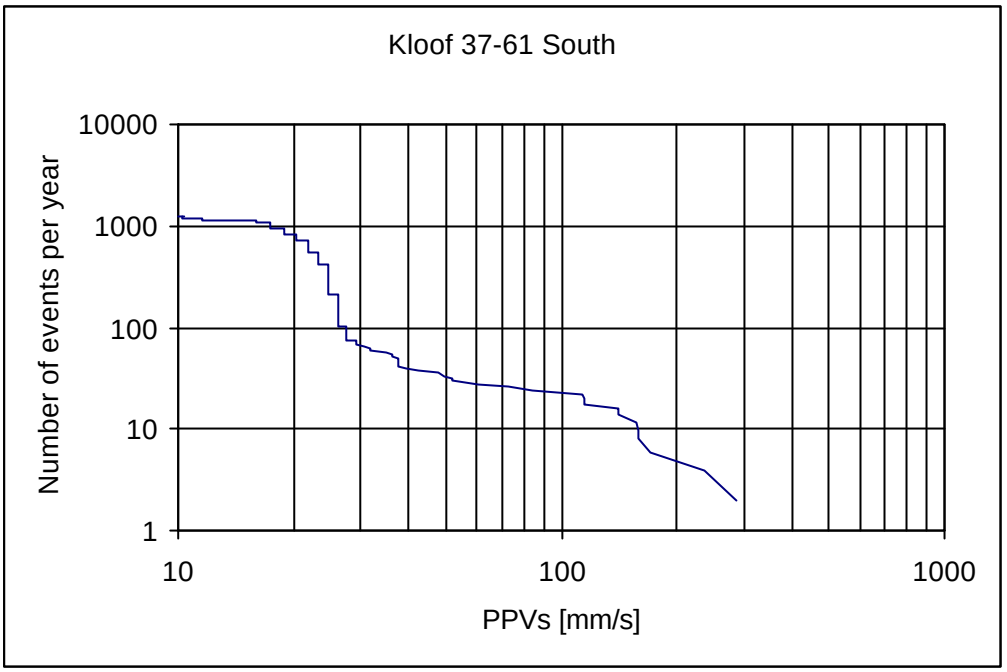

Figure 3.16 Peak particle velocities recorded at Kloof gold mine: Section 37-61 South, Panels S1, S2, S3 and S4

Maximum values close to 0.3 m/s were recorded during the monitoring period (Figure 3.16).

3.3 Mponeng gold mine

Seven seismically active sites in three sections have been instrumented, following a discussion with Mr A. Ward. Support at these sites consists only of conventional support components; no backfill was placed in this stope. The depth of the sites ranged from 2 750 m to 2 900 m. A site was also run in a haulage for 47 days.

The data and the current results obtained for Mponeng gold mine are summarised in Table 3.4.

Table 3.4 PPVs experienced at Mponeng gold mine during the period of observation

Section	Panel	Time (days)	PPV G.T. 100 (mm/s)	PPV G.T. 800 (mm/s)	PPV (mm/s)	Beginning	End
94-44	E3	28	9	2	1 253	10-Dec-01	8-Jan-02
	E4	89	38	2	2 338	30-Aug-01	8-Jan-02
	E5 Top	46	5	0	262	7-Sep-01	5-Dec-01
	E5 Bottom	58	17	3	1 906	17-Jul-01	12-Dec-01
	E6	72	7	0	418	19-Jul-01	9-Jan-02
94-IV	Haulage	47	3	0	731	23-Nov-01	8-Jan-02
99-44	E7 (ISSI)	63	31	5	2 089	27-Sep-01	6-Jan-02

The results listed in Table 3.4 illustrate large variations in PPVs for the different areas. Values of 2.3 m/s were recorded in Section 94-44 and values of 2.1 m/s were recorded at Section 99-44.

Position of the monitoring Section 94-44 is illustrated in Figure 3.17. The stoping spans were small.

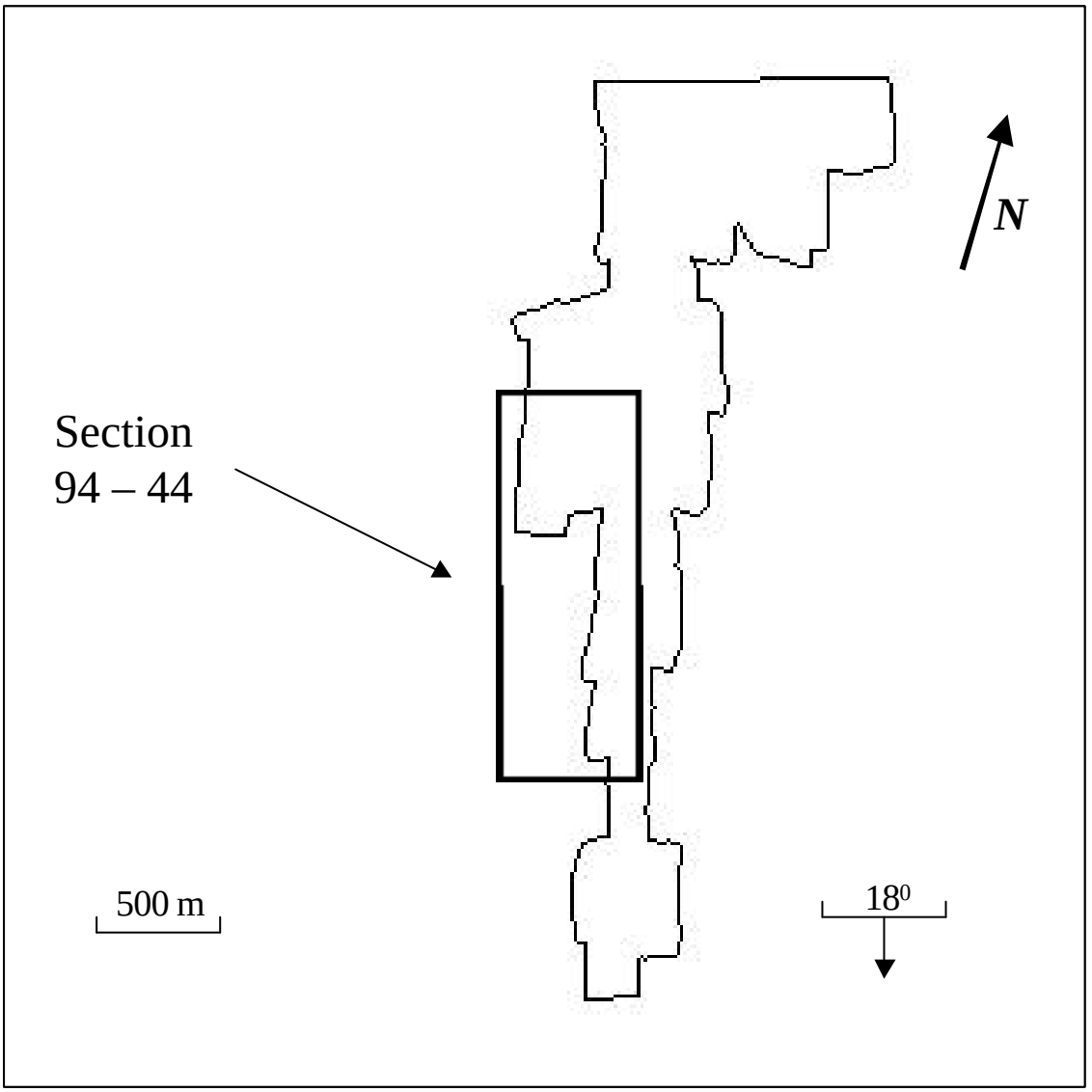

Figure 3.17 Position of the monitoring in Section 94-44

Peak particle velocities recorded for a period of 293 site days at Mponeng gold mine: Section 94-44, Panels E3, E4, E5 Top, E5 Bottom and E6 are shown in Figure 3.18.

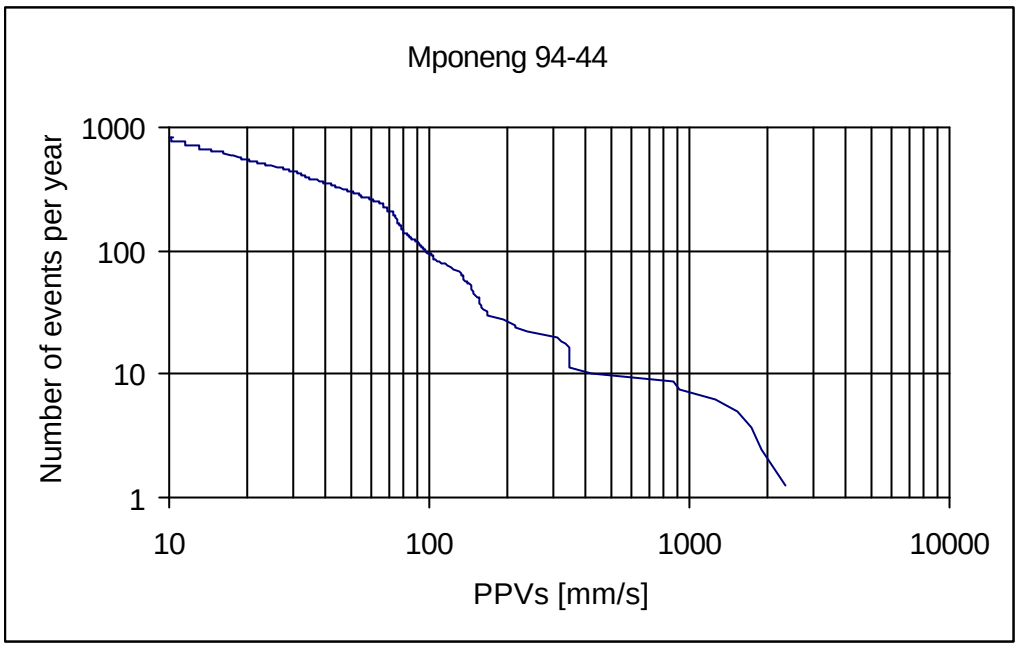

Figure 3.18 Peak particle velocities recorded at Mponeng mine: Section 94-44 Panes E3, E4, E5 Top, E5 Bottom, and E6

Maximum values of 2.3 m/s were recorded during the monitoring period (Figure 3.18).

Peak particle velocities recorded for a period of 47 site days at Mponeng gold mine: Section 94-IV, haulage, is shown in Figure 3.19.

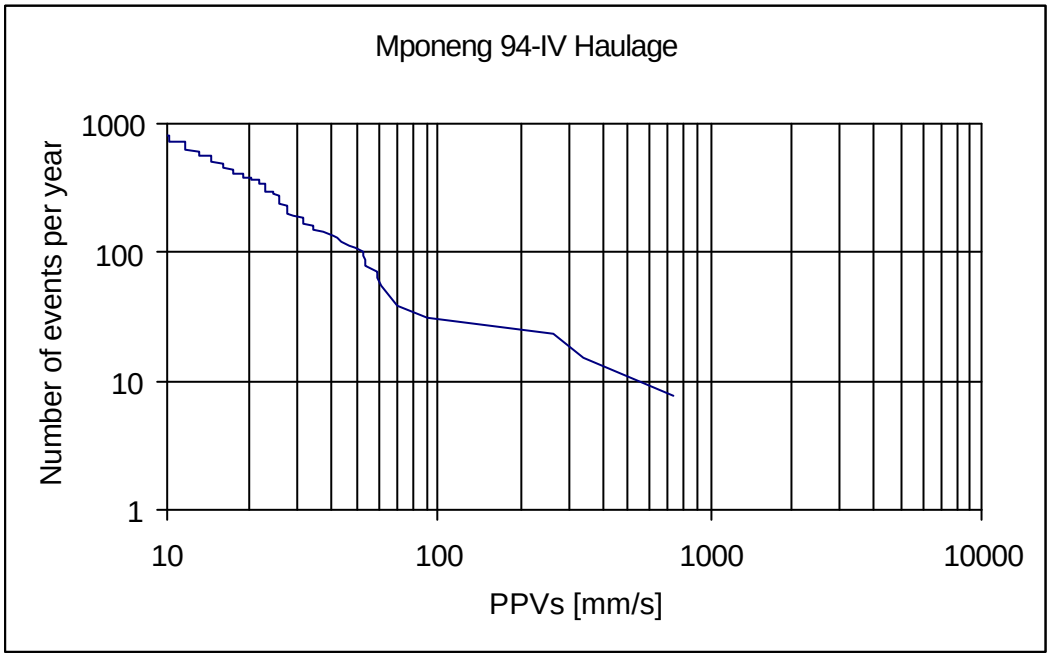

Figure 3.19 Peak particle velocities recorded at Mponeng mine: Section 94-IV-Haulage

Maximum values of 0.7 m/s were recorded during the monitoring period (Figure 3.19).

Peak particle velocities recorded for period of 63 site days at Mponeng gold mine; Section 99-44, Panel E7 is shown in Figure 3.20.

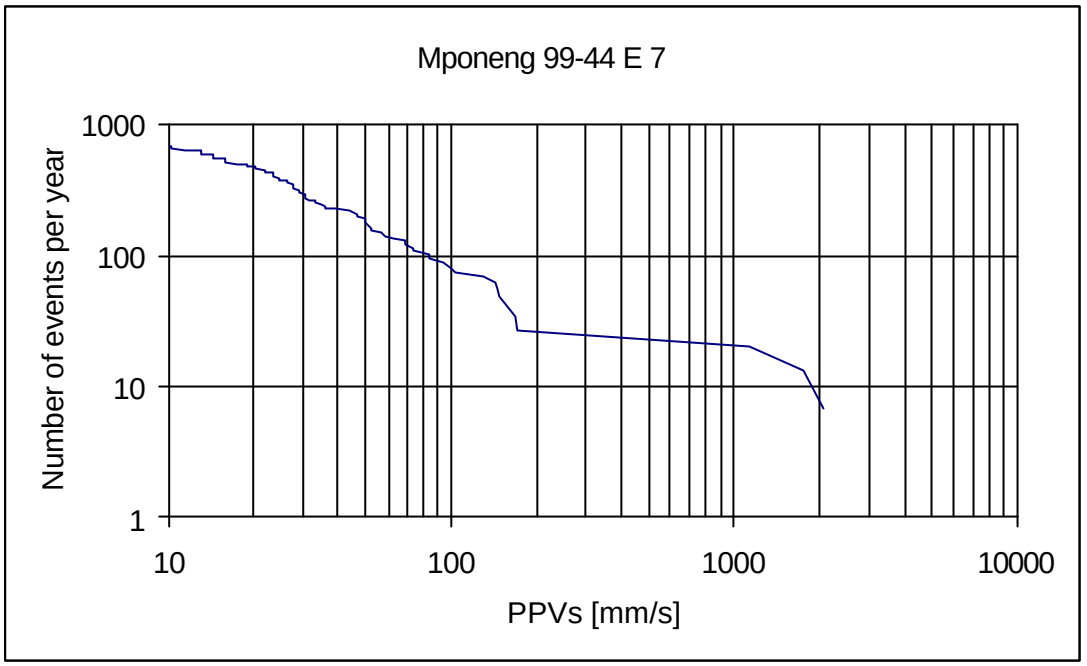

Figure 3.20 Peak particle velocities recorded at Mponeng mine: Section 99-49, Panel E7

Maximum values of 2.0 m/s were recorded during the monitoring period (Figure 3.20). Slight deviation from the linear distribution is visible at that point.

3.4 Test sites at Driefontein mine

It was suggested by SIMRAC that CSIR Mining Technology and ISS International open a joint site in order to compare their measurements. A test site at Driefontein gold mine # 1 Shaft 30/31 VCR was instrumented with an 8-channel Ground Motion Monitor (GMM) and Peak Velocity Detector (PVD). This site was also monitored by ISS International using accelerometers. The underground layout of the site and the positions of the recording instruments is shown in Figure 3.21.

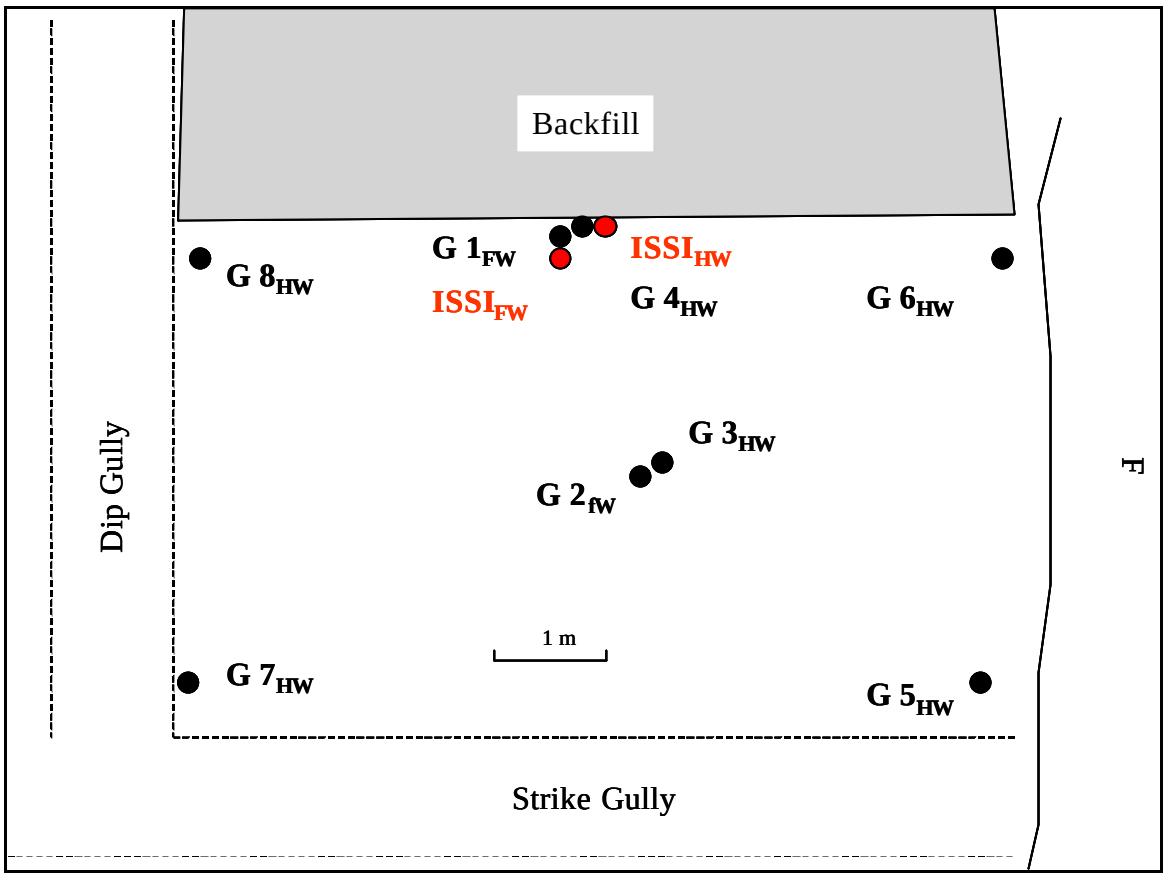

Figure 3.21 Underground layout and the position of monitoring instruments installed by CSIR Mining Technology and ISS International (ISSI)

Common events from this site were identified in collaboration with Dr A. Cichowicz from ISSI. The velocities measured by CSIR Mining Technology were differentiated to accelerations and than compared to the accelerations measured by ISSI.

Separate comparison was made for the peak particle accelerations recorded on hangingwall and footwall. The results are shown in Figure 3.22 (a, b).

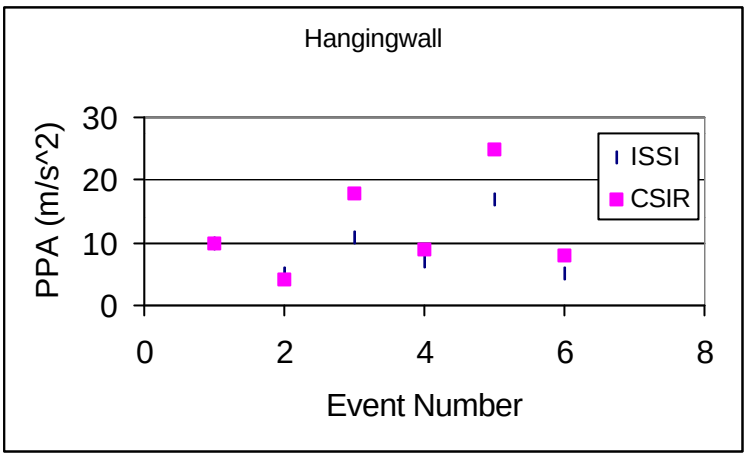

(a)

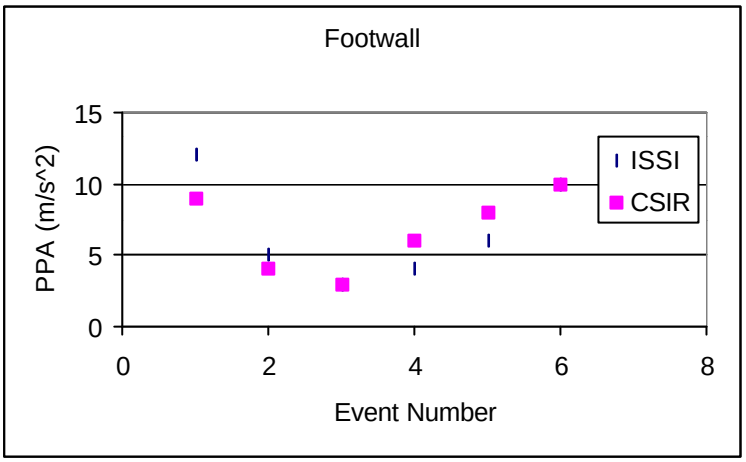

(b)

Figure 3.22 (a, b) Peak particle accelerations (PPAs) measured by ISS International (ISSI) and CSIR Mining Technology (a) hangingwall; (b) footwall

Despite the differences in the measuring instruments, it is clearly illustrated in Figure 3.22 (a, b) that the acceleration values reported by both organisations are similar. The small deviations in these values can be explained by the effect of the local fractures near each transducer and the differences in the source receiver geometry. Similar results were found in GAP 201. It is also interesting to note that the deviations in values measured on the hangingwall are greater than the deviations measured on the footwall, where the accelerations were generally lower.

3.5 Discussion and conclusions

The peak particle velocities recorded at TauTona, Kloof and Mponeng gold mines were summarised and shown in Figures 3.23, 3.24 and 3.25 respectively. The number of events was normalised on the number of site days for each corresponding mine, and then, an annual rate was estimated.

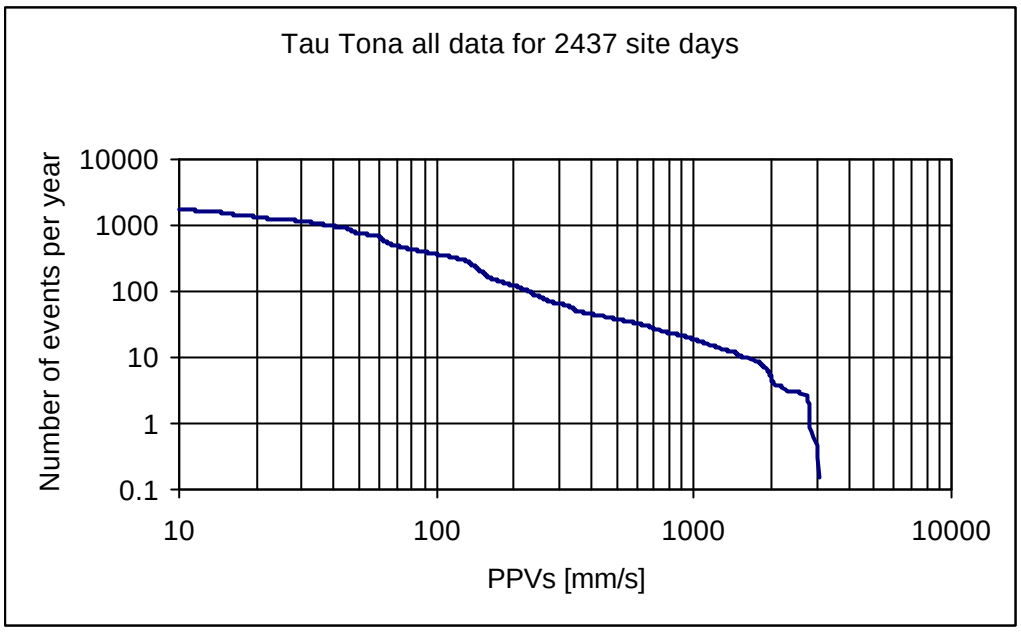

Figure 3.23 Peak particle velocities recorded at TauTona mine during the course of this project

A total number of 15 139 seismic events were recorded at TauTona gold mine during the monitoring period of 2 437 site days. As is shown in Figure 3.23, a maximum value of 3 m/s is obtained. However, a deviation from the linear distribution is visible for values of PPVs more than 2.8 m/s.

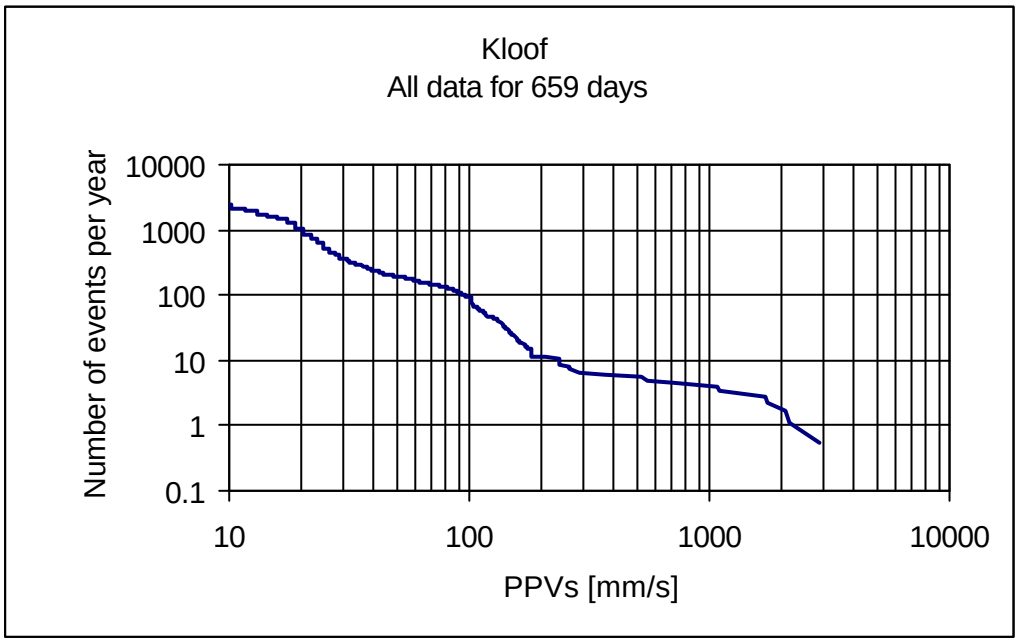

Figure 3.24 Peak particle velocities recorded at Kloof mine during the course of this project

A total number of 6 066 seismic events were recorded at Kloof gold mine during the monitoring period of 659 site days. As is shown in Figure 3.24, a maximum value of 3 m/s is obtained.

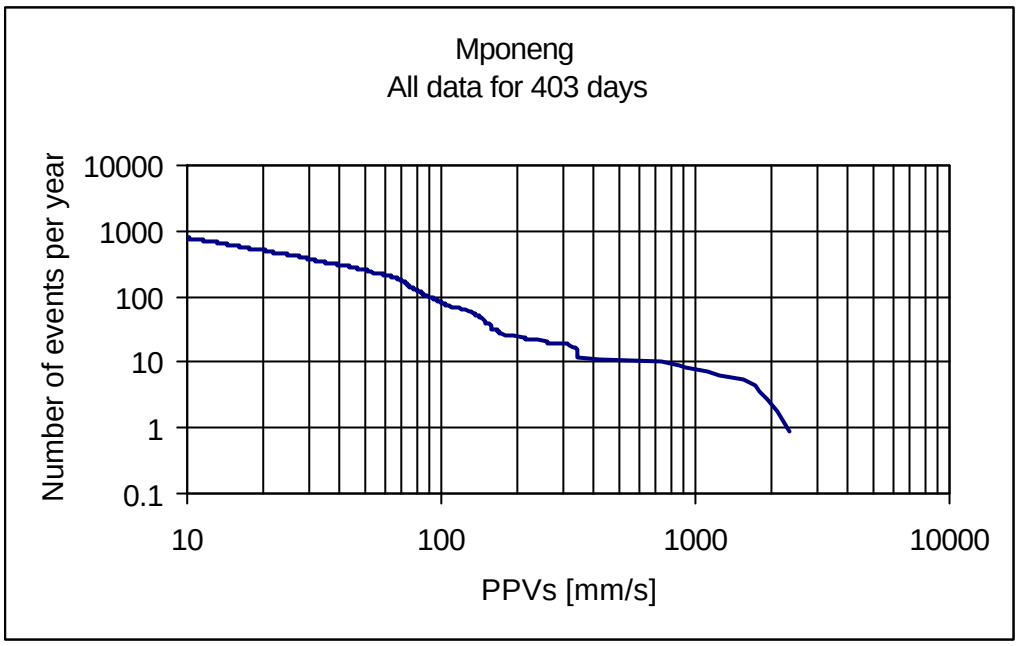

Figure 3.25 Peak particle velocities recorded at Mponeng mine during the course of this project

A total number of 1 183 seismic events were recorded at Mponeng gold mine during the monitoring period of 403 site days. As is shown in Figure 3.25, a maximum value of 2.3 m/s is obtained.

4 Back-analyses of mine network data to derive the velocity amplification factors on the skin of the excavations

One of the most important factors in the design of rockburst-resistant support systems is an adequate knowledge of the ground motion at the surface of the excavations. A number of studies conducted during the last decade have shown a significant difference between the PPVs measured in the solid rock and the PPVs measured on the surface of excavations (Durrheim et al., 1997; Spottiswoode et al., 1997; Milev et al., 1999; and Cichowicz et al., 2000). Most of the studies, however, were based on a limited number of observations in only a few geotechnical areas.

During the course of this project, a large volume of seismic data recorded on the skin of the excavations was compared to the seismic data recorded by mine seismic networks where transducers are installed in boreholes drilled into solid rock. The PPVs recorded by mine seismic networks were transferred to the point of each PVD location. In the transformation, the value of PPV was scaled using a scaling factor of $(\textit{hypocentral distance to the site})^{-1.5}$ and then the average value of all sites that recorded this particular event was taken. The hypocentral distance was calculated from given event location to the PVD site and to each of the mine network geophone sites.

All events recorded by the mine seismic network at more than two stations were compared to the seismic events recorded by the PVD. The correlation of the data in the time domain was done by an automatic procedure developed during this project.

The difference between PPVs recorded on the skin of the excavations and in solid rock was used to outline the site response as a function of hypocentral distance for each area studied. Additional analyses were made to gain more insights into the nature of the site response. The relationship between the PPVs and following important seismic parameters was analysed:

- Site response vs. hypocentral distance
- Site response vs. source radius
- Source radius vs. hypocentral distance
- Source radius vs. magnitude
- Site response vs. wavelength (Lambda)
- Site response vs. maximum velocity

The mine-wide data sets overlapping the total monitoring period were extracted from each mine's seismic database. The site response obtained on the surface of excavations were analysed for three different mines: TauTona, Kloof and Mponeng gold mines, exploring Carbon Leader and Ventersdorp Contact Reefs. The discussion of results obtained for each particular mine follows in this section.

4.1 TauTona gold mine

The underground monitoring period at TauTona mine was 2 437 site days in total, spread between 22 sites. The observations were made between November 2000 and January 2002. A data set corresponding to this time-period was extracted from the mine network and compared to the data recorded.

The site response as a function of the hypocentral distance was calculated for Level 87. This includes three hangingwall sites and one footwall site, located in Panels E1, E1A and E2. The results are shown in Figure 4.1.

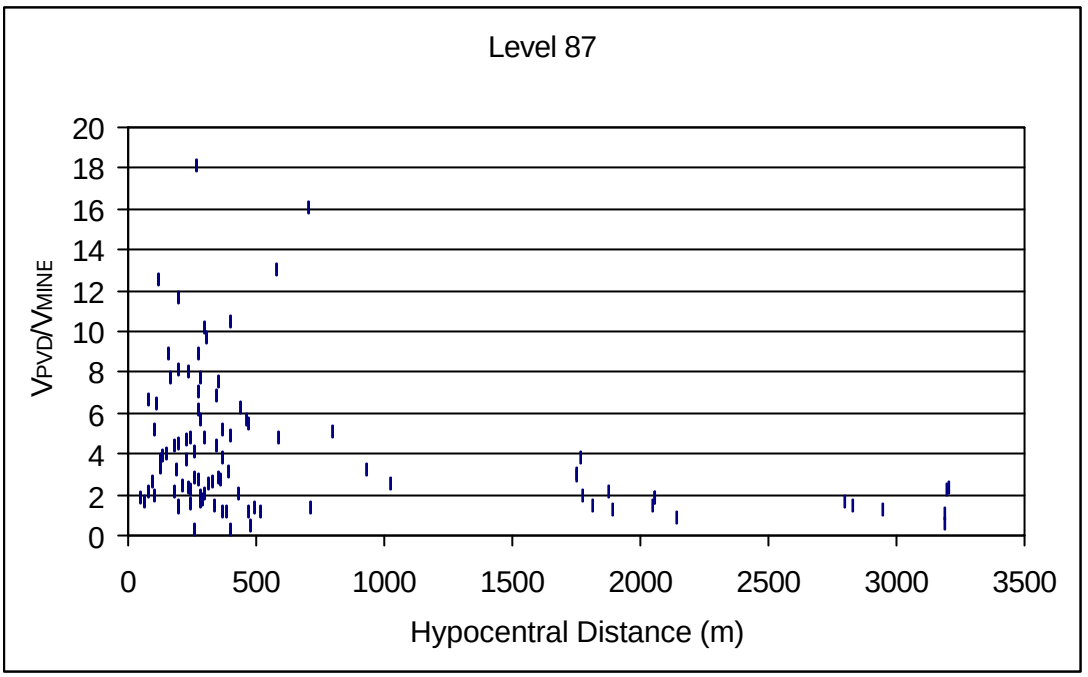

Figure 4.1 Site response obtained at Level 87 as a function of hypocentral distance

It is clearly indicated in Figure 4.1 that the maximum site response obtained for the hypocentral distances is up to 500 m and then attenuate with the hypocentral distance.

The site response calculated for Level 94, Panels E1, E2, and E3 is shown in Figure 4.2.

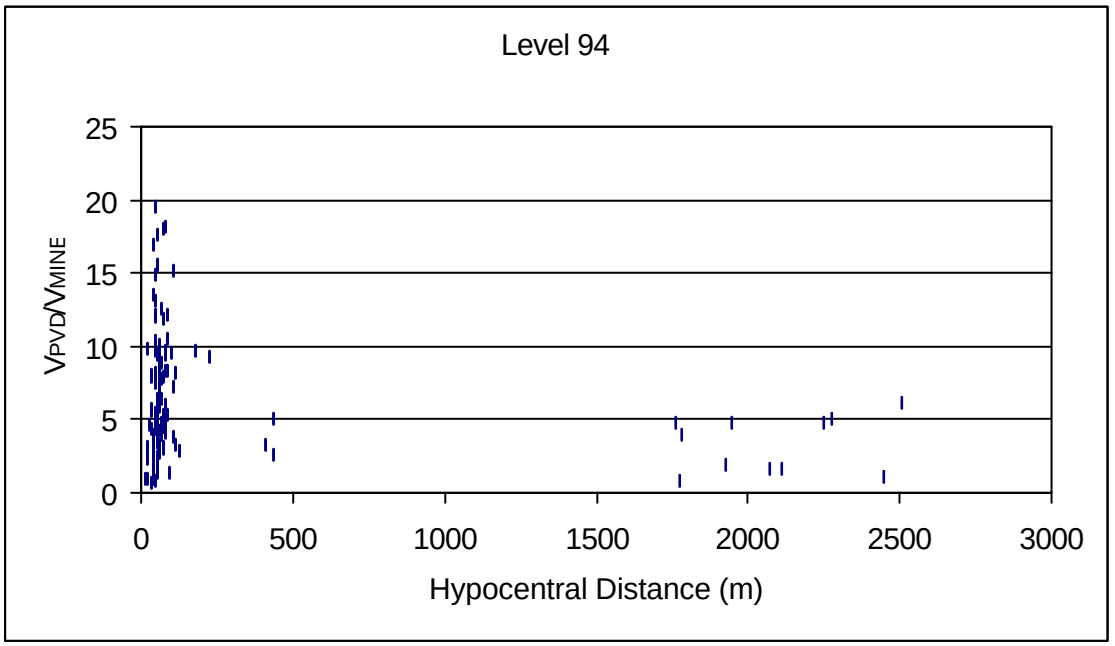

Figure 4.2 Site response obtained at Level 94 as a function of hypocentral distance

The mining operations taking place at this site are directed to extraction of the shaft pillar surrounded by mined-out areas. Most of the seismic events are within 100 m of the working panels. The high-level of site response was observed at that distance.

The site response calculated for Level 97, Panels E2, E3, E5 E6 and E7 is shown in Figure 4.3.

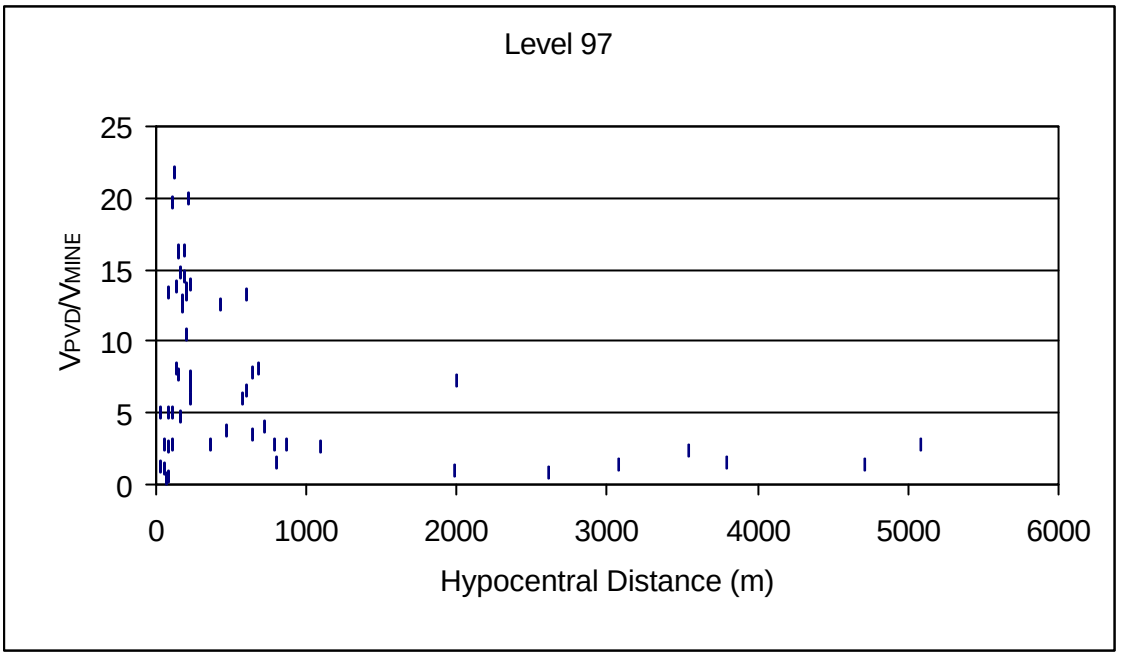

Figure 4.3 Site response obtained at Level 97 as a function of hypocentral distance

Level 97 is located in the far end of the mine where the resolution capabilities of the mine network are comparatively poor, leading to a higher location error. This explains the lower number of correlated events indicated in Figure 4.3.

The site response calculated for Level 102, Panels E1, E2, E3 and E4 is shown in Figure 4.4.

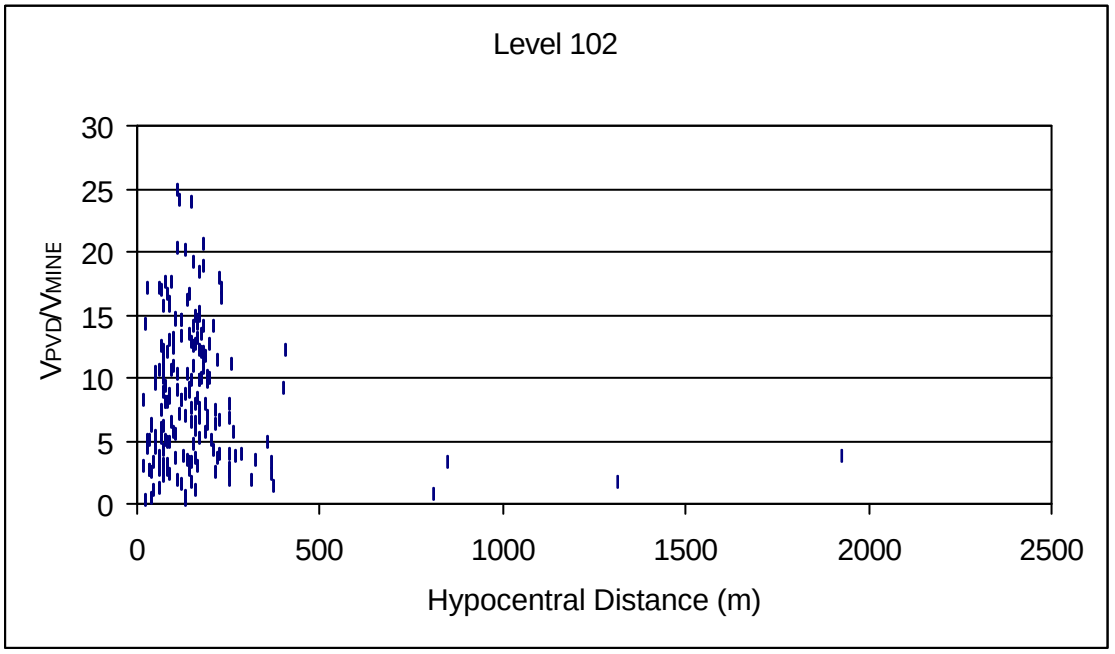

Figure 4.4 Site response obtained at Level 102 as a function of hypocentral distance

The site response obtained on the hangingwall and the footwall at Panel E3 was compared. Figure 4.5 (a, b) illustrates these site responses as a function of hypocentral distance.

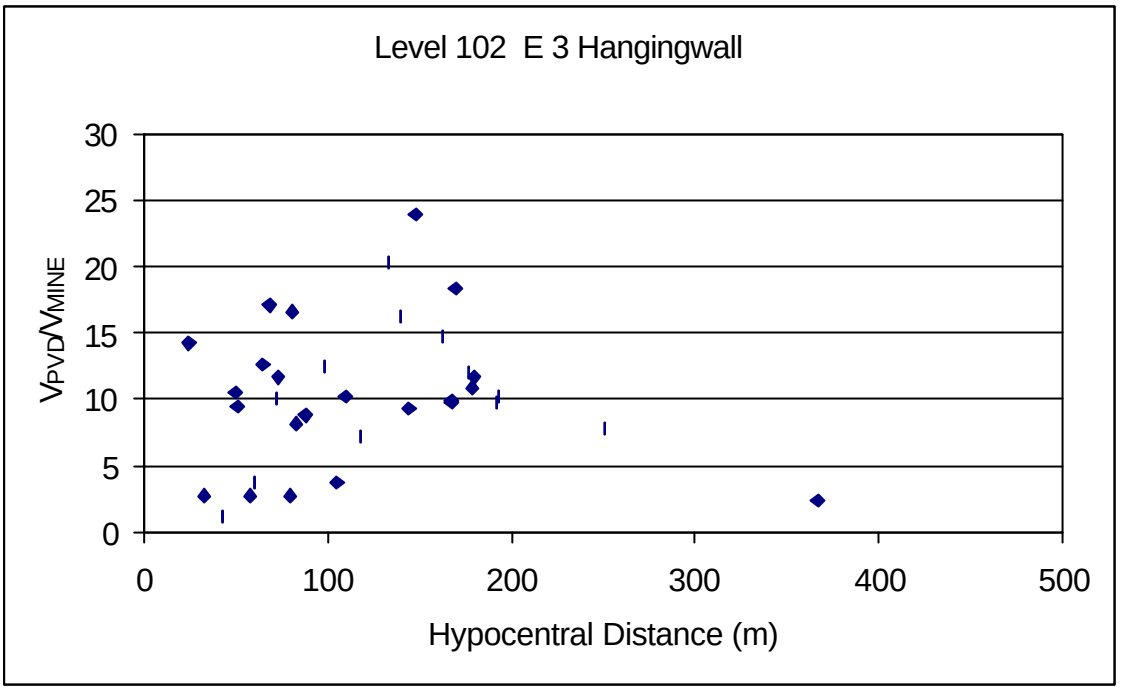

(a)

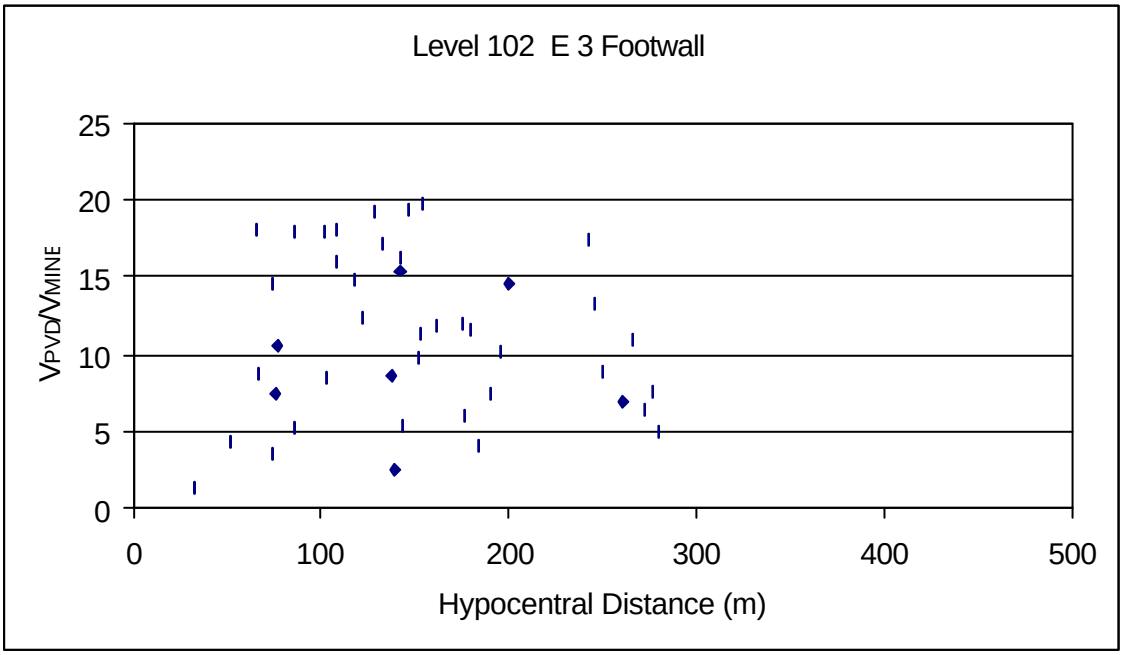

(b)

Figure 4.5 (a, b) Site response determined at Level 102, Panel E3: (a) hangingwall; (b) footwall

The PPVs recorded at Panel E3 indicate higher values in the footwall when compared to the hangingwall (see Figure 3.11). The process of footwall heaving in this panel was described by

Murphy (2000), which explained the higher footwall ground motion. The site response, however, is very similar for both hangingwall and footwall. As is seen in Figure 4.5 (a, b) a maximum response is obtained for seismic events with hypocentral distance of around 100 m to 150 m. The distance between hangingwall and footwall, approximately 1 m, is a very small portion of the hypocentral distance and therefore the hangingwall and the footwall were reacting as one entity to the incoming seismic waves. Similar results were reported by Cichowicz (2001) using data recorded at East Driefontein gold mine # 1 Shaft.

Despite the number of larger PPVs recorded at the Level 109 tunnel (Figure 3.7) there are only two seismic events, which correlated with the mine seismic network. The results are shown in Figure 4.6.

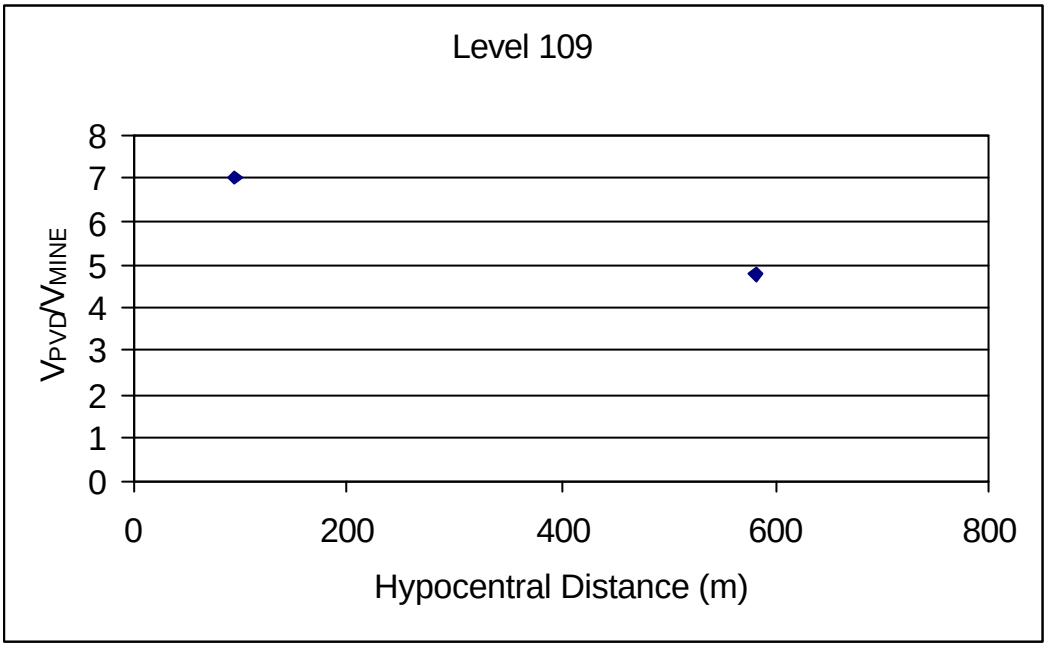

Figure 4.6 Site response obtained at Level 109 tunnel as a function of hypocentral distance

The site response measured in the tunnel is within the same range as the site response measured in stopes.

The site response calculated for Level 120, Panels E3, E4 and E5 is shown in Figure 4.7.

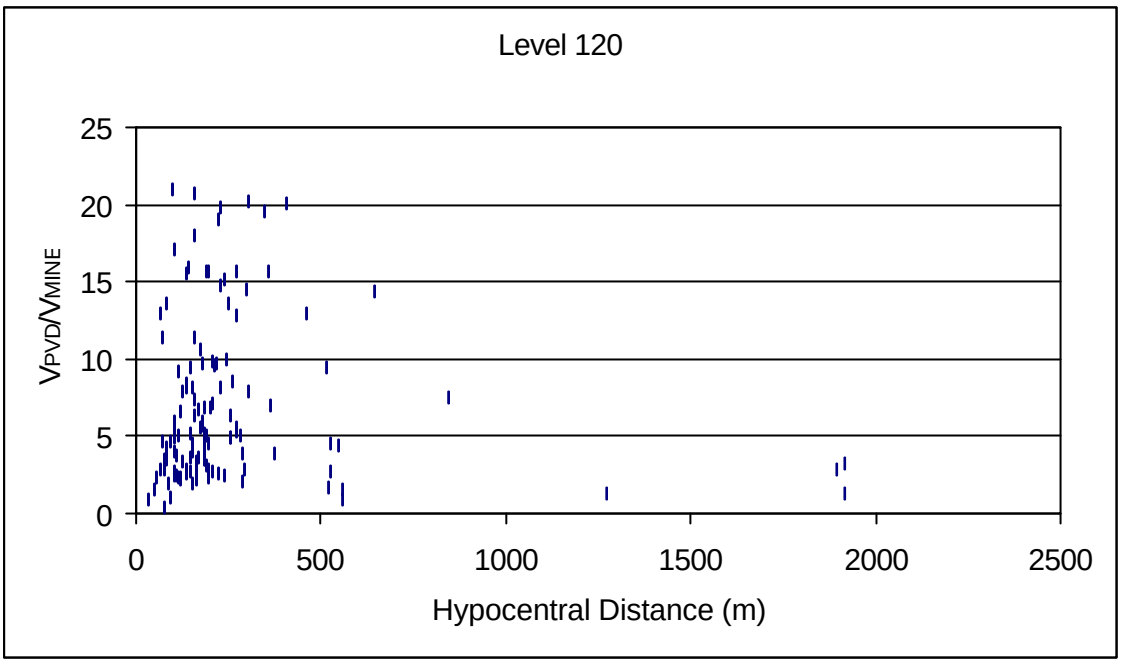

Figure 4.7 Site response obtained at Level 120 as a function of hypocentral distance

Most of the correlated seismic events shown in Figure 4.7 are located within 500 m from the face. The maximum site effect is viable for seismic events around 200 m from the face.

4.1.1 TauTona: site response outline

The site response estimated over the entire data set accumulated at TauTona mine is discussed in this section. The relationship between the site response and additional seismological parameters was outlined in an attempt to characterise the comprehensive rock mass behaviour under dynamic loading.

The site response as a function of hypocentral distance is shown in Figure 4.8.

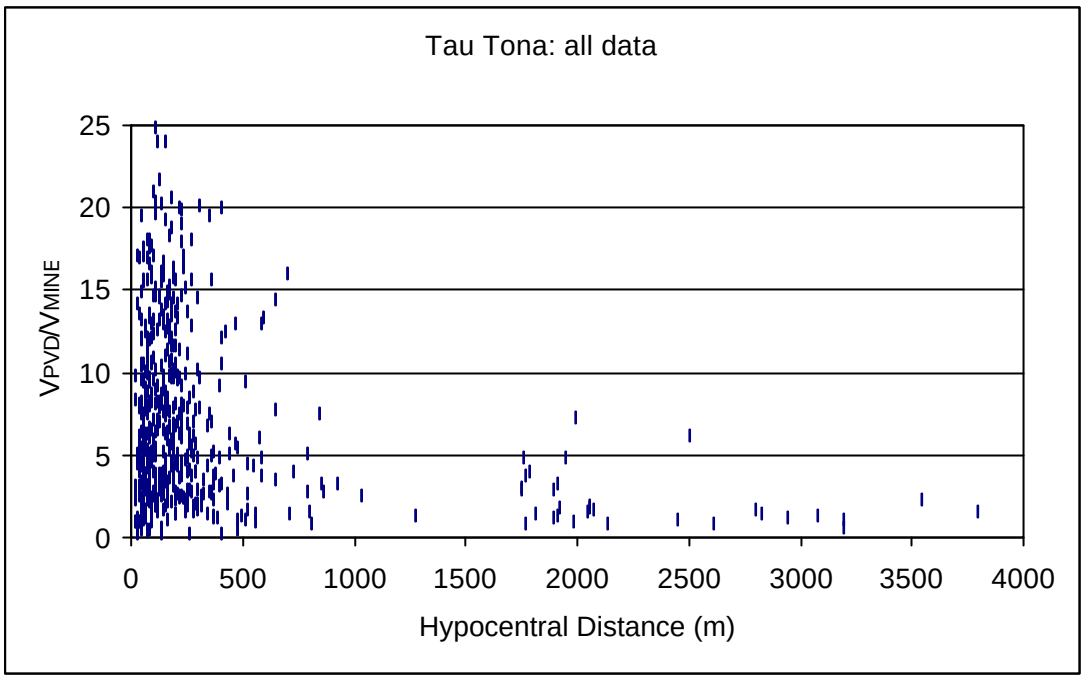

Figure 4.8 Site response obtained from all data recorded at TauTona mine as a function of hypocentral distance

The site response for all data recorded at TauTona mine indicate attenuation with the hypocentral distance. The exponential low of attenuation seems to be the closest approximation. However, due to the limited number of seismic events correlated at hypocentral distances longer then 500 m, the correlation coefficient for the exponential trend line is very low and thereafter the scaling equations are not presented here.

Another important parameter is the relationship between the level of the site response and the source radius (as estimated by the mine). This relationship is shown in Figure 4.9.

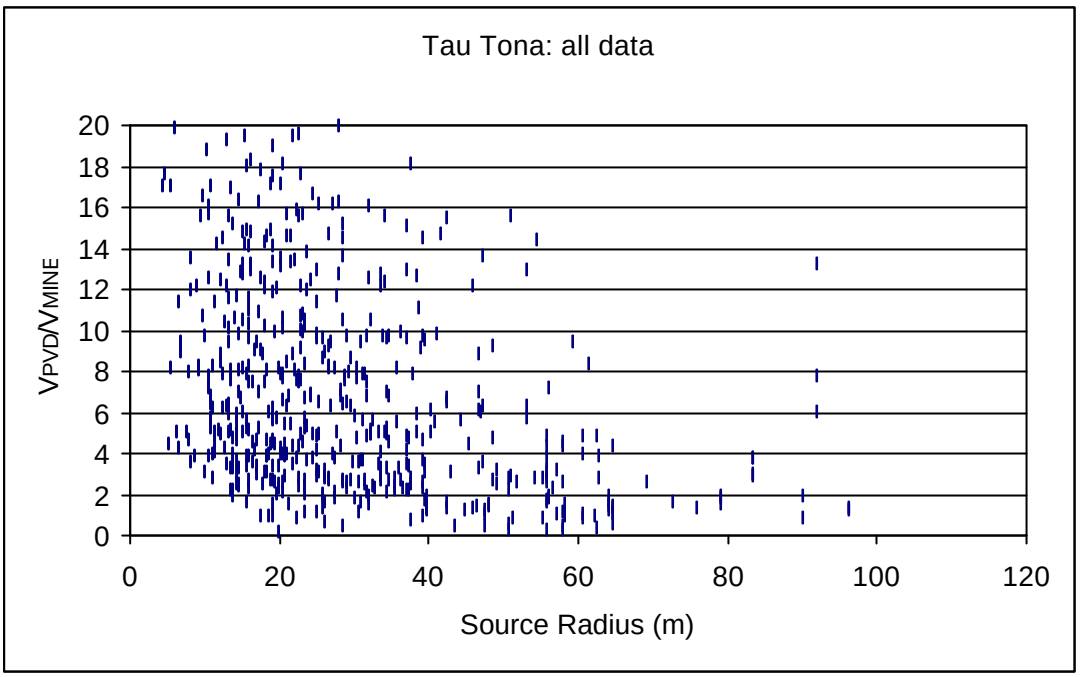

Figure 4.9 Site response obtained from all data recorded at TauTona mine as a function of source radius

As is indicated in Figure 4.9, the maximum site response is observed for source radii around 20 m and then it decay for the bigger radii.

To characterise the level of ground motion, it is also important to study the position of the source radius in respect to the face. McGarr (2001) shows that the strong ground motion in the source region is controlled by the strength of the rock mass that ruptures during the tectonic type seismic event. The tectonic dislocations in a weak rock mass have low-rupture velocity that generates only low levels of PPVs. In contrast, the strong quartzite rock mass surrounding the Carbon Leader and the Ventersdorp Contact Reef ruptures with high velocity and generates high-level PPVs associated with the most damaging events in this mining region. On the other hand, seismic events with high-rupture velocities generate high-frequency seismic signals, which can reach very high PPVs in the source region, but do not propagate very far due to the rapid attenuation of high-frequency signals. Applied in practice, this means that the seismic events taking place in the face area will be responsible for the highest velocities recorded by the PVD on the skin of the excavations. In many cases, these events will not have enough triggers to be recognised by the mine seismic network.

The data shown in Figure 4.10 indicates that the majority of the seismic events with source radius between 5 m and 55 m are between 0 m and 300 m from the face.

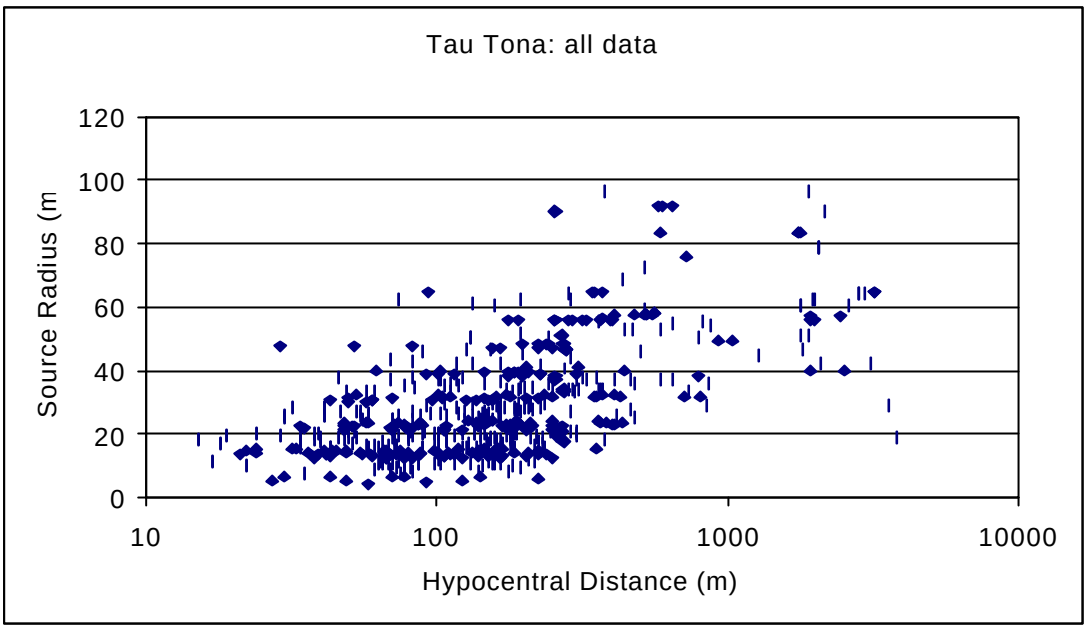

Figure 4.10 Source radius as a function of the hypocentral distance obtained from all data recorded at TauTona mine

The "characteristic" damaging event was introduced using the fatality database in the Carletonville mining area. Analysing the number of fatalities as a function of magnitude, Milev and Spottiswoode (1997) found that 50% of fatalities were associated with events smaller than $M \cong 2.0 \pm 0.2$ and the other 50% of fatalities were associated with larger events.

As defined, the "characteristic" damaging event was related to the corresponding source radius to quantify the site response for these events. The source radius as a function of the magnitude for all correlated events is shown in Figure 4.11.

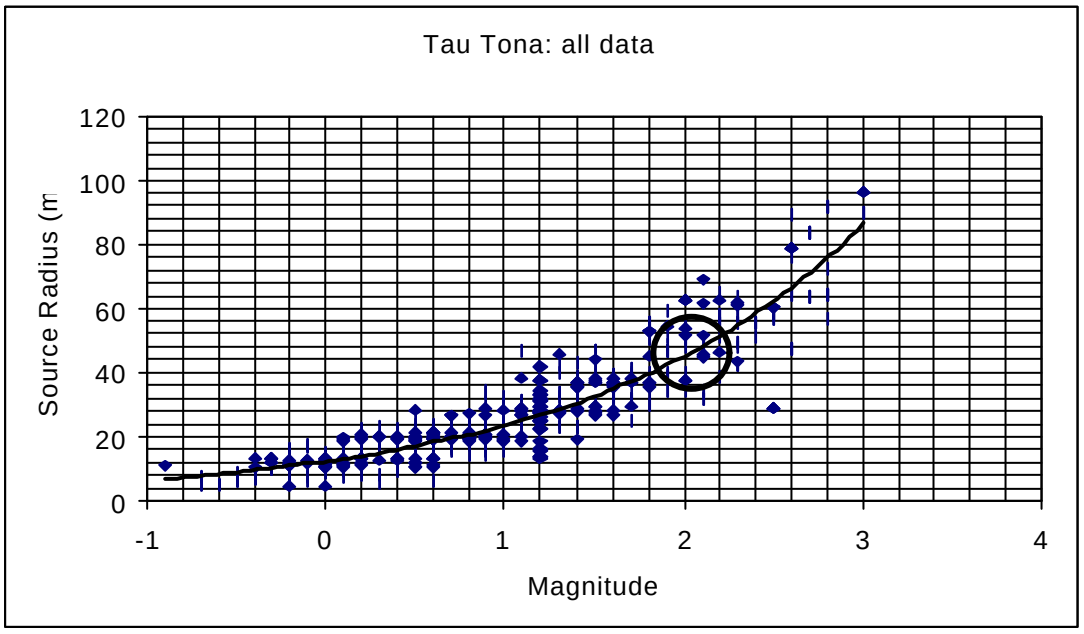

Figure 4.11 Graphical estimation of the source radius range for the "characteristic" damaging events $(M \approx 2.0 \pm 0.2)$ ***obtained from all data recorded at TauTona mine***

It is indicated in Figure 4.11 that source radii of 40 m to 58 m can be related to that "characteristic" event. Therefore, this radius range is slightly offset from the radius of maximum site response shown in Figure 4.9.

Milev at al. (1999) and Cichowicz et al. (2000) showed that local variations were less at low frequency through study of the spectral ratios at several sites. In Figure 4.12, the site response is shown as a function of the wavelength (Lambda), calculated from the shear-wave velocity and time between the peak width measured between two consecutive zero-crossings ($l = TV_S$ where $V_S = 3400\, m/s$).

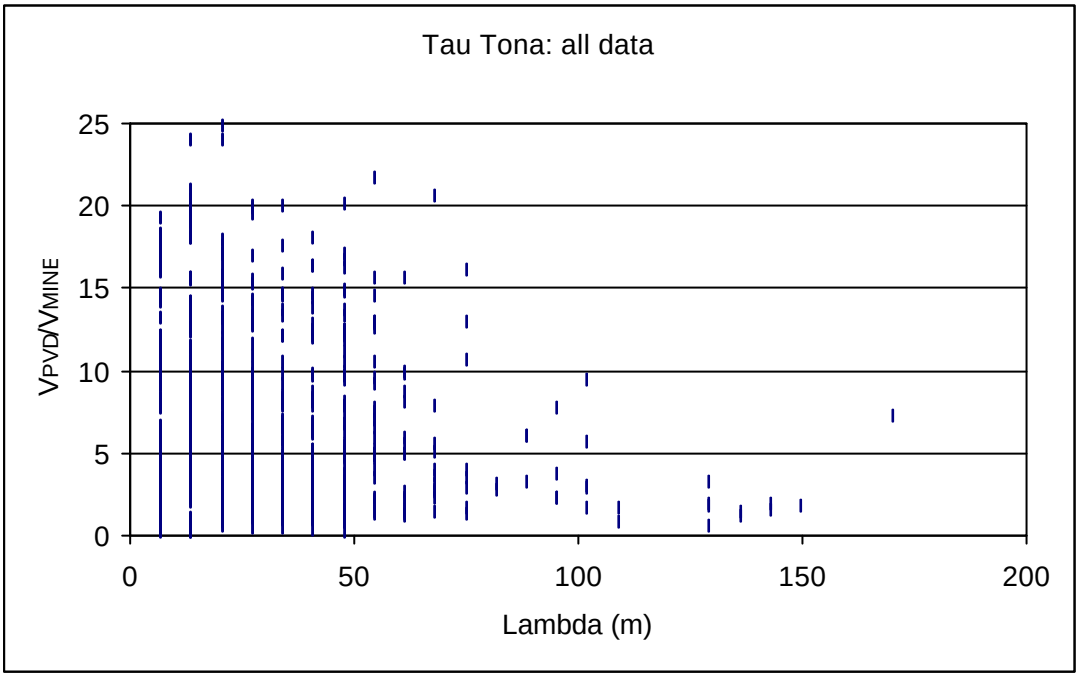

Figure 4.12 Site response obtained from all data recorded at TauTona mine as a function of wavelength Lambda

It is shown in Figure 4.12 that the maximum site response is observed for events with wavelength of about 30 m, which is the same size as a typical Panel length at TauTona mine.

The relationship between the site response and the maximum velocities loading the site is shown in Figure 4.13.

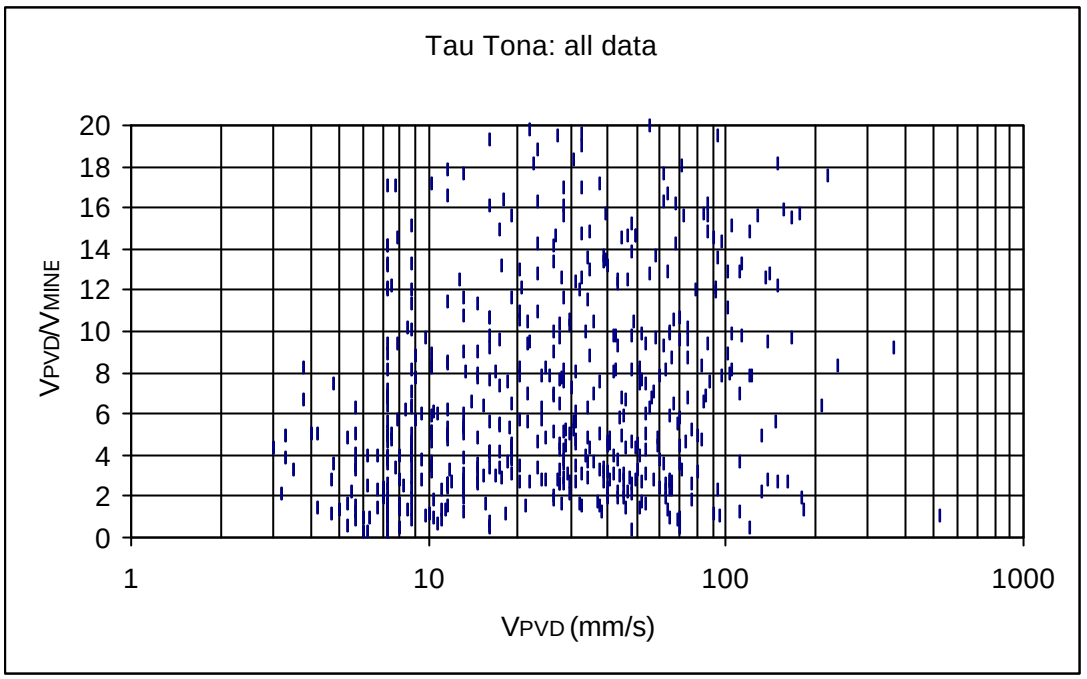

Figure 4.13 Site response as a function of PPVs

It is interesting to note that the site response is not a function of PPV value (Figure 4.13).

4.2 Kloof gold mine

The monitoring period at Kloof gold mine was 659 site days in total, spread over 10 sites. The observations were made between August 2001 and January 2002. A data set corresponding to this time-period was extracted from the mine network and compared to the recorded seismic events.

The site response as a function of the hypocentral distance was calculated for Section 37 – 34 North. Three hangingwall data sites collected from Panels 13050, 13090 and 13096 were combined. The results are shown in Figure 4.14.

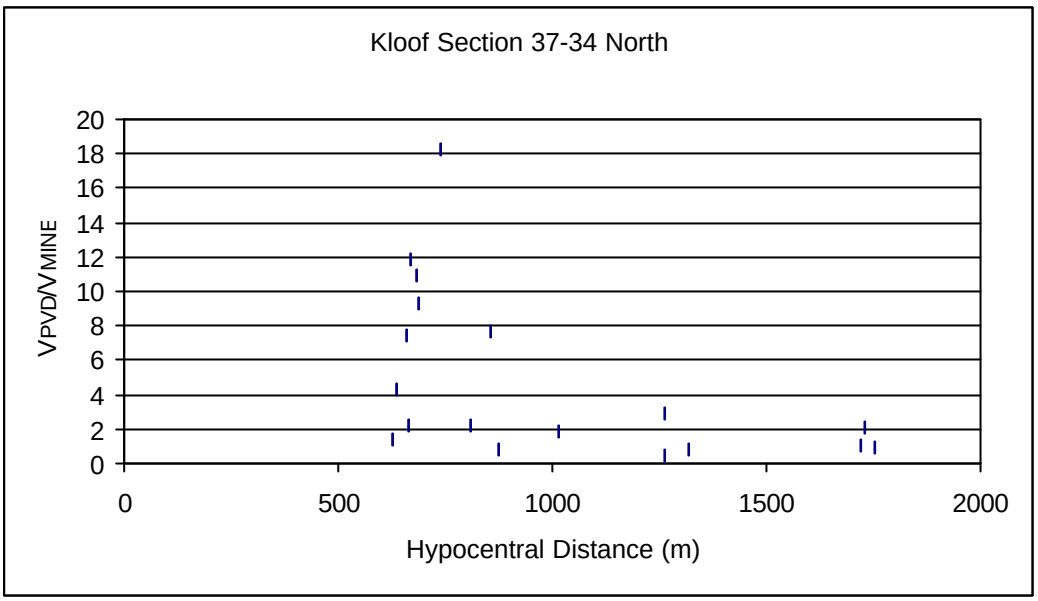

Figure 4.14 Site response as a function of hypocentral distance

In this section, the correlated seismic events plotted in Figure 4.14 have hypocentral distances greater than 500 m and show rapid attenuation of the site response with distance.

The site response as a function of hypocentral distance was calculated for Section 37–34 South. Hangingwall data collected at Panels 13058, 13075 and 13151 were combined. The results are shown in Figure 4.15.

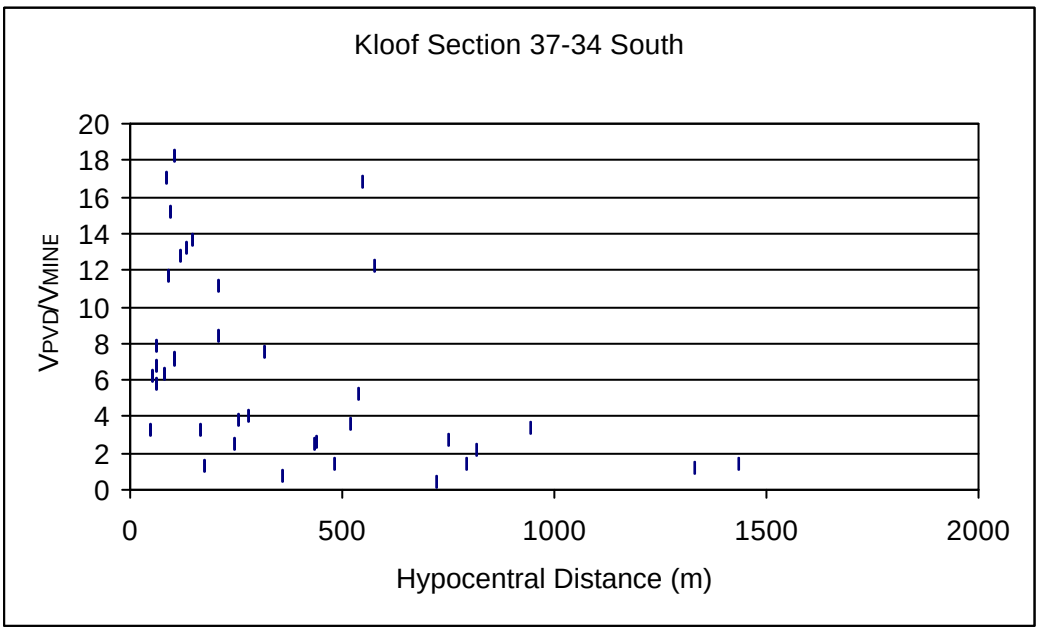

Figure 4.15 Site response as a function of hypocentral distance

The site response for this Section shows attenuation with the hypocentral distance.

Seismic events recorded at Section 37–61 South Panels S1, S2, S3 and S4 were compared to the seismic events recorded by the mine seismic network. The site response estimated for the correlated events is shown in Figure 4.16.

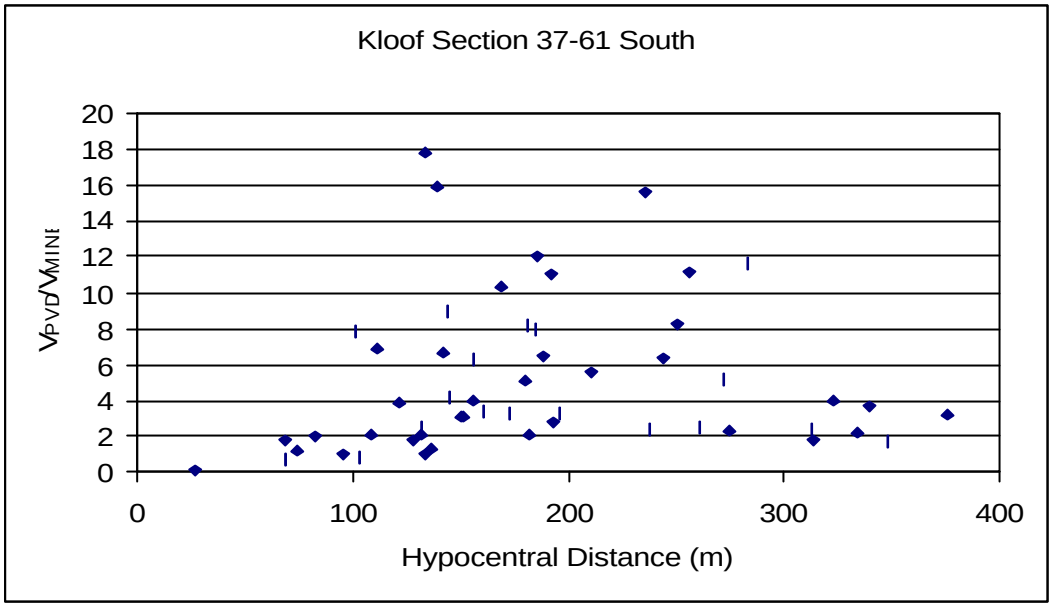

Figure 4.16 Site response as a function of hypocentral distance

All seismic events plotted in Figure 4.16 have hypocentral distances in the range of 0m to 400 m, which falls in the zone of maximum site response. Peak values are visible for hypocentral distances of 150 m and 200 m. However, the overall attenuation of the site response cannot be estimated from this data set.

4.2.1 Kloof: site response outline

The site response estimated over the entire data set accumulated at Kloof mine is discussed in this section. The relationship between the site response in respect to hypocentral distance, source radius, wavelength (Lambda) and maximum velocity is discussed in this section, as well as the relationship between source radius and hypocentral distance, and source radius and magnitude.

The site response as a function of hypocentral distance is shown in Figure 4.17.

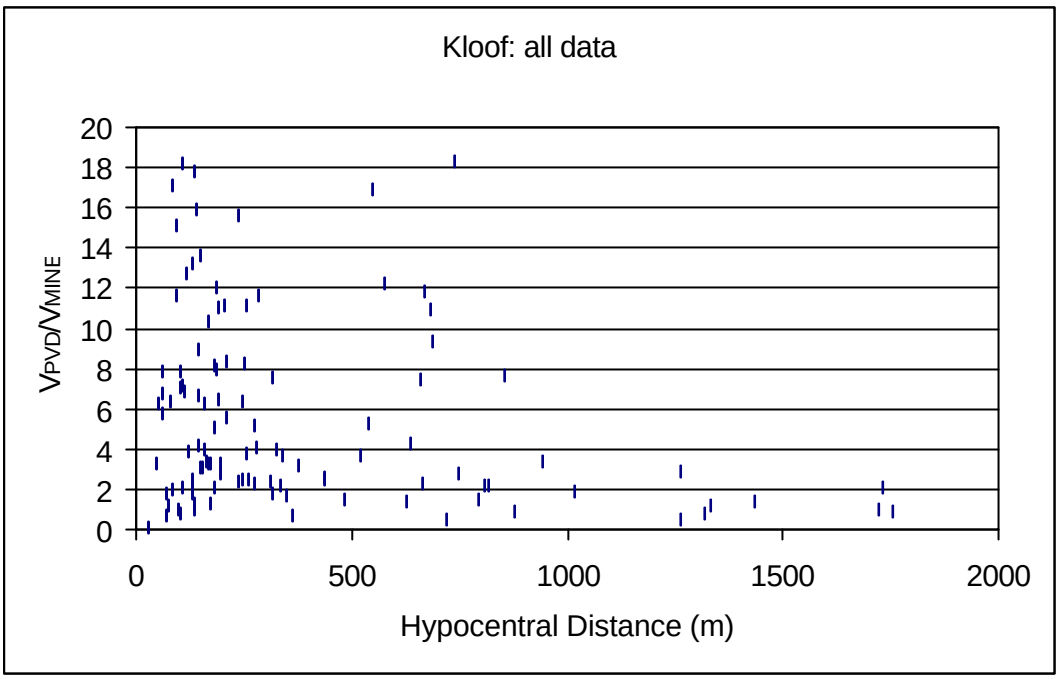

Figure 4.17 Site response as a function of hypocentral distance

The site response estimated over all data recorded at Kloof mine shows attenuation with the hypocentral distance.

The relationship between the site response and the source radius (as estimated by the mine) is shown in Figure 4.18.

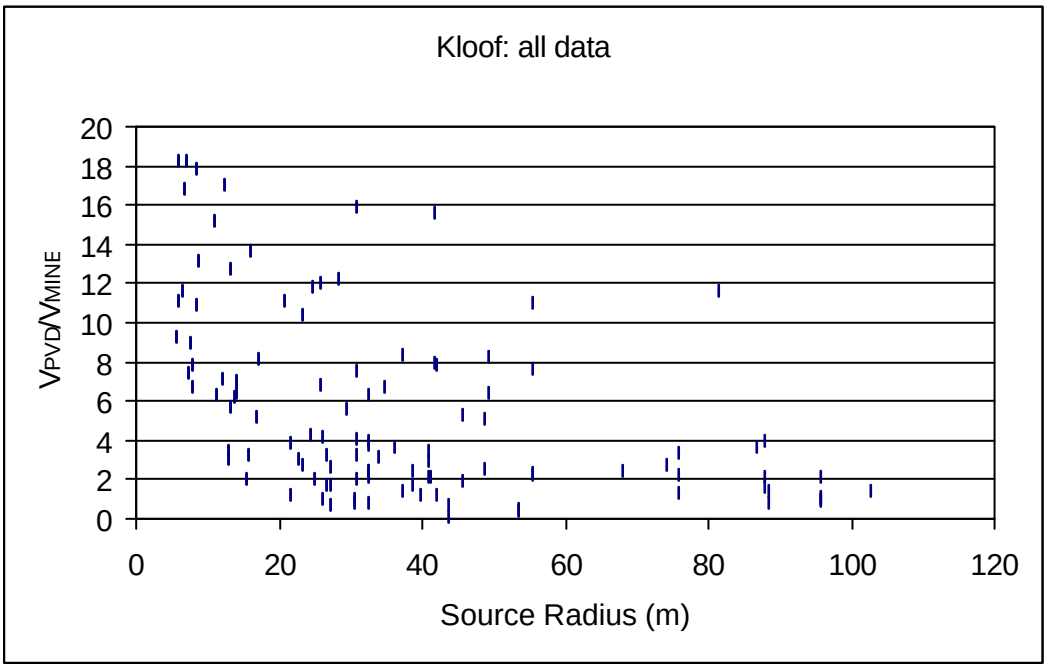

Figure 4.18 Site response as a function of source radius

It is clearly indicated in Figure 4.18 that the maximum site response is observed for source radii of between 5 m and 20 m, and that it then attenuates for bigger source radii.

The distribution of the source radius as a function of the hypocentral distance is shown in Figure 4.19.

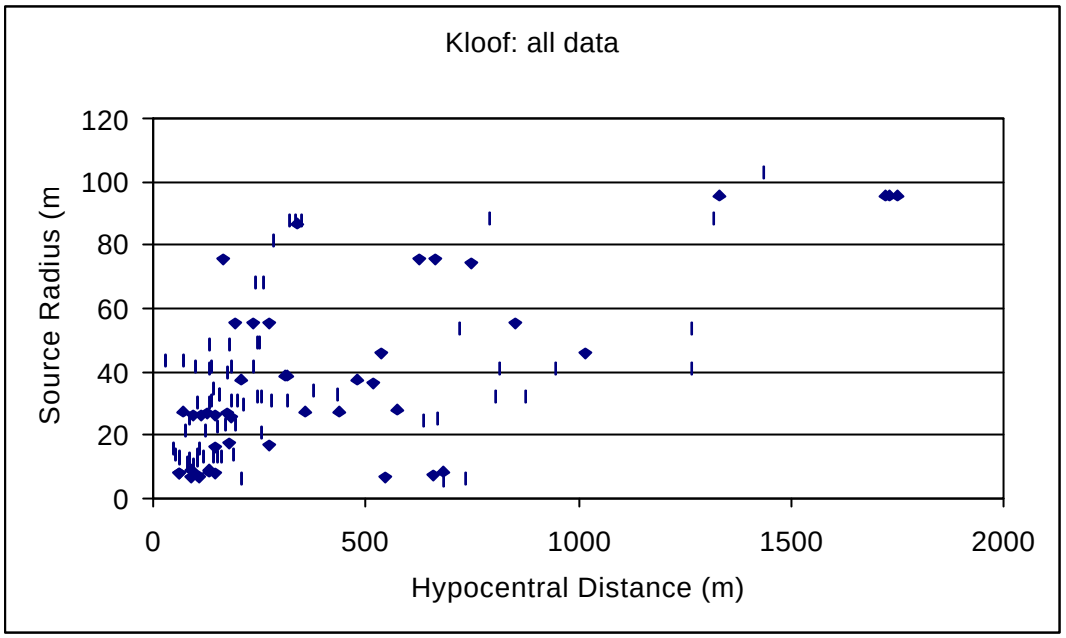

Figure 4.19 Source radius as a function of the hypocentral distance

It is important to notice that the seismic events with source radii of between 5 m and 20 m (see Figure 4.18) have the maximum site response. These events take place within the first 100 m to 200 m from the face. Seismic events with larger source radii (20 m to 60 m) are also obtained in this hypocentral range.

The distribution of a source radius as a function of magnitude is shown in Figure 4.20.

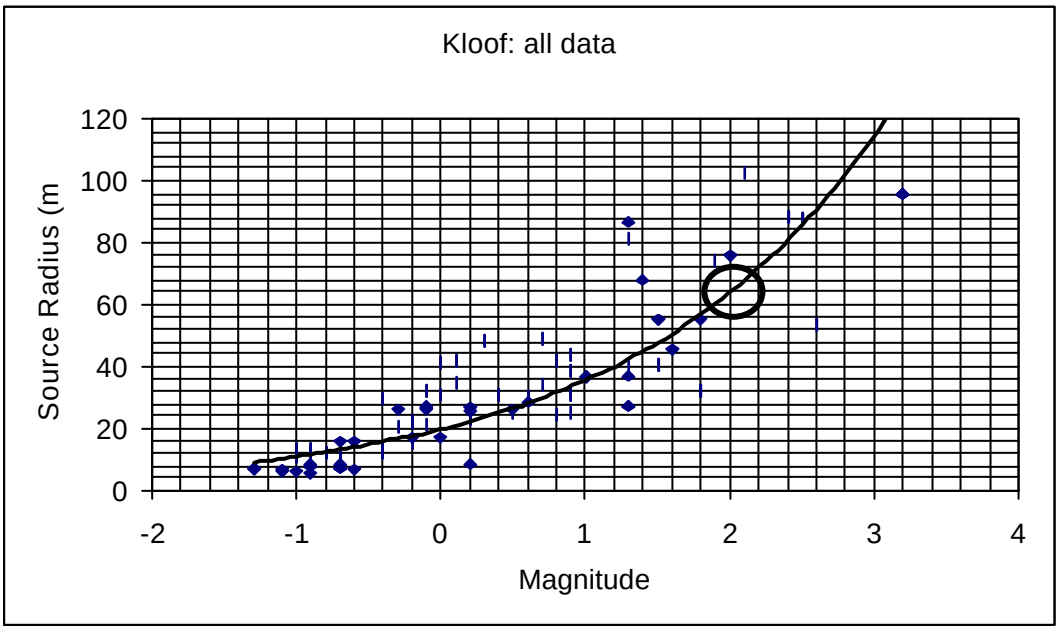

Figure 4.20 Graphical estimation of the source radius range for the "characteristic" damaging events $(M \approx 2.0 \pm 0.2)$

It is estimated from Figure 4.20 that source radii of 59 m to 72 m can be related to events with $M \cong 2.0 \pm 0.2$. These values are significantly higher than the values obtained at TauTona mine and indicate lower stress drop events.

The site response as a function of wavelength (Lambda) is shown in Figure 4.21.

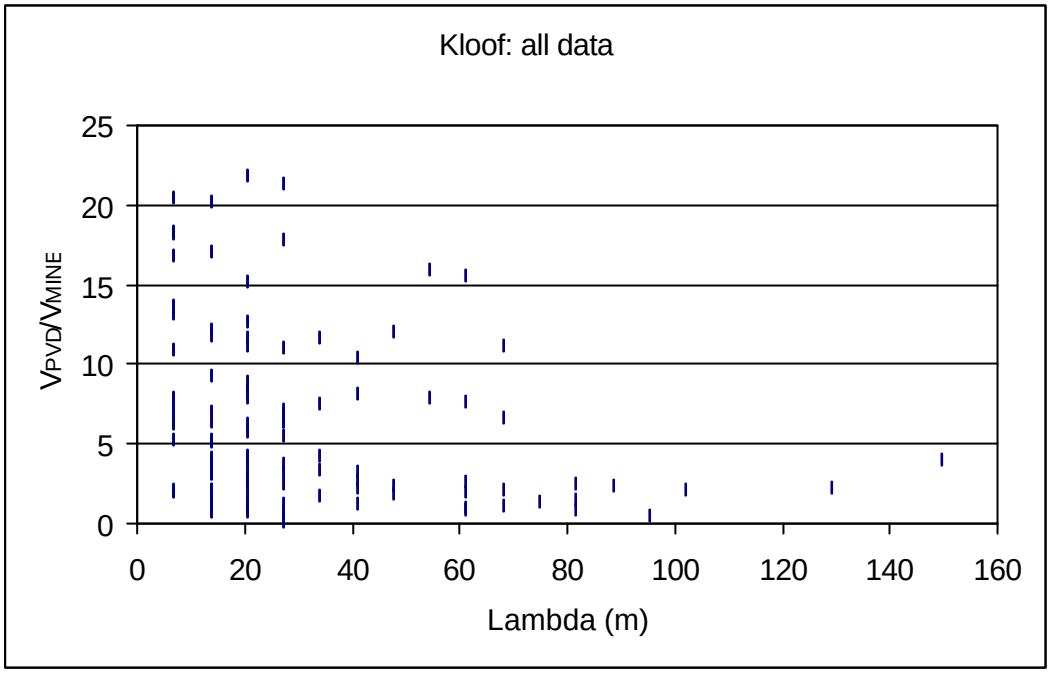

Figure 4.21 Site response as a function of wavelength Lambda

The maximum site response was observed for seismic waves with wavelengths of between 5 m and 25 m (Figure 4.21).

The relationship between the site response and the maximum velocities of correlated events is shown in Figure 4.22.

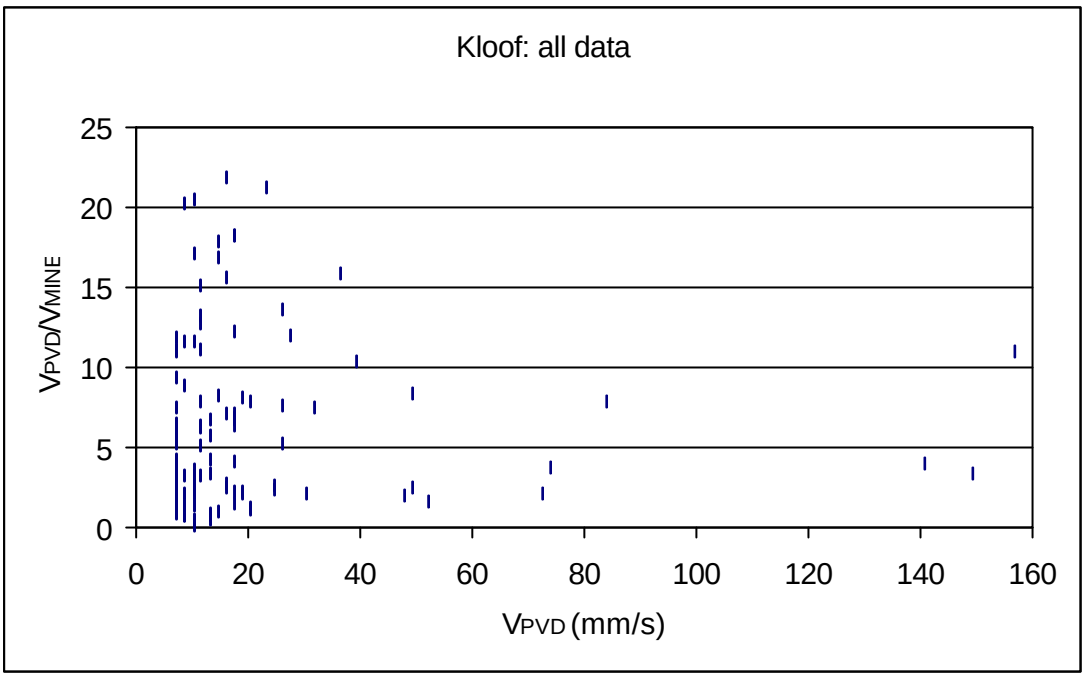

Figure 4.22 Site response as a function of PPVs

Maximum site response is observed for PPVs between less than 25 mm/s.

4.3 Mponeng gold mine

The monitoring period at Mponeng gold mine was 407 site days in total, over seven underground sites. The observations were made between July 2001 and February 2002. A data set corresponding to this time was extracted from the mine network and compared to the data recorded.

The site response as a function of the hypocentral distance was calculated for Section 94 – 44 Panels E4, E5 Top, E5 Bottom and E6. The results are shown in Figure 4.23.

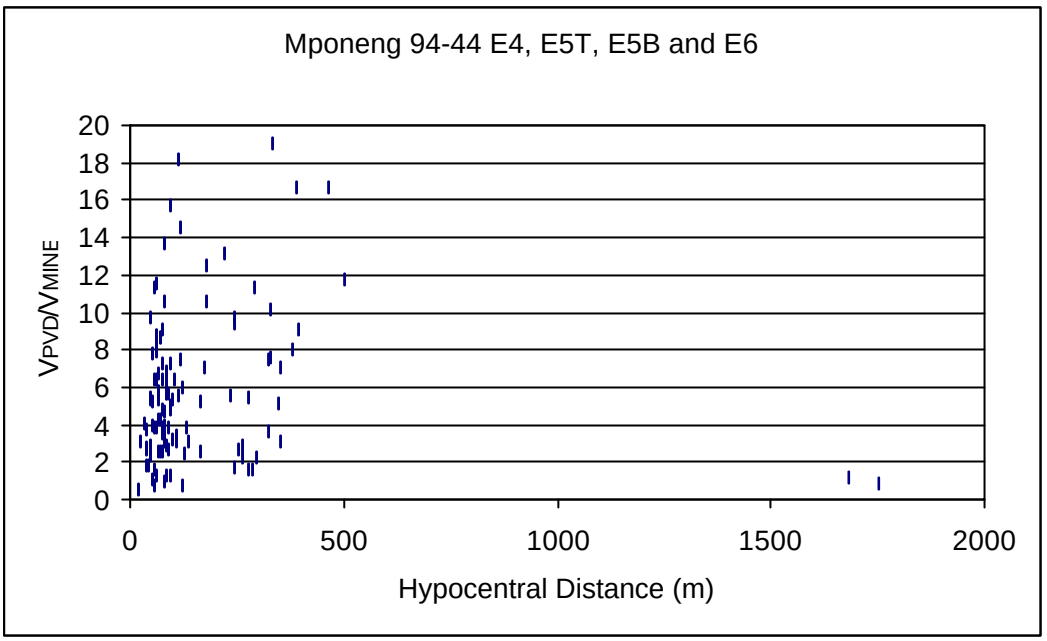

Figure 4.23 Site response a function of hypocentral distance; E4, E5 Top, E5 Bottom and E6

The site response estimated for Section 94 – 44, Panel E7 and Section 94 – IV, haulage is shown in Figures 4.24 and 4.25 respectively.

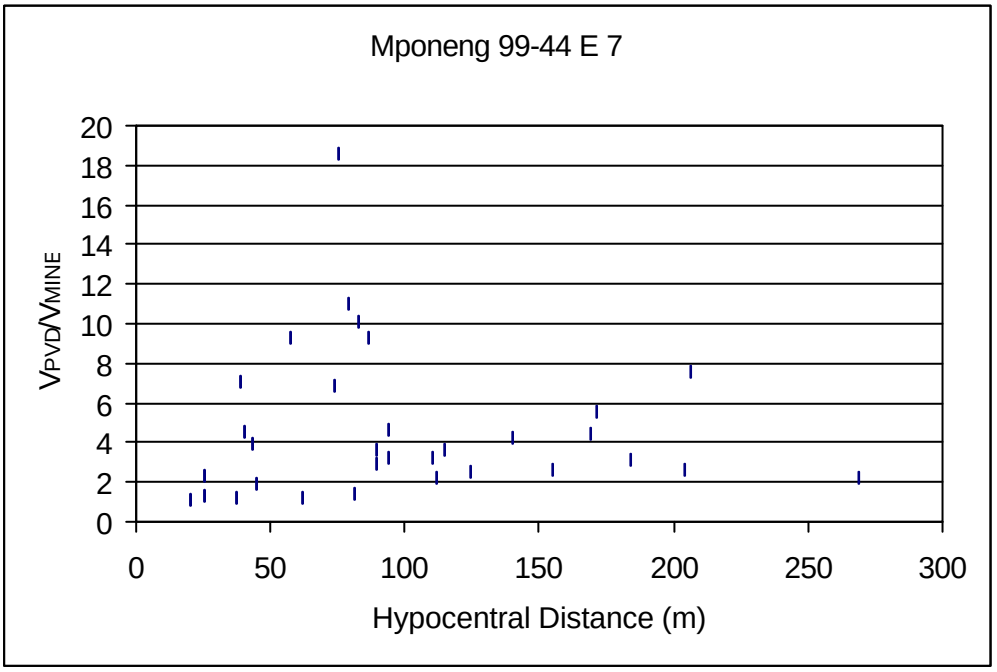

Figure 4.24 Site response as a function of hypocentral distance

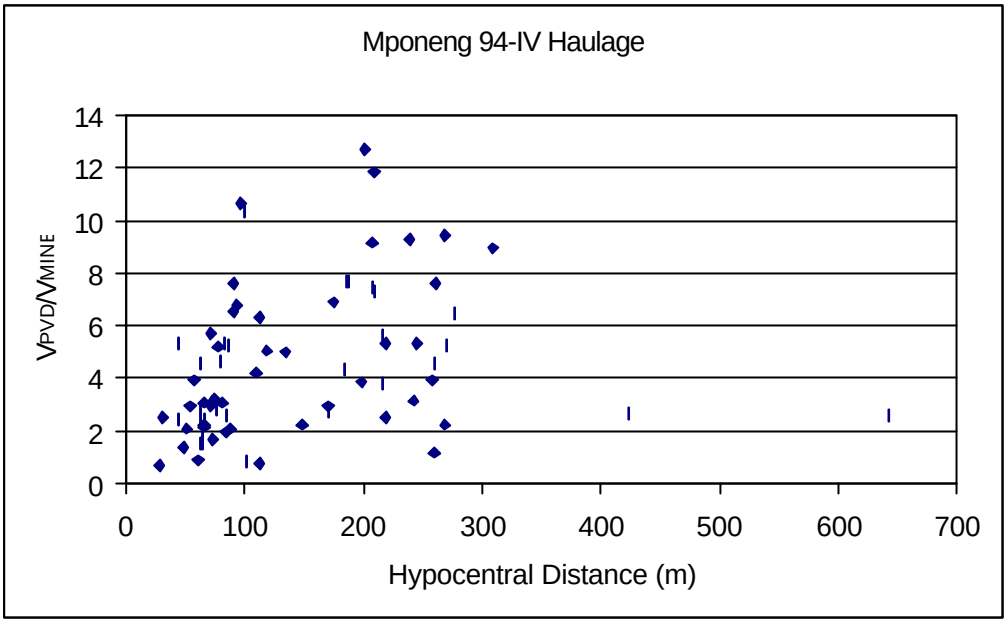

Figure 4.25 Site response as a function of hypocentral distance

The hypocentral distribution for the correlated seismic events is in the range of between 0 m and 300 m. Although a reliable estimation of the site response attenuation for these sites was not possible, a peak of around 80 m for Section 99 – 44 (Figure 4.24) and a peak of between 100 m and 250 m for Section 94 – IV (Figure 4.25) was obtained.

4.3.1 Mponeng: site response outline

The site response estimated over the entire data set accumulated at Mponeng mine is discussed in this section. The relationship between the site response and hypocentral distance, source radius, wavelength (Lambda) and maximum velocity were discussed, as well as the relationship between source radius and hypocentral distance, and source radius and magnitude.

The site response as a function of hypocentral distance is shown in Figure 4.26.

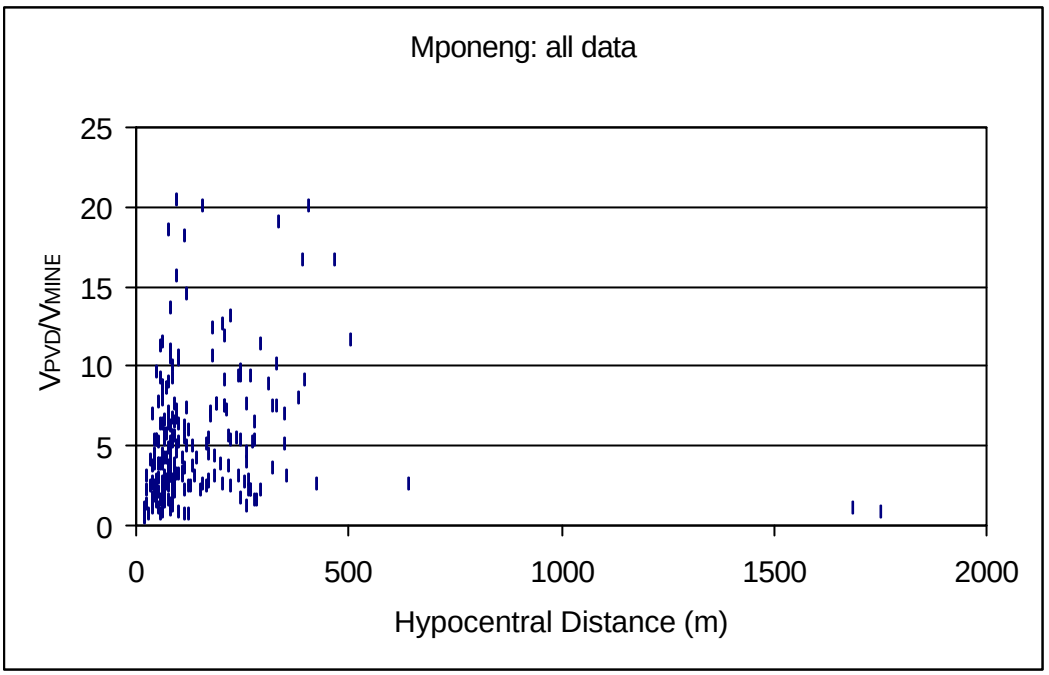

Figure 4.26 Site response as a function of hypocentral distance

The site response shown in Figure 4.26 indicates attenuation with the hypocentral distance. However, the trend is not clearly defined due to the limitation of number of events correlated, for hypocentral distances larger then 500 m.

The site response as a function of the source radius (as estimated by the mine) is shown in Figure 4.27.

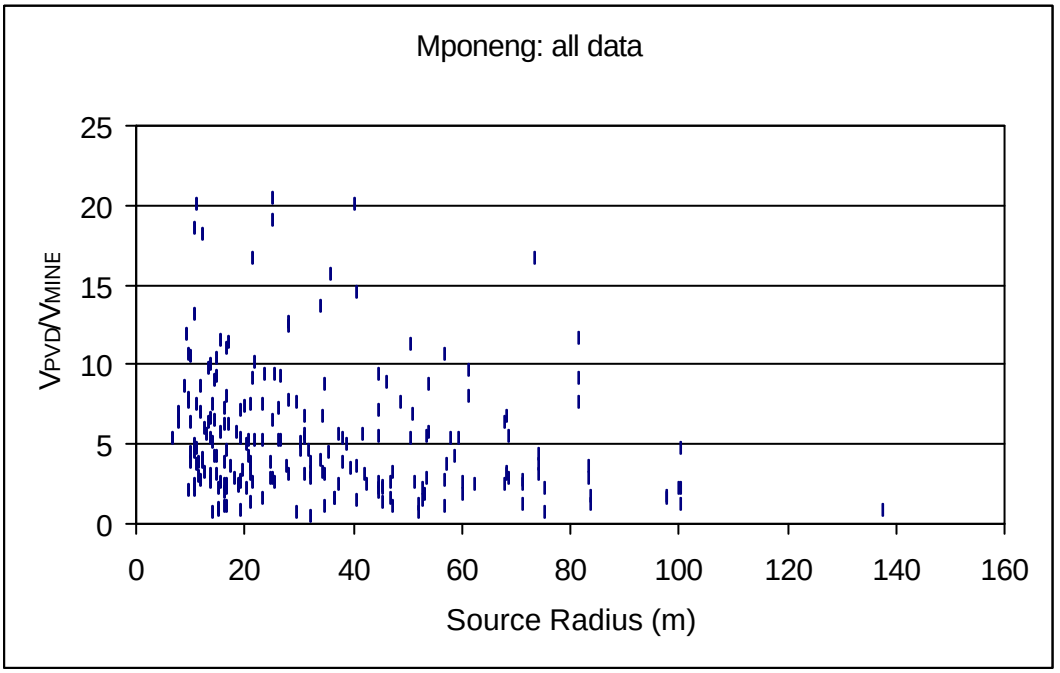

Figure 4.27 Site response as a function of source radius

The distribution of source radii indicates maximum site response for radii of between 10 m and 40 m.

The distribution of source radius as a function of the hypocentral distance is shown in Figure 4.28.

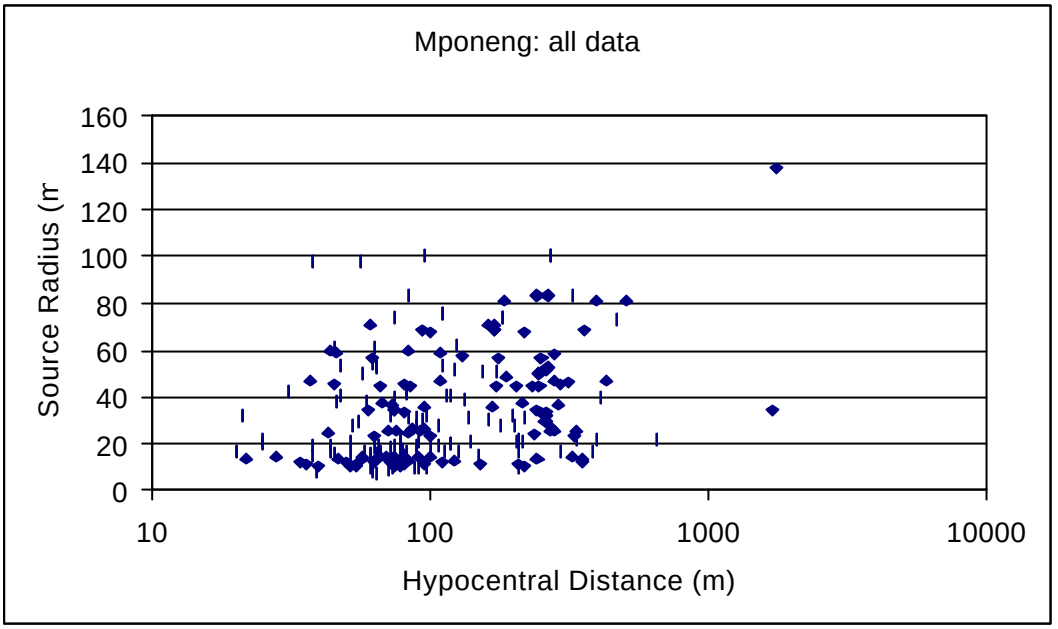

Figure 4.28 Source radius as a function of the hypocentral distance

As is shown in Figure 4.28, the majority of the source radii indicating maximum site response are located from 50 m to 120 m from the face.

The distribution of a source radius as a function of magnitude is shown in Figure 4.29.

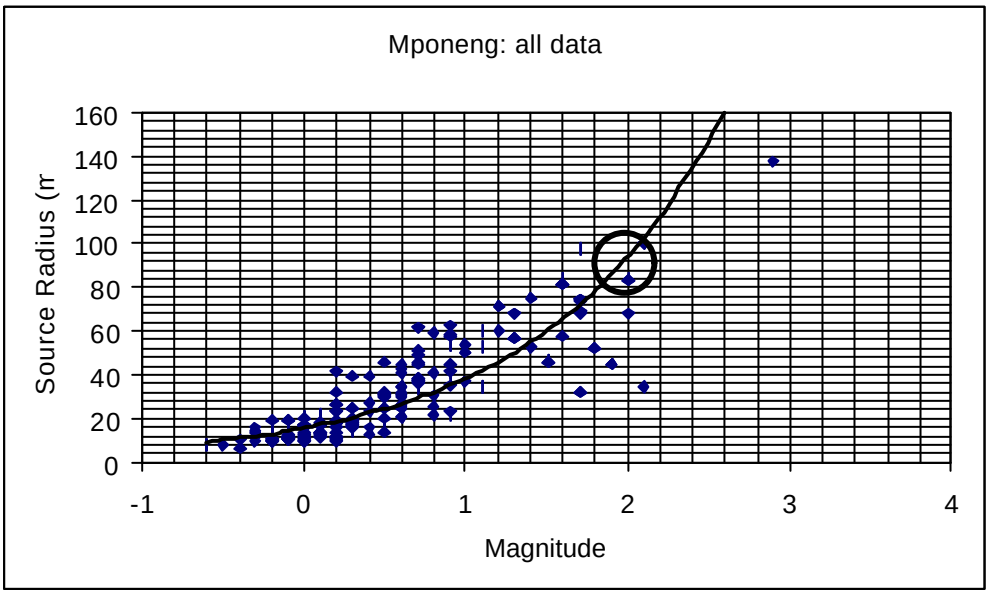

Figure 4.29 Graphical estimation of the source radius range for the "characteristic" damaging events $(M \approx 2.0 \pm 0.2)$

The estimated source radii of 85 m to 104 m can be related to events with $M \cong 2.0 \pm 0.2$ (Figure 4.29). These values are higher than the values obtained at TauTona and Kloof mines, suggesting even lower stress drop events.

The site response as a function of wavelength (Lambda) is shown in Figure 4.30.

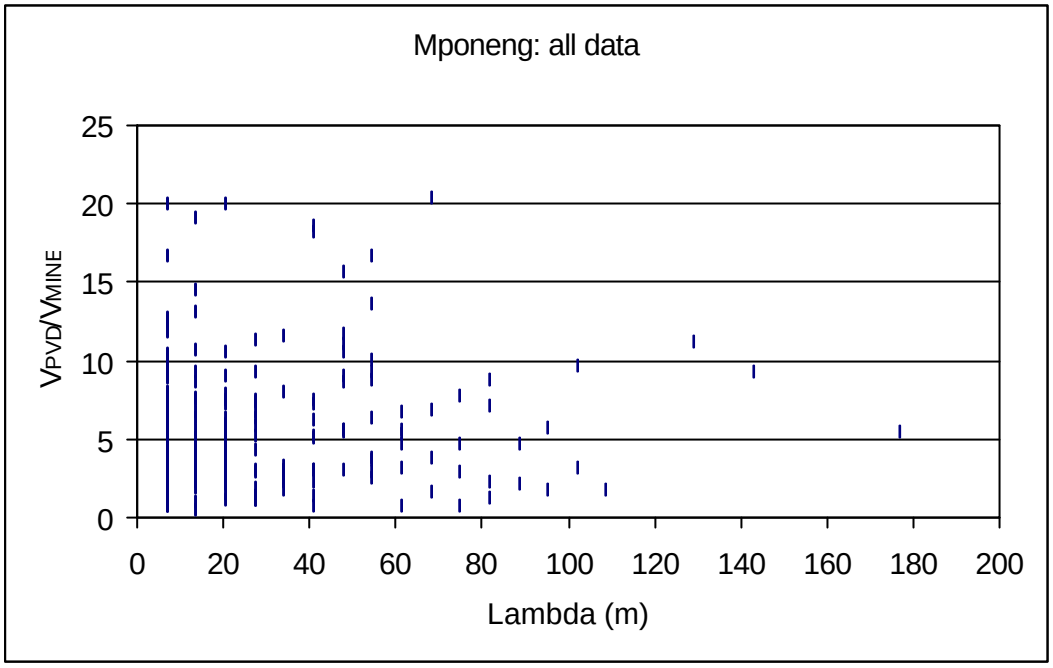

Figure 4.30 Site response as a function of wavelength Lambda

The maximum site response was observed for seismic waves with wavelengths of between 5 m and 20 m (Figure 4.30).

The relationship between the site response and the maximum velocities of correlated events is shown in Figure 4.31.

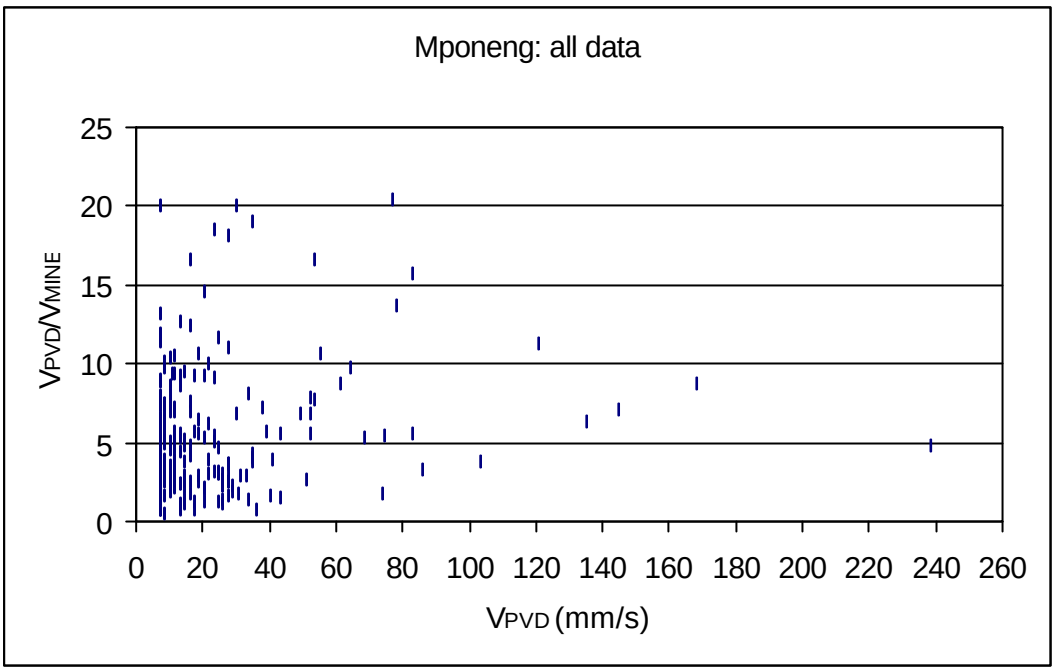

Figure 4.31 Site response as a function of PPVs

Similarly to Kloof mine, maximum site response is observed for PPVs of between 5 mm/s and 25 mm/s (Figure 4.31).

4.4 Conclusions

The site response obtained at the surface of excavations was found to attenuate with the hypocentral distance. The exponential attenuation of the following type;

$$x = a\,e^{-bR} \qquad (4.1)$$

where *a* and *b* are coefficients different for the different geotechnical areas; is proposed. However, due to the limited number of seismic events correlated at hypocentral distances longer then 500 m, the correlation coefficient for the exponential trend line is very low.

The maximum site response was obtained for source radii of between 5 m and 30 m. This range shows slight deviation for different geotechnical areas.

Most of the extreme values of PPVs were recorded in cases were the face-area lay within the source radius.

The majority of the seismic events with source radius of between 5 m and 30 m took place within 200 m from the face.

The corresponding source radius for the “characteristic” damaging event varies significantly with the local geotechnical conditions.

Maximum site response was obtained for seismic waves with a wavelength in the order of 30 m. This wavelength corresponds to the size of a typical mining panel.

Maximum site response was obtained for the smaller PPVs, up to 100 mm/s. The higher PPVs have a minor influence on the site response.

5 Application of a statistical procedure to estimate the probability of the occurrence of a particular PPV

5.1 Mathematical formulation

Many observations of mining-induced seismic events indicate that these events follow the same rules as natural earthquakes. One of the classic techniques used to analyse earthquake data is to plot a Gutenberg-Richter frequency-magnitude graph. Gutenberg and Richter (1944, 1954) introduced the frequency-magnitude relation that can be written as follows:

$$\log n = a - bm \tag{5.1}$$

where n is the number of earthquakes with magnitude m, a is a parameter describing the level of seismicity and b is a parameter describing the number of small events to large events. An example of a Gutenberg-Richter frequency-magnitude distribution computed from data recorded in a deep level gold mine is given in Figure 5.1. The slope of the linear portion of the graph is equal to parameter *b*, and the y-intercept (at x = M = 0.0) of the linear trend gives *a*. The sensitivity of the seismic network, i.e. the magnitude above which all magnitudes are reliably recorded, can be determined from the point where the curve deviates from the linear trend (towards the low end of the magnitude scale). In the example, the sensitivity of the network is approximately M= 1.1.

When the logarithm of velocity is plotted on the x-axis instead of magnitude (Figure 5.1), it is evident that the frequency-log(PPV) distribution shows a similar shape to that of the frequency-magnitude distribution. Because of the similarities in the shape illustrated in Figure 5.1, the methodology described in Gibowicz & Kijko (1995) to estimate maximum magnitudes from Gutenberg-Richter frequency-magnitude distributions is applied to estimate the maximum velocities.

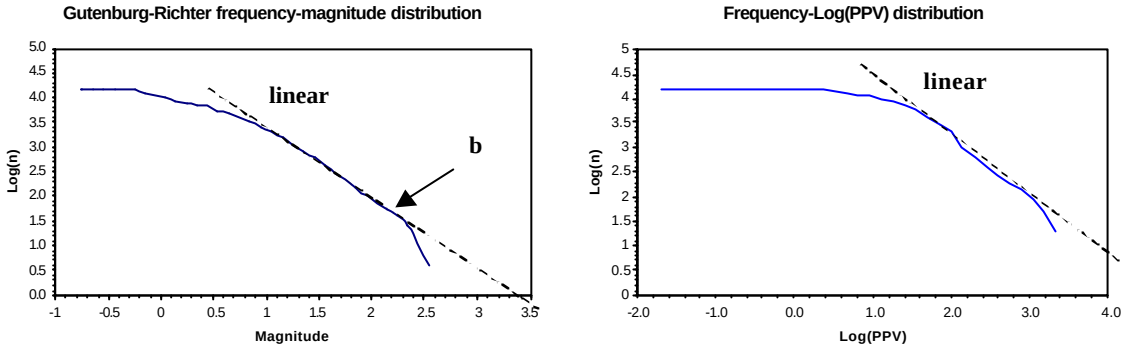

Figure 5.1 Similarities between (left) Gutenberg-Richter frequency-magnitude distribution and (right) frequency-log(PPV) distribution

The mathematical formulation to estimate maximum velocities is given in Appendix A.

5.2 Estimation of peak particle velocity

Standard statistical procedures generally involve plotting the distribution of the data, and on the basis of the shape of the distribution, various other quantities such as the probability density function and cumulative distribution can be calculated. In this context, 'standard' is used to describe those methods that do not include extreme value statistics. These standard methods assume that the population has been adequately sampled, and that each data point has been sampled or recorded with equal accuracy.

However, it is the nature of the distribution of seismic data that the extreme values (i.e. the low and high end of the distribution of the data set) are undersampled. The low end of the distribution of seismic data is always limited by the instrumentation and/or the noise level. The high end of the distribution is controlled by the recording period and the physics of the earthquakes. The recording period would have a significant impact on the shape of the upper end of the distribution – if the recording instruments do not log data for a long enough period, it is possible that no events having extreme values (on the high end) would be recorded. These factors would affect the shape of the distribution of a data set and statistical parameters such as the mean and standard deviation would lose their meaning. For example, the mean magnitude calculated from all the data in Figure 5.1 would be less than that computed from the data set containing magnitudes above the minimum magnitude.

In Figure 5.2, for example, at first glance, the distribution of peak particle velocities recorded at TauTona could be classified as log-normal distribution. However, closer inspection of the low end of the distribution shows anomalous jagged trends, which, could be artefacts introduced by the data acquisition hardware. This highlights the importance of introducing a minimum value above which the data is reliably recorded.

The distributions of peak particle velocities recorded at Kloof (Figure 5.3) and Mponeng (Figure 5.4) show a shape quite different from the apparently log-normal distribution of peak particle velocities recorded at TauTona. In all cases, the same instruments were used to acquire the data, but some instruments were left in the stopes longer than others, resulting in the larger events being stored preferentially to the smaller events (i.e. graceful decline). The longer the

instruments are left underground, the more the minimum increases. Additionally, the Kloof and Mponeng recording periods were significantly lower than that of TauTona (compare the recording period of 2 437 site days at TauTona to the 659 and 403 sites days at Kloof and Mponeng) and as a result, it is likely that the high ends of the distributions are undersampled.

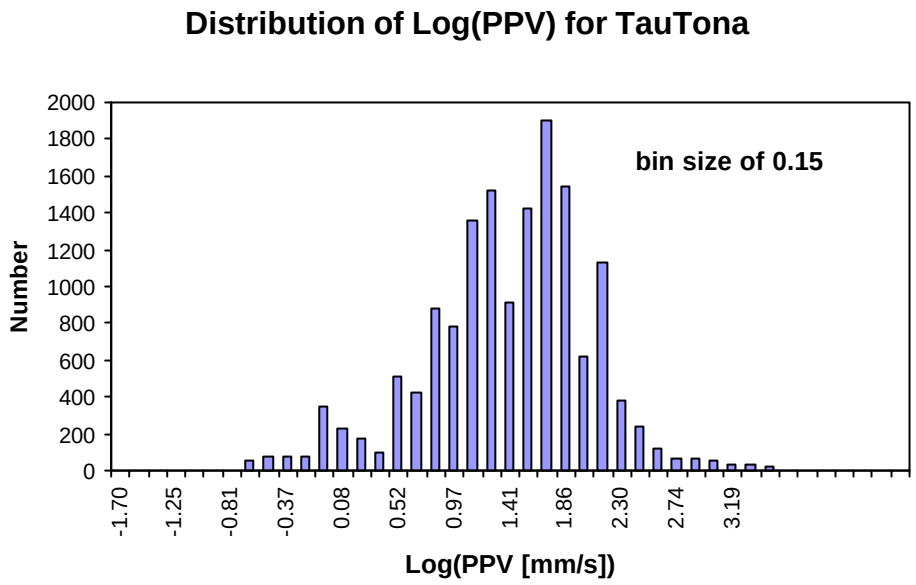

Figure 5.2 Distribution of log(PPV) for TauTona (15 139 data points)

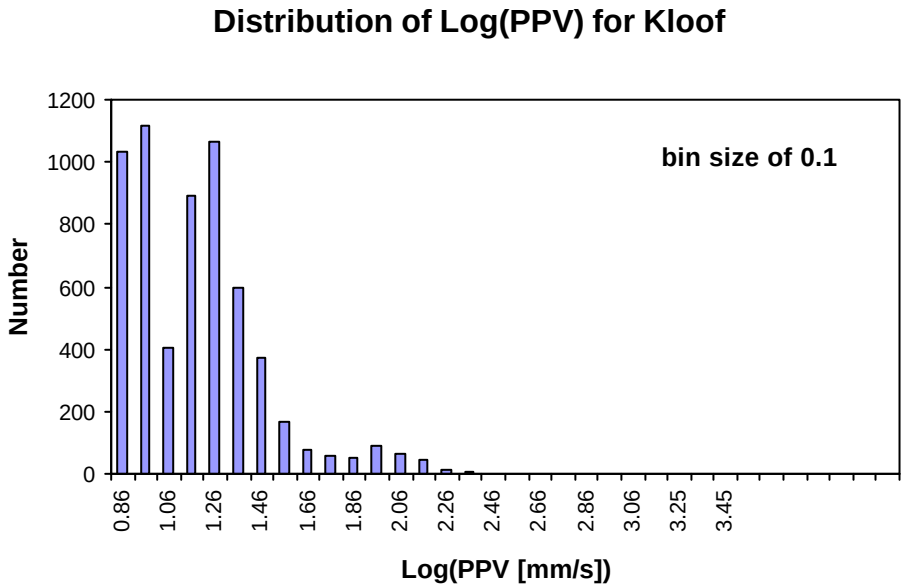

Figure 5.3 Distribution of log(PPV) for Kloof (6 066 data points)

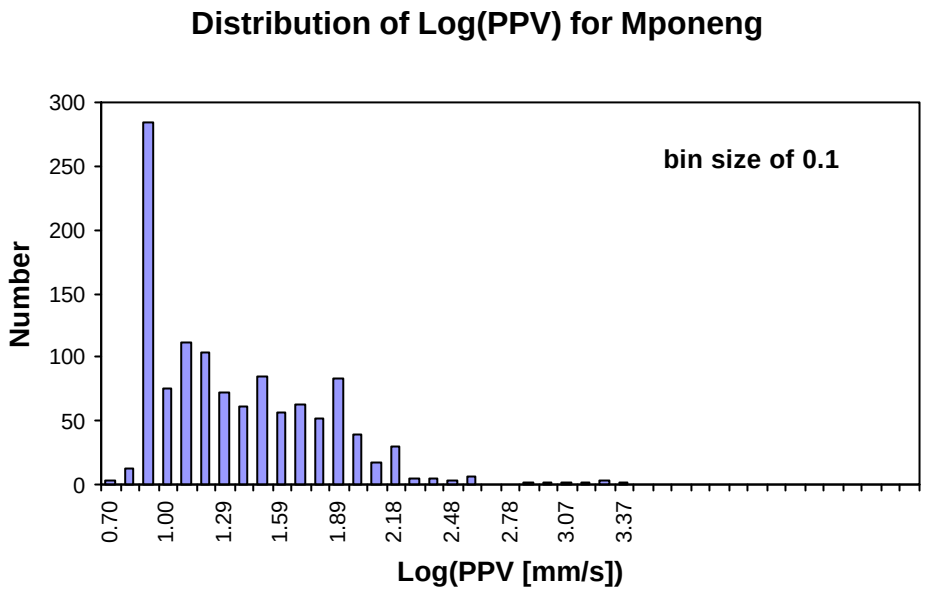

Figure 5.4 Distribution of log(PPV) for Mponeng (1 183 data points)

Frequency-log(PPV) curves were plotted for TauTona, Kloof and Mponeng (Figure 5.5, Figure 5.6, and Figure 5.7). To plot these curves, the data (log(PPV)) were binned, the number of events having log(PPV) within the bin was calculated and the results cumulated. To estimate the maximum log(PPV), the maximum-likelihood procedure described in the Appendix A was applied.

Two curves were fitted to the data. Firstly, a minimum log(PPV) was introduced and the unbounded cumulative distribution function computed (see Appendix A). The maximum-likelihood curve was then calculated. As noted previously, this approach has a significant shortcoming in that no maximum is considered – the effect of this is particularly evident in the TauTona data set where the curve fit predicts an unrealistically high PPV. Secondly, a minimum and a maximum were used, and the cumulative distribution function was calculated using the bounded function. Because of the introduction of the maximum, the curve fit is no longer linear, but bends downwards towards the higher end of the distribution. It is the opinion of the researchers of the project that the maximum likelihood fits that use both a minimum and a maximum are more accurate than those using only the minimum, because it is thought that an upper limit to the peak particle velocity must exist.

Unfortunately, selection of the minimum and maximum is subjective, and as a result, the trend lines presented in this section are not unique. The minimum was selected as the point where the curve deviates from the linear trend towards the low end of the scale (an example is given in Figure 5.1). A number of maxima were selected, and the value that gave the 'best' visual curve fit was selected as the maximum. In some cases, for example, the Mponeng data set, selection of the minimum log(PPV) has a significant impact on the maximum likelihood trend line. To illustrate this, two curves fits for Mponeng are shown in Figure 5.7. In Figure 5.7(a) a minimum PPV of 24.61 mm/s was used, whereas in Figure 5.7 (b) a minimum of 38.81 mm/s was used. It is suggested that the more conservative graph be used to estimate peak particle velocities *viz*. Figure 5.7(b).

At this stage, some general comments regarding the curve fits are pertinent. The maximum likelihood trend using a maximum and a minimum appear to fit the data recorded at TauTona very well, whereas the trend calculated using just the minimum predicted unrealistically high

PPVs (Figure 5.5). Both the maximum likelihood trends (i.e. calculated using both a minimum, and a minimum and a maximum) fit the data recorded at Kloof and Mponeng fairly well (Figure 5.6 and Figure 5.7). However, for both curve fits for both mines, since there is so little data at the high end of the velocity range, the fits are largely controlled by the data above the minimum but towards the lower end of the velocity range. As a result, the trend lines fall below the data curve at the high end of the velocity range.

The frequency-log(PPV) distributions for Kloof and Mponeng (Figure 5.6 and Figure 5.7) appear to be bimodal. The bimodality is less pronounced in the frequency-log(PPV) distribution plotted for TauTona (Figure 5.5). The source of the bimodality is not known – it could be an effect introduced by the instrumentation or an indication of a fundamental difference in the mechanisms of failure. As a result, it is not known what an 'ideal' frequency-PPV plot should look like and the selection of the minimum and maximum is subjective. It is strongly suggested that further work be done to investigate the source of the bimodality so that the appropriate statistics can be applied.

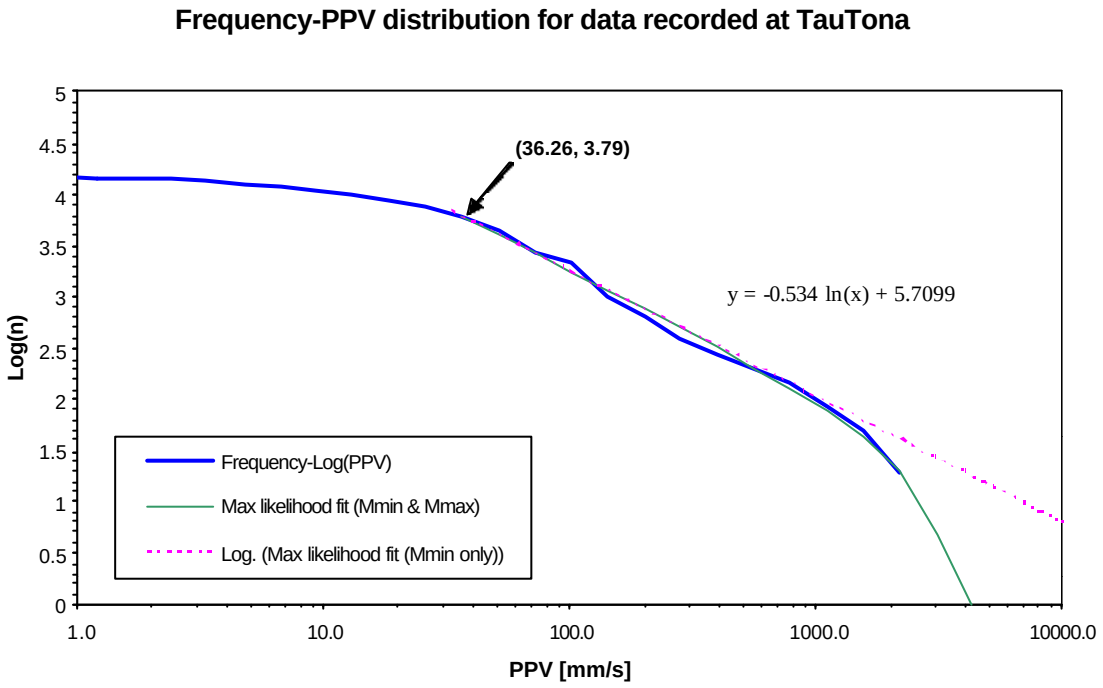

Figure 5.5 Frequency-PPV distribution for peak particle velocities recorded at TauTona (15 139 data points recorded during 2 437 site days)

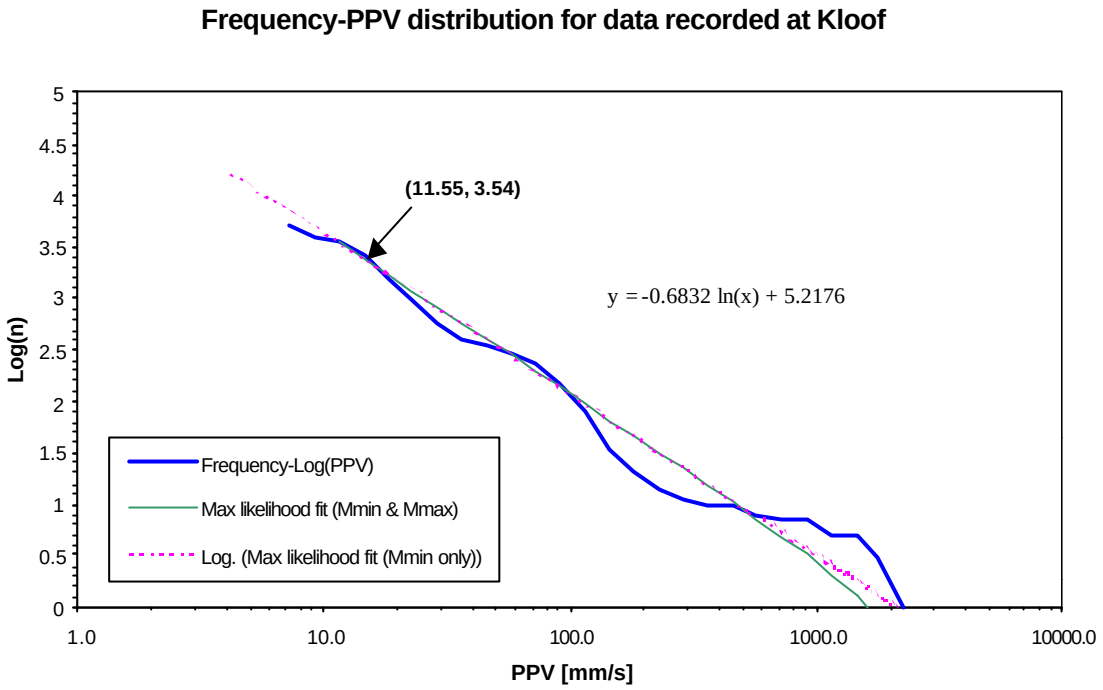

Figure 5.6 Frequency-PPV distribution for peak particle velocities recorded at Kloof (6 066 data points recorded during 659 site days)

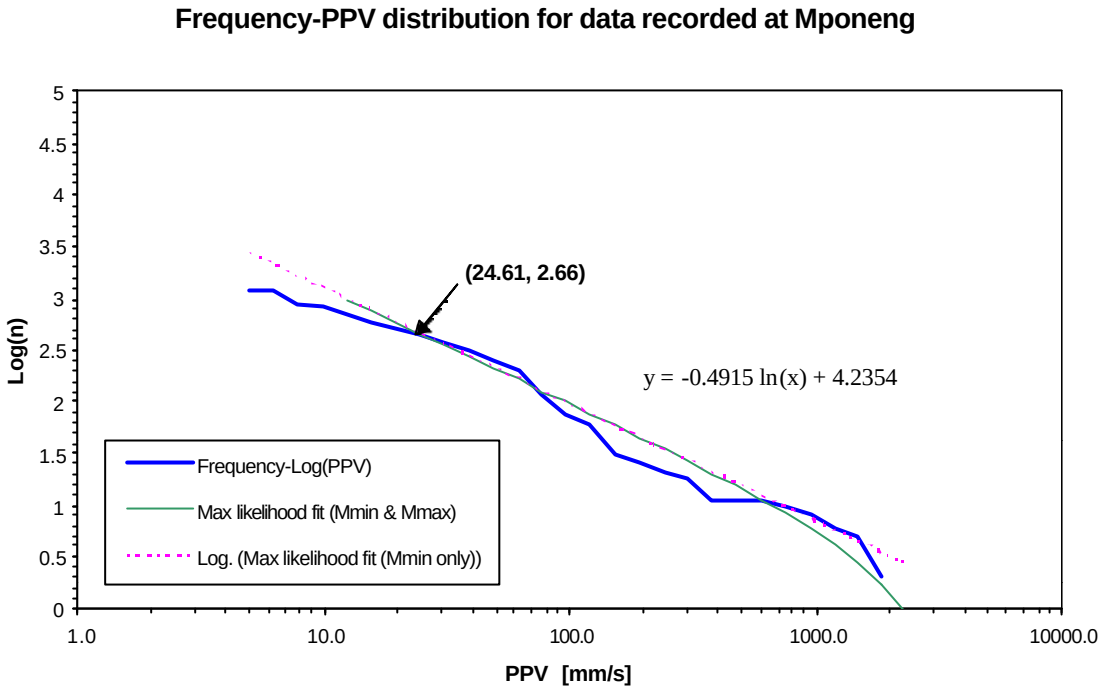

(a)

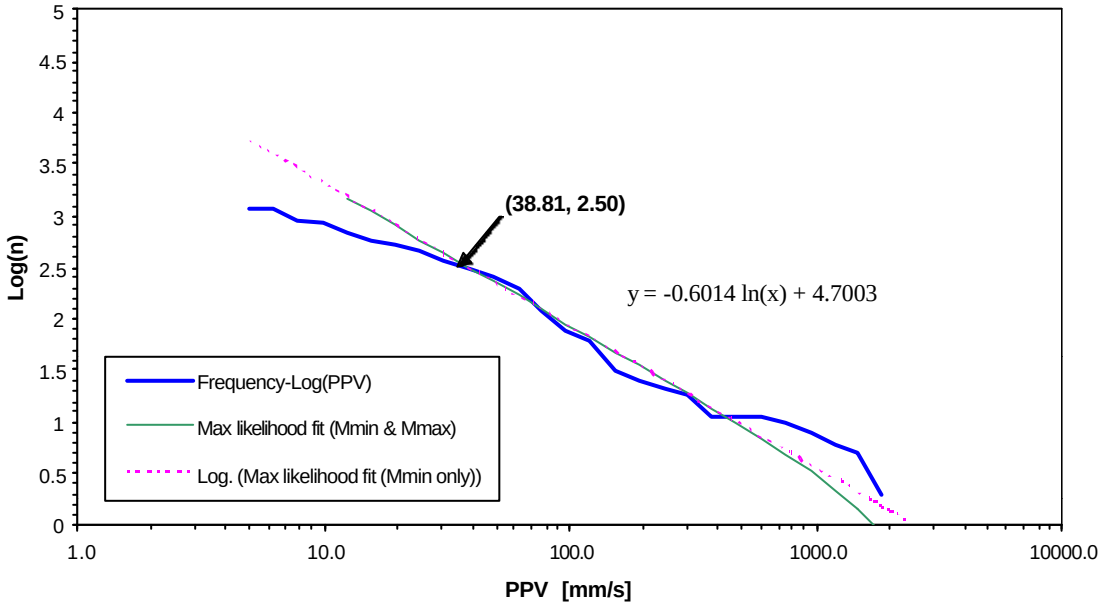

(b)

Figure 5.7 Frequency-PPV distribution for peak particle velocities recorded at Mponeng (a) minimum PPV = 24.6 mm/s; (b) minimum PPV = 38.8 mm/s (1 183 data points recorded during 403 site days)

The maximum expected PPVs estimated using the maximum likelihood approach and the maximum recorded PPVs are given in Table 5.1.

Table 5.1 Maximum recorded and estimated PPVs for TauTona, Kloof and Mponeng

Mine	Recording period [site days]	Maximum recorded PPV [mm/s]	Maximum estimated PPV [mm/s]	
			Max likelihood fit using a min	Max likelihood fit using a min & max
TauTona	2 437	3 053.8	*	3 548.1
Kloof	659	2 845.9	2 073.5	3 311.3
Mponeng	403	2 338.1	5 528.4	3 162.3

* The estimation of PPV using the maximum likelihood fit with a minimum only was not possible for this data set.

Figure 5.8 shows the cumulative distribution of PPV for TauTona, Kloof and Mponeng calculated using maximum likelihood with a minimum and a maximum. These curves show how the data is distributed above the minimum. For example, 80% of the PPVs recorded at Kloof (above the minimum) have values of 30 mm/s and below. These curves allow comparisons to be made between the three mines: TauTona and Mponeng show similar cumulative distributions, whereas, in comparison, Kloof shows a lower percentage of high PPVs.

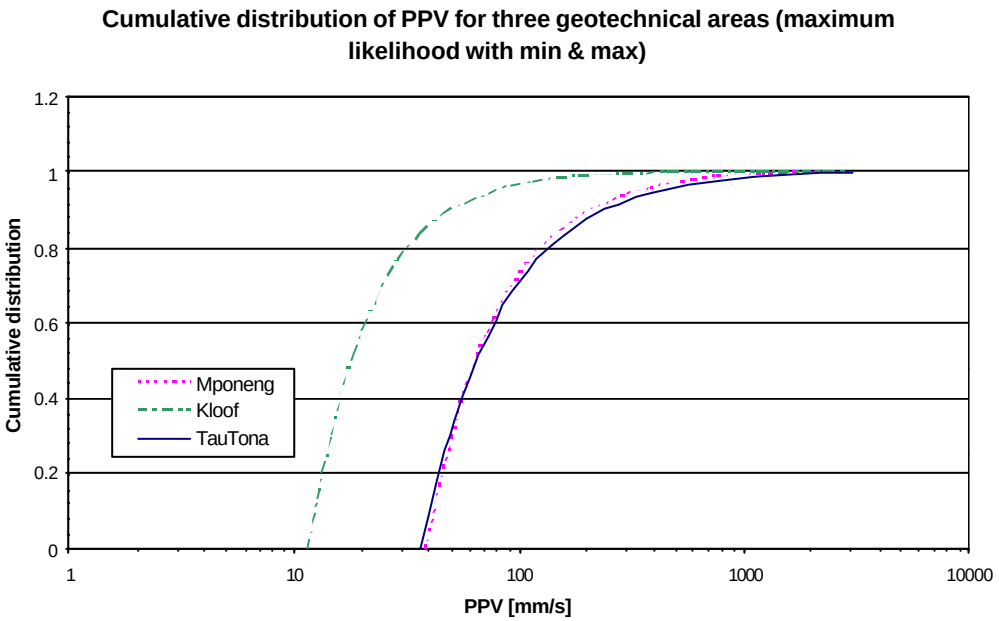

Figure 5.8 Cumulative distribution of PPV for TauTona, Kloof and Mponeng calculated using maximum likelihood with a minimum and a maximum

Table 5.2 gives the recorded number of events exceeding a particular PPV for TauTona, Kloof and Mponeng. 'Total' refers to the total number of site days i.e. total number of days during which data was recorded. For example, if 3 PVDs were installed in three different panels and recorded data for a week, the total number of sites days would be three weeks. In the table, the recorded number of events exceeding three selected PPV levels per year is reported. TauTona had the highest number of events exceeding 1 000 mm/s (18.7 events per year) whereas the lowest number of events exceeding this level was recorded at Kloof (3.9 events per year). Mponeng had 8.2 events exceeding 1 000 mm/s per year. For the 2 000 mm/s level, TauTona once again showed the highest number of events exceeding this level (4.6 per year), whereas Kloof and Mponeng had similar numbers of events exceeding 2 000 mm/s (1.7 and 1.8 events per year, respectively). 0.4 events exceeding 3 000 mm/s were recorded at TauTona whereas no events exceeding this value were recorded at Kloof and Mponeng.

Table 5.2 Recorded number of events exceeding a particular PPV for three geotechnical areas

Mine	Recorded number of events exceeding a particular PPV					
	1 000 mm/s		2 000 mm/s		3 000 mm/s	
	Total	Per year	Total	Per year	Total	Per year
TauTona 2437 site days	125	18.7	31	4.6	3	0.4
Kloof 659 site days	7	3.9	3	1.7	0	0
Mponeng 403 site days	9	8.2	2	1.8	0	0

5.3 Summary of observations

- The maximum likelihood curve fits using a maximum and a minimum value of PPV appeared to match the data recorded at TauTona very well, whereas the trend calculated using just the minimum predicted unrealistically high PPVs.

- The curve fits to PPV data recorded at Kloof and Mponeng were less satisfactory, particularly towards the high end of the velocity range. This is possibly as a result of the recording period being four to six times lower than that of TauTona.

- The maximum recorded PPVs were 3 054 mm/s at TauTona; 2 846 mm/s at Kloof and 2 338 mm/s at Mponeng.

- The maximum expected PPVs estimated using the maximum likelihood approach (with a minimum and a maximum) were 3548 mm/s at TauTona; 3311 mm/s at Kloof and 3 162 mm/s at Mponeng.

- The frequency-log(PPV) distributions for Kloof and Mponeng appeared to be bimodal. The source of the bimodality is not known, and could be an effect introduced by the instrumentation or an indication of a fundamental difference in the mechanisms of failure. It is strongly suggested that further work be done to investigate the source of the bimodality so that the appropriate statistics can be applied.

5.4 Recommendations for future work

Application of PVD with expanded capability to record full waveforms of largest events to check validity of strongest ground motions and enable additional seismological analysis in the frequency domain.

6 Investigation into the improved rockburst support criteria for stopes and tunnels

6.1 Review and evaluation of dynamic response of support systems used in stopes and tunnels

6.1.1 Rate dependence of elongates and packs

Various studies (Roberts et al., 1987; Daehnke et al., 1998) have been conducted to quantify the force-deformation characteristics of elongates and packs installed in working stopes underground. It has been shown that the force-deformation behaviour of the support units can be significantly downgraded compared to the laboratory-derived force-deformation curves. To clarify this discrepancy, a series of systematic laboratory test (Roberts et al., 1987) were carried out to assess the influence of various parameters, including temperature, humidity, timber quality and loading rate, on the performance of timber props. A comparison between the laboratory and underground test results found that the parameter that had the greatest effect in reducing the support load, was the difference in loading rate.

The materials constituting a particular support type or the yielding mechanisms can render the support performance loading-rate dependent. For example, the strength of timber is generally known to be rate dependent and at higher loading rates the strength of the timber-based support element increases. This implies that support units, such as timber elongates and packs, offer higher support resistance when tested in the laboratory compared to their underground performance. Conversely, during rapid stope convergence typically encountered during rockbursts and dynamic events, the support resistance of packs and timber props is increased significantly.

During rapid compression, props, which make use of frictional yielding mechanisms, result in lower support resistance. This is because the coefficient of dynamic friction is generally lower than the coefficient of static friction. An example of this can be seen in the force-deformation curve of the Rocprop in Figure 6.1.

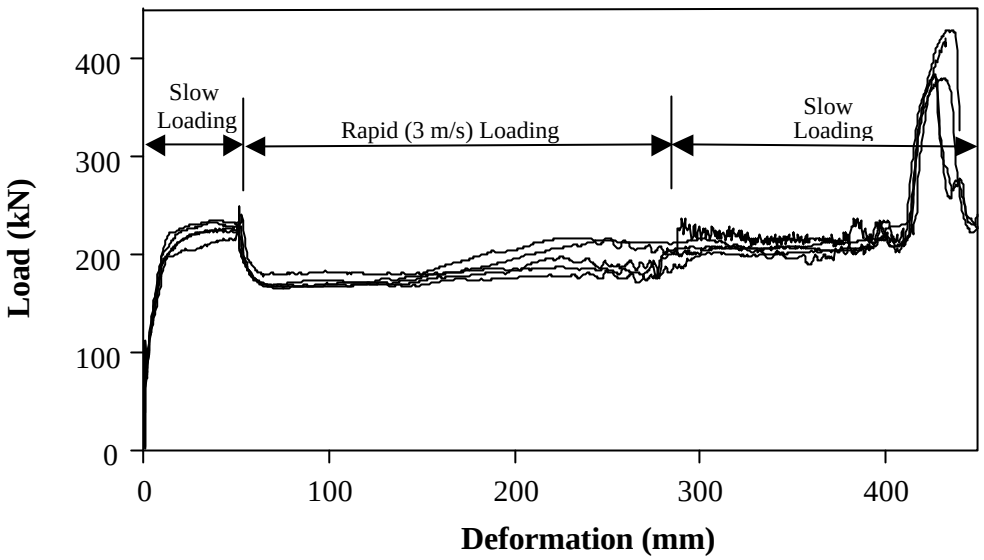

Figure 6.1 Force-deformation curves of five 1.2 m Rocprops that were initially loaded slowly, then rapidly, and then slowly again (Daehnke et al., 1998)

Correction factors have been derived that allow rock engineers to assess the likely underground support performance of a particular support unit from laboratory-derived force-deformation curves. The following equations adjust the support resistance of timber elongates and packs for loading rate:

Timber Elongates:

(Roberts, 1995)

$$F_{u/g} = F_{lab}\left[m\log\left(\frac{v_{u/g}}{v_{lab}}\right)+1\right] \tag{6.1}$$

Timber Packs:

(Taggart, 1994, 1994a)

$$F_{u/g} = F_{lab}\left(1+\frac{16}{100}\right)^{\log\frac{v_{u/g}}{v_{lab}}} \tag{6.2}$$

Cementitious Packs:

(Smit et al., 1998)

$$F_{u/g} = F_{lab}\left(1+\frac{10{,}4}{100}\right)^{\log\frac{v_{u/g}}{v_{lab}}} \tag{6.3}$$

where $F_{u/g}$ is an adjusted force

F_{lab} is an original force as measured during laboratory testing

$v_{u/g}$ is an underground site velocity/closure rate (typically 1 – 3 m/s for rockbursts and 1 – 30 mm/day for rockfalls)

v_{lab} is a laboratory compression rate (typically 10 – 30 mm/min)

m is an empirically determined correction factor; m = 0.123 for rockbursts and m = 0.084 for rockfalls.

The above equations can be rewritten as $F_{u/g} = \boldsymbol{k}\ F_{lab}$, where $\boldsymbol{k}$ is the force-correction factor. A graphical representation of the force-correction factors for different velocities can be found in Figure 6.2 for timber elongates and for timber and cementations packs.

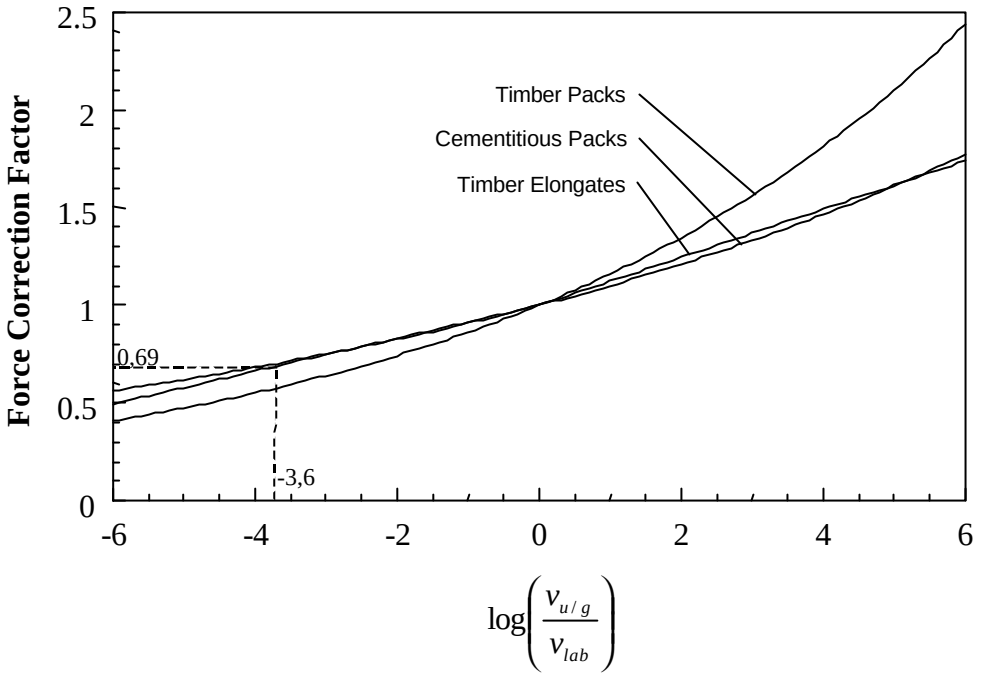

Figure 6.2 Graphs used for adjusting the load-deformation curves for different deformation rates

6.1.2 The effect of dynamic loading on elongates

In order to quantify and evaluate the dynamic performance of support units, the CSIR Mining Technology Support Testing Laboratory conducted routine dynamic compression tests. A testing procedure was developed to provide information on the variability of different support units. The testing procedure consisted of twenty-four tests:

- 10 quasi-static laboratory tests at 15 mm/min;
- 5 dynamic laboratory compression tests at 3 m/s (the units are initially compressed slowly for 50 mm, than subjected to 3.0 m/s for at least 200 mm, and then the test is completed at a slow rate until failure occurs.
- 1 test at a deformation rate of 150 mm/min;
- 1 test at 15 mm/min on a 10°-inclined platen;
- 1 test at 15 mm/min on a 20 mm-stepped platen;
- 1 test at 15 mm/min on a 50 mm stepped platen;

- 1 slow test at a deformation rate of 10 mm/day;
- 1 creep test for seven days; and
- 3 instrumented underground tests.

The results of these tests were then subjected to statistical analysis to provide performance curves for support system design. In addition, and as part of the SIMRAC project GAP 330 (Daehnke et al., 1998) the quasi-static and dynamic performance characteristics of the twelve most widely used elongate types by the gold and platinum industry were evaluated according to the testing procedure described in GAP 330. Some details are given in Table 6.1.

Table 6.1 Details of support types tested as part of SIMRAC project GAP330 (Daehnke et al., 1998)

Elongate Type	Supplier	Nominal Diameter (mm)	Lengths Tested
Cone Prop	MM & E	190	1.0 m; 1.6 m
Disc Prop	Westeel Engineering	170	1.0 m; 1.6 m
Eben Haeser	Jan Woller Mining	200	1.0 m; 1.6 m
Eben Haeser MK 1	Jan Woller Mining	200	1.0 m; 1.6 m
Hard Gum Mine Pole	Generic	150	1.6 m
Load Stick	BMS Mining Supplies	160	1.0 m; 1.6 m
Loadmaster	BMS Mining Supplies	180	1.0 m; 1.6 m
Turned Pencil	Generic	200	1.0 m
Unturned Pencil, pre-stress	Generic	180	1.0 m; 1.6 m
Profile Prop	Mondi Timber	200	1.0 m
Rocprop	Mine Support Products	150	1.0 m; 1.6 m
Timber Splitter	Elbroc Strata Control	180	1.0 m; 1.6 m

Test results (laboratory and underground) were sorted according to elongate type and length. Summary statistical evaluations were conducted on the slow and rapid test results and are

presented below. Figures 6.3 (*a, b*), 6.4 (*a, b*) and 6.5 (*a, b*) of the statistical evaluations show the mean values and measures of the variability of the limited number of units tested. These variability curves represent various lower confidence limits of the elongate performance. The mean –1 standard deviation (or approximately 84% lower limit), 90% and 95% limits are shown to illustrate the effects of increasing the confidence of exceeding the design curve. Comparing the rate effects appears to indicate that little variation in performance exists between 15 and 150 mm/min, bearing in mind that only one test was conducted at 150 mm/min.

As a whole, there does appear to be enough information across all elongate types and at both lengths to imply that there is little difference between results from testing rates at 15 and 150 mm/min, and certainly not when considering the variability obtained from ten slow tests. For this reason, a standard testing rate of 30 mm/min would be more practical, especially since many of the manufacturers/suppliers in the past have used this rate and their database is largely based on this test rate.

Since estimates had to be made with regard to the accuracy of the load cells, the use of the underground test results is somewhat subjective, especially following the large seismic events that both the short and long elongates were subjected to. Photographs of the installed units had to be reviewed in considerable detail to determine the validity of *In-situ* results. The underground results shown in the following graphs have been formatted such that reliable results are shown with a dotted line and unreliable or false results are shown with a dashed line. From the graphs, the average performance of the supports was determined from the reliable results.

As an example of fast and slow test results, consider the Rocprop force versus the deformation curves given in Figure 6.3 (*a, b*).

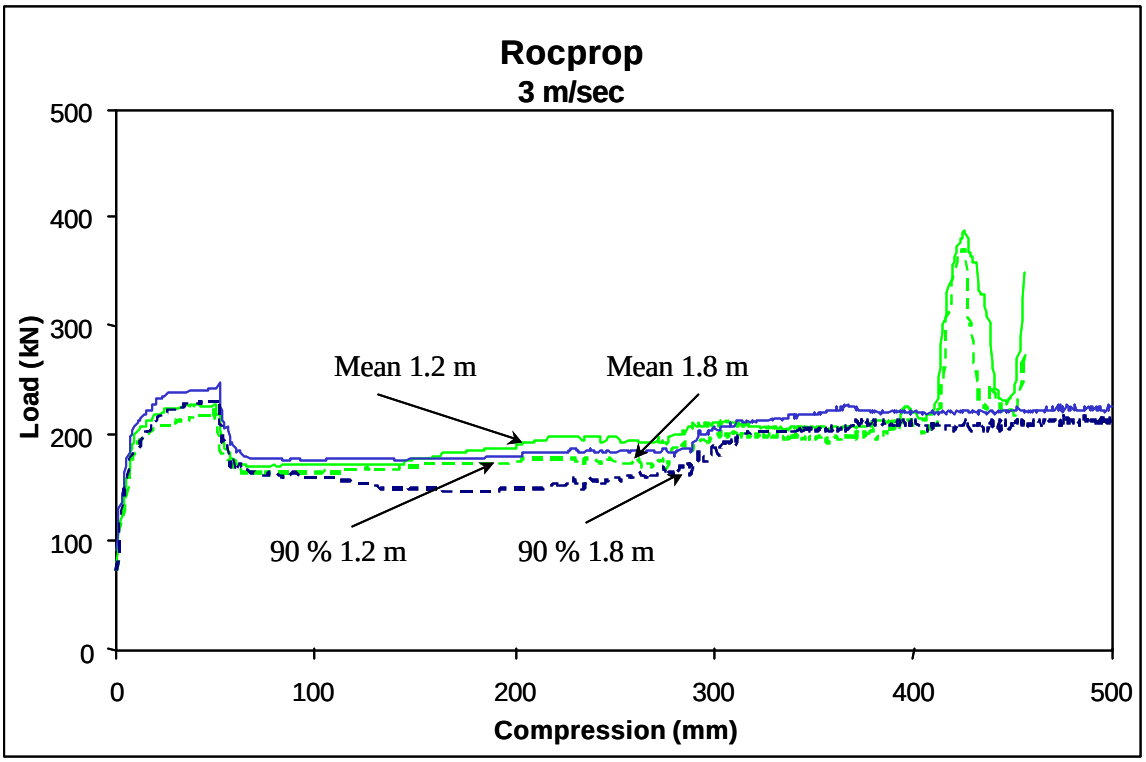

(*a*)

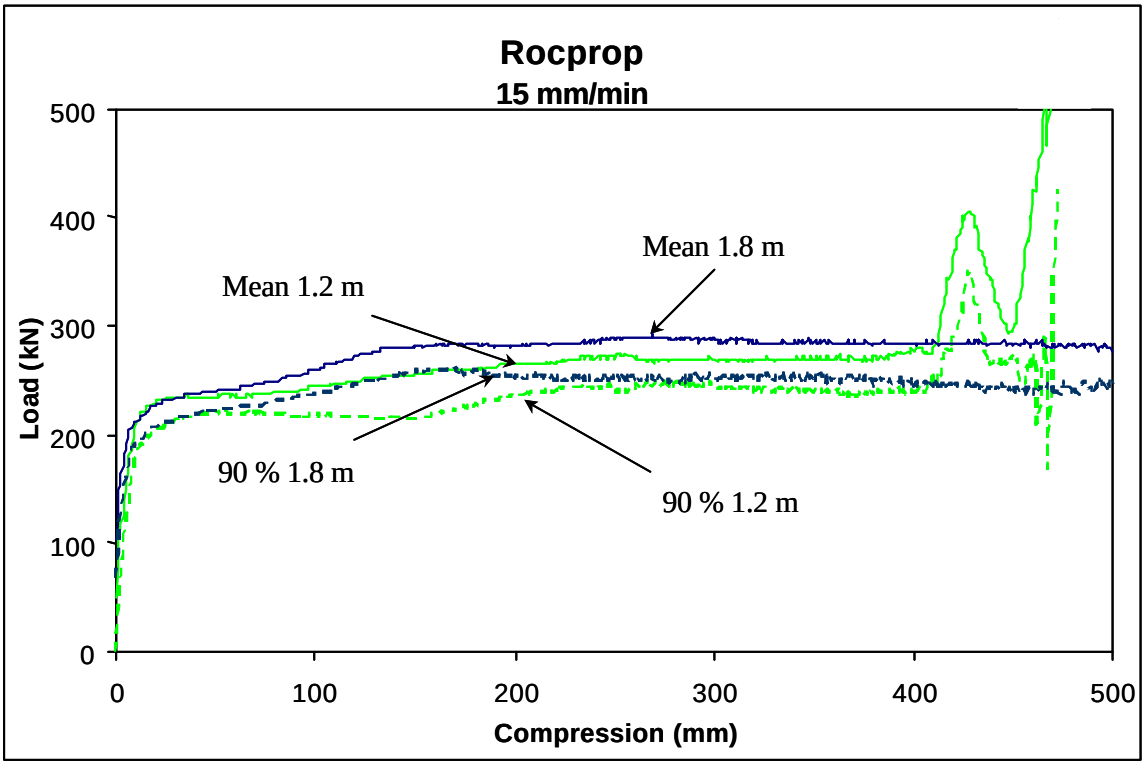

(*b*)

Figure 6.3 (a, b) Results of statistical analysis on Rocprop performance data: (a) 3 m/s; (b) 15 mm/min

As an example of fast and slow test results, consider the Profile Prop force versus the deformation curves given in Figure 6.4 (*a, b*).

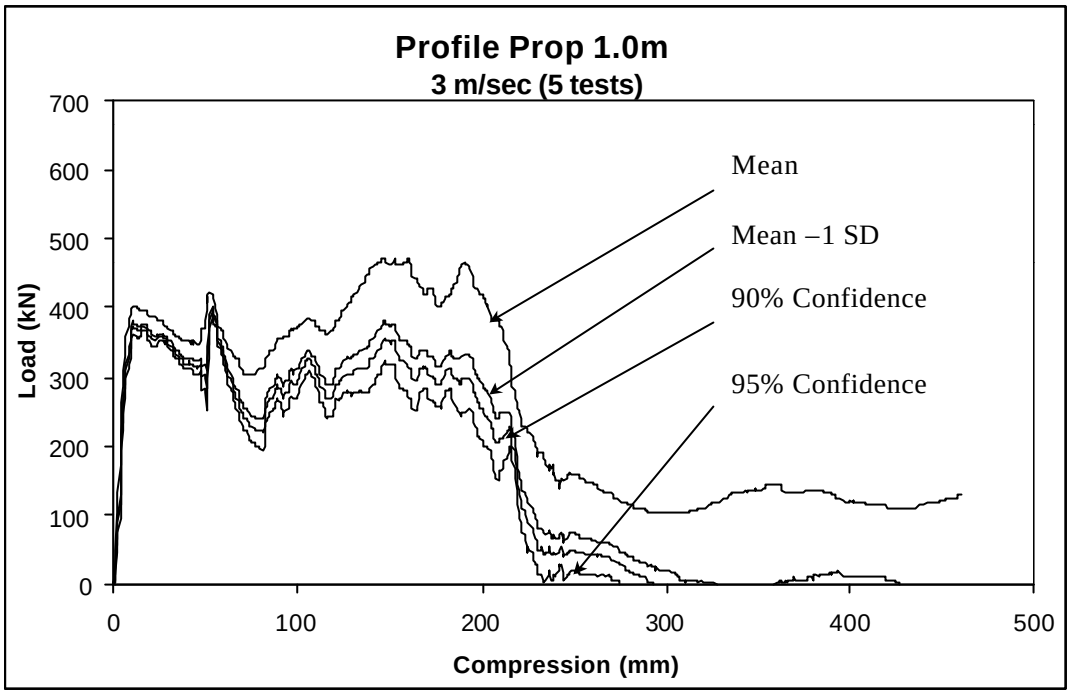

(***a***)

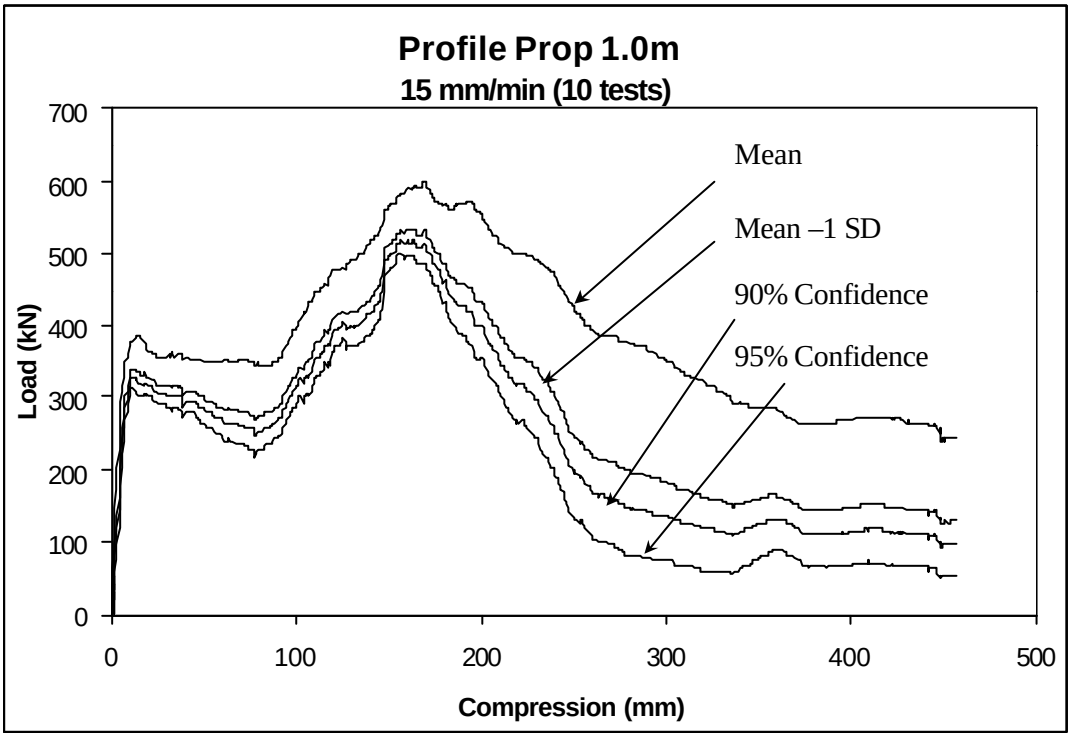

(***b***)

Figure 6.4 (a, b) Results of statistical analysis on Profile Prop performance data: (a) 3 m/s; (b) 15 mm/min

As an example of fast and slow test results, consider the Pencilprop force versus the deformation curves given in Figure 6.5 (*a, b*).

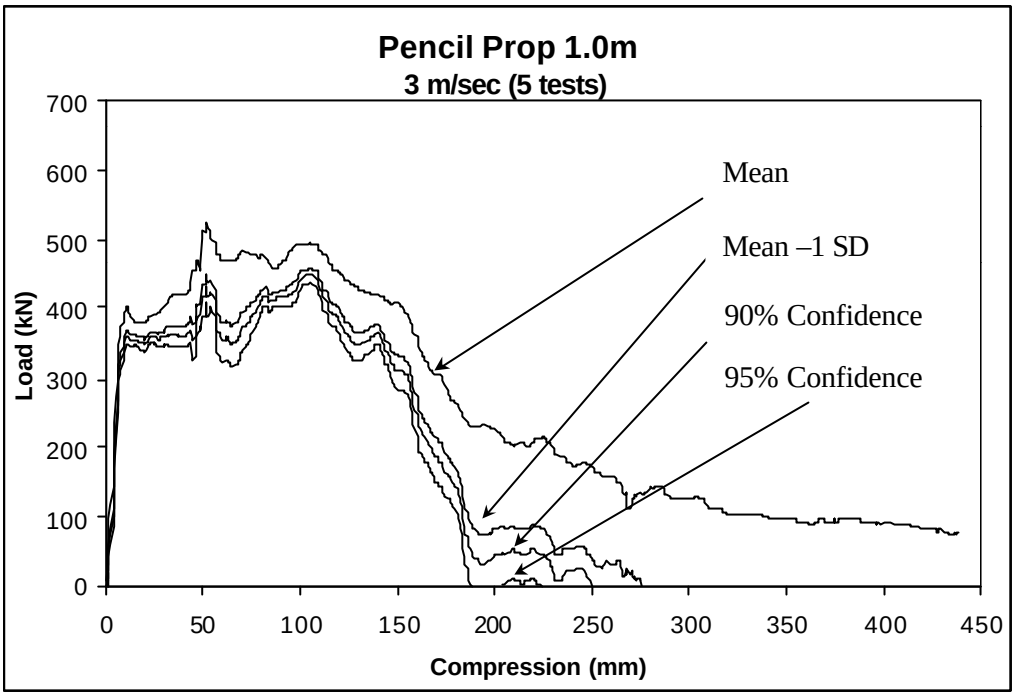

(***a***)

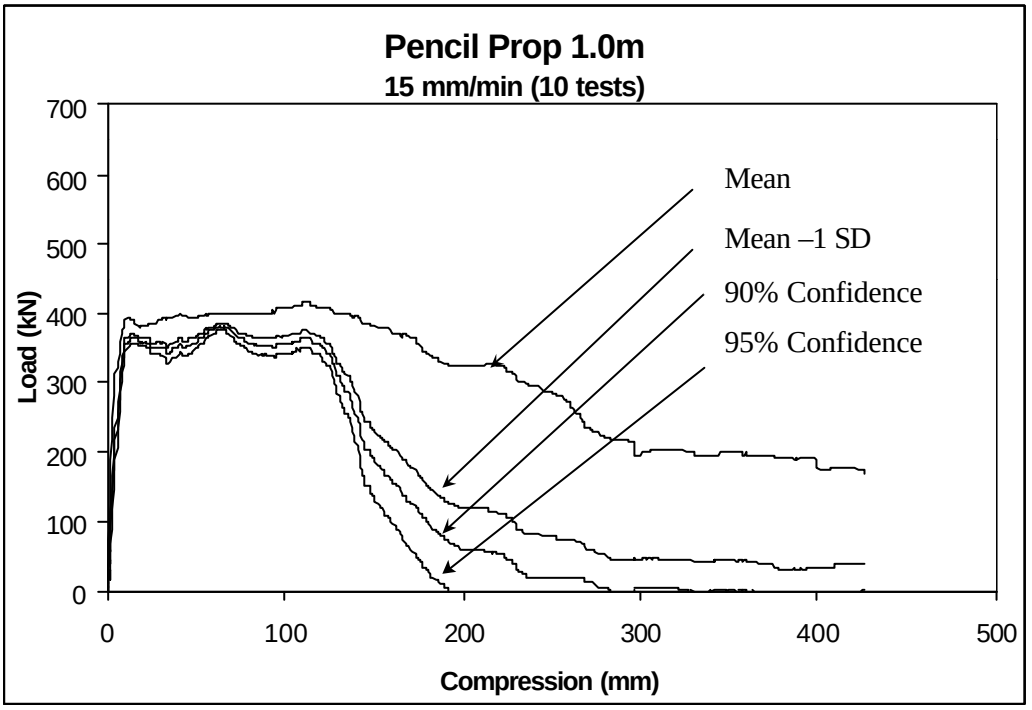

(***b***)

Figure 6.5 (a, b) Results of statistical analysis on Pencilprop performance data: (a) 3 m/s; (b) 15 mm/min

Owing to the variety of materials used and the difference in the construction of each elongate, the variability of performance between different specimens of each type tested is, in itself, a point to be taken into consideration. The Rocprop elongate, for example is a well-engineered steel elongate, which displays a remarkably consistent performance (see Figure 6.3 (*a, b*)).

The Pencilprop is a timber-based unit with a separate pre-stressing device and some machining is done to control the yielding behaviour. Being a basic prop, with timber as its main constituent, it exhibits a greater degree of variability in its performance, as seen in Figure 6.5 (*a, b*). A statistical analysis was carried out in order to take the variability of elongates performance into consideration.

Friction-based yield units (e.g. Rocprop) typically exhibit lower loads as the rate of compression testing increases; this is clearly seen in Figure 6.6. This negative rate dependency is reversed when timber is combined with an engineering yielding unit, as can be seen in Figure 6.7, where the rapid tests provide higher yield loads.

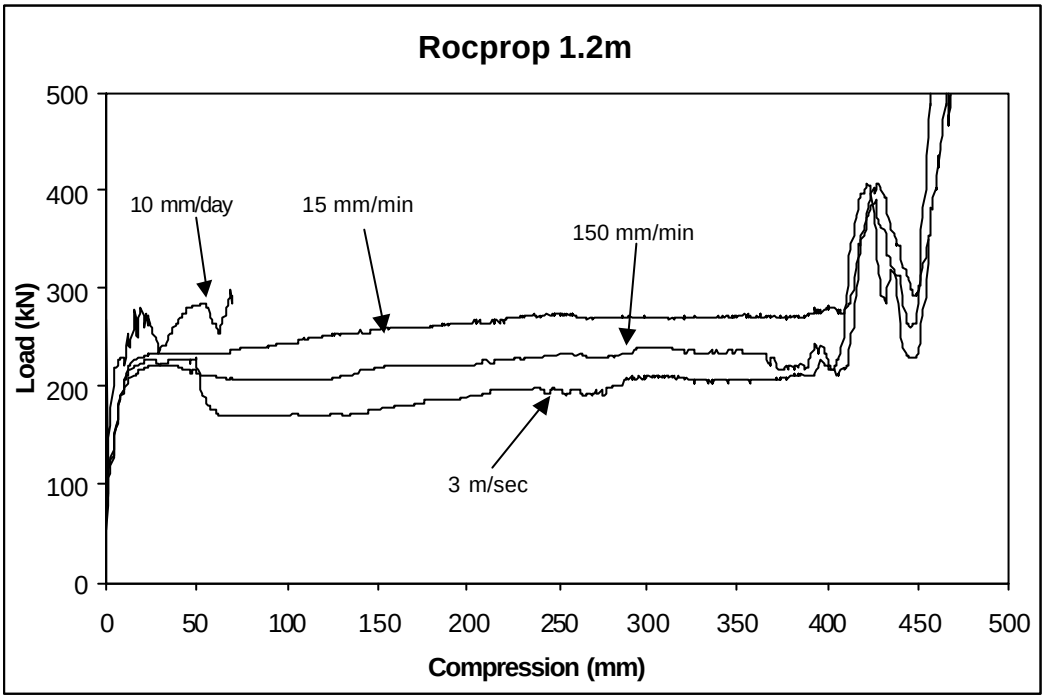

Figure 6.6 Rate-dependent performance of a Rocprop comparing average performance curves at different testing rates

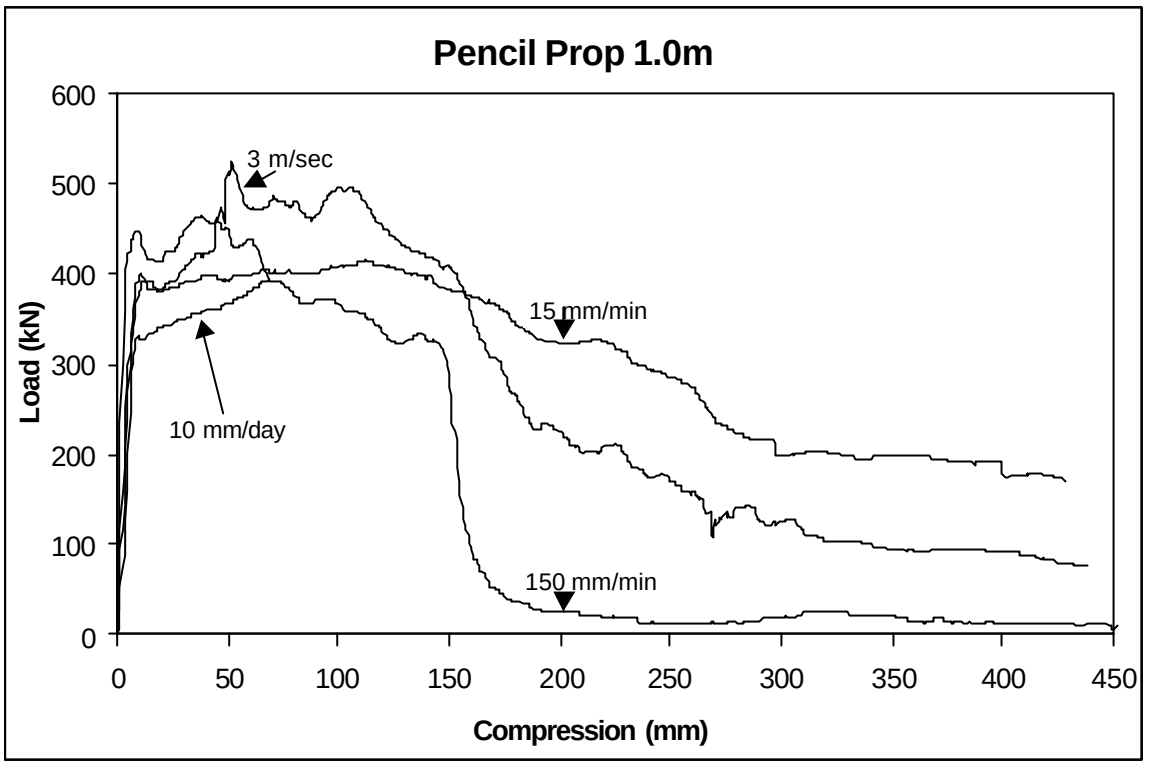

Figure 6.7 Rate-dependent performance of a Pre-stressed Pencilprop comparing average performance curves at different loading rates

6.1.3 The effect of dynamic loading on roofbolts

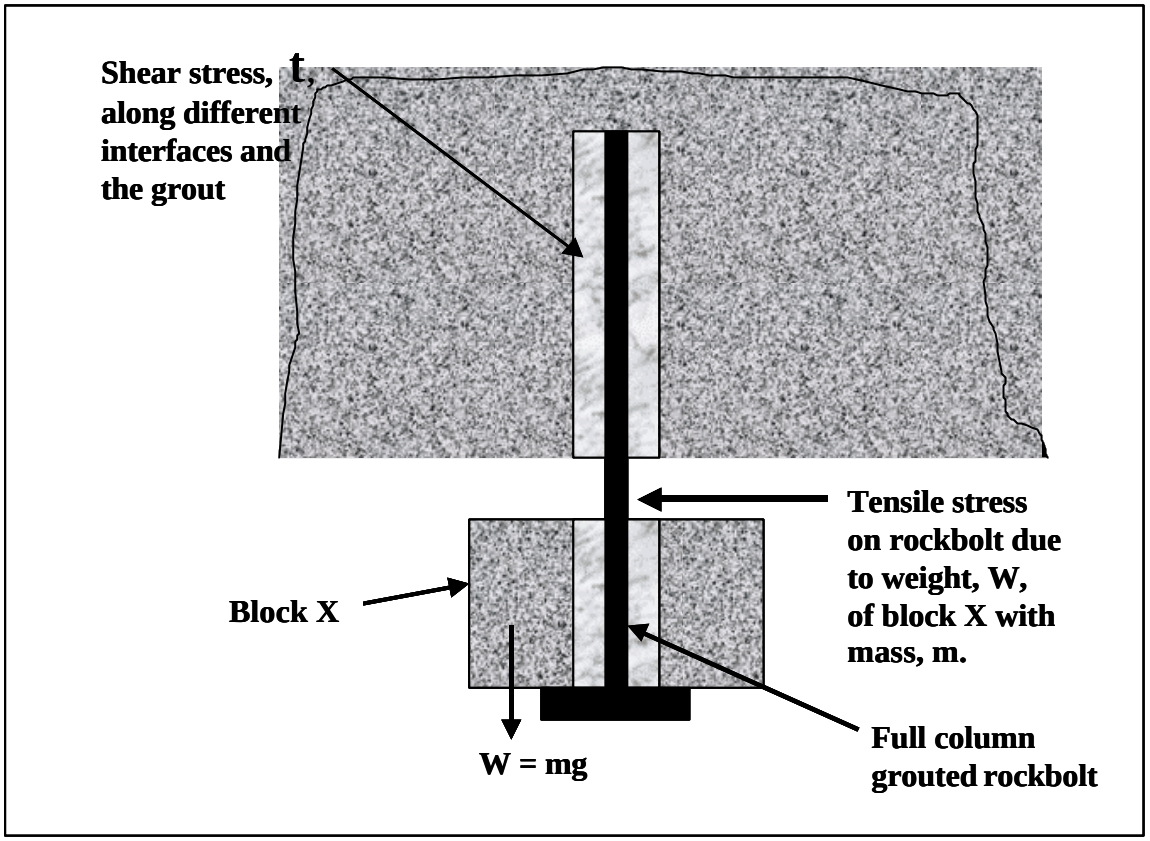

Figure 6.8 Deadweight loading causing a tensile stress in the roofbolt

Assume that a seismic wave causes movement in the vertical direction in Figure 6.8. If this wave imposes a downward velocity to the block that is being supported, the total downward force F_d will increase. This is a function of the mass, *m*, of the block and the change in acceleration, *a*, of the block. This is given by:

$$F_d = ma \tag{6.4}$$

$$F_d = m(g + \frac{\partial v}{\partial t}) \tag{6.5}$$

$$F_d = mg + m\frac{\partial v}{\partial t} \tag{6.6}$$

where *v* is the velocity experienced by the block due to the seismic wave and *t* is the time period in which the block is excited by the wave.

Equation (6.6) give an asymptotic solution for frequencies much grater then the resonance frequency. A more complete description of the tendon-mass behaviour is given by:

$$F_d = mg + m\frac{\partial v}{\partial t} + bv + ku \tag{6.7}$$

where v is the velocity experienced by the block due to the seismic wave and t is the time period in which the block is excited by the wave,

k is the stiffness of tendon at current load,

u is relative displacement, and

b is “viscous” frictional loss.

The load-deformation curves of the different tendons can be used to calculate the energy-absorption capabilities of the different tendons by calculating the area under the graph. The total energy of a block in the hangingwall of a stope is a combination of the kinetic and potential energy. The kinetic energy is zero if the velocity of the block is zero. Thus, the energy-absorption capability E_f of a tendon is given by:

$$E_f = m\left(\frac{1}{2}v^2 + gh\right) \tag{6.8}$$

where h is the maximum downward deformation of a tendon, m is the mass of the block that the tendon is supporting, g is the gravitational acceleration and v is the velocity of the block induced by dynamic loading.

Thus, m can be expressed as:

$$m = \frac{E_f}{\frac{1}{2}v^2 + gh} \tag{6.9}$$

The mass of the block in the hangingwall is a function of its volume, V, and the density, ρ, of the rock:

$$m = \rho\ V \tag{6.10}$$

and,

$$V = b\ A \tag{6.11}$$

where b is the bedding plane height and A is the tributary area supported by each tendon.

Therefore,

$$m = \rho\ b\ A \tag{6.12}$$

Thus,

$$A = \frac{m}{\rho b} \tag{6.13}$$

Equation (6.13) can be used to determine the spacing of the support units as a function of the mass of the blocks in the hangingwall, the density of the rock and the bedding plane thickness. The maximum mass of the block in the hangingwall that a tendon can support can be determined from equation (6.9).

The energy-absorption capability E_f and the maximum downward deformation *h* of the tendon can be determined from the load – deformation curves (Figure 6.9 (*a, b, c,* and d)), and the velocities can be measured by geophones.

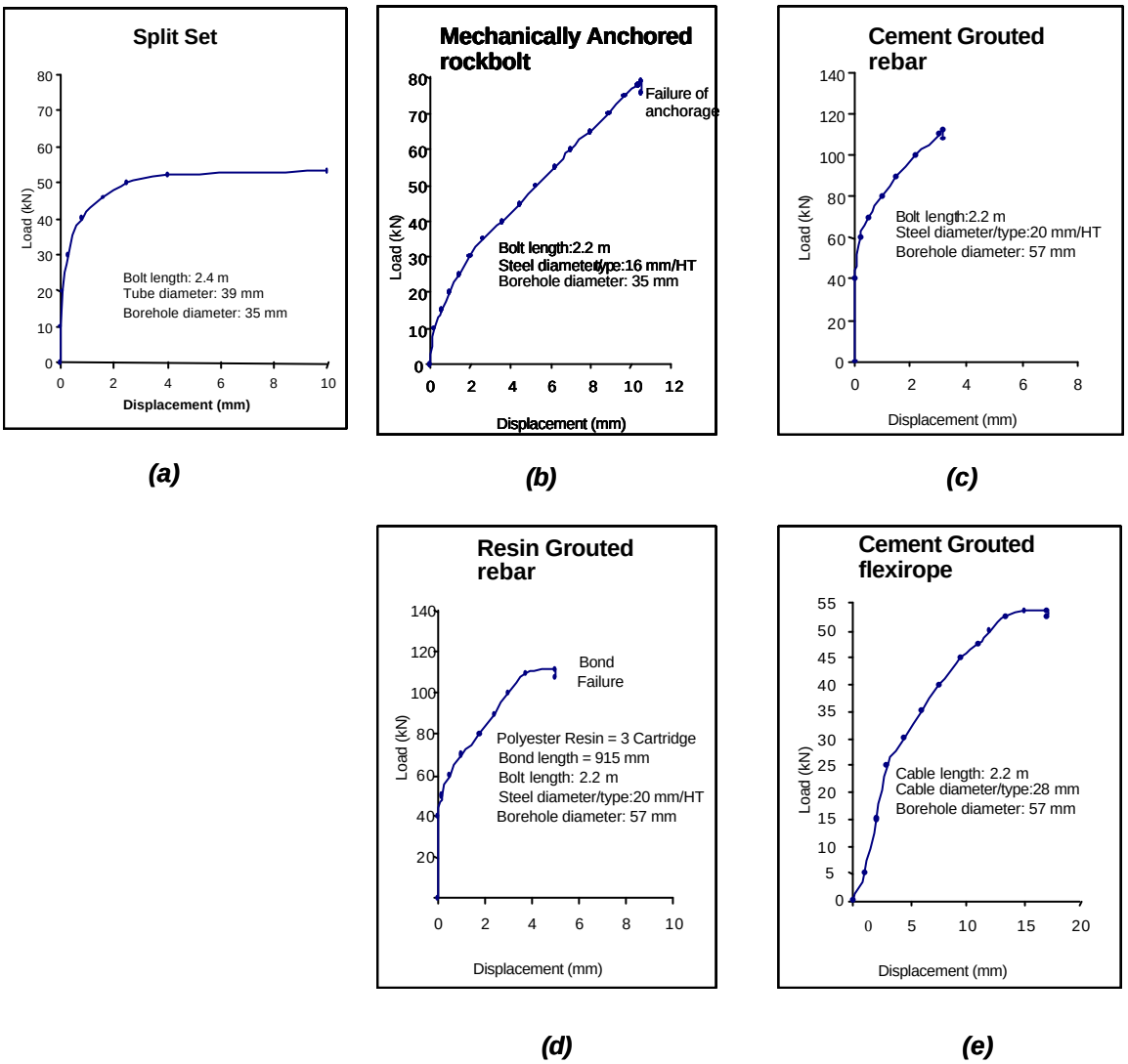

Figure 6.9 (a, b, c, and d) Load-deformation curves for: (a) split sets; (b) mechanically anchored rockbolt; (c) cement grouted rebar; (d) resin grouted rebar, and (e) cement grouted Flexirope (after Stillborg, 1986)

From equation (6.9) and (6.13), both the mass of the block that the tendon is supporting at a velocity induced by dynamic loading and the spacing of the support units as a function of the

mass of the blocks in the hangingwall can be derived. The graphs shown in Figures 6.11, 6.12 and 6.13 are than drawn using these values with an induced velocity of 3 m/s, 2 m/s and 1 m/s. respectively.

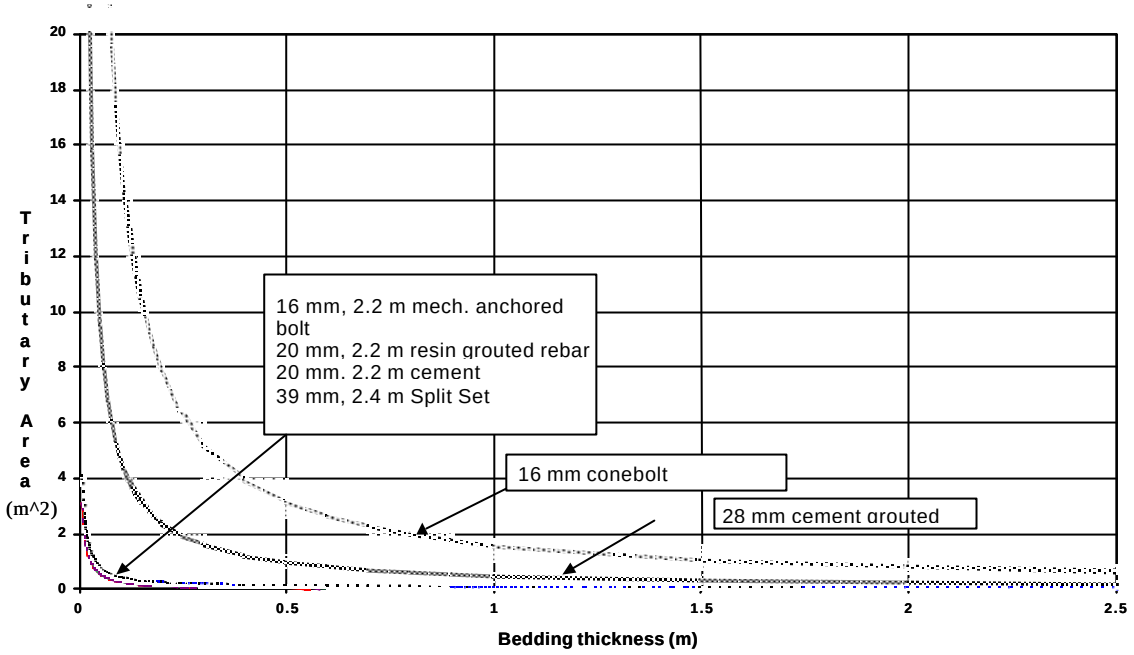

Figure 6.10 Maximum allowable support spacing for a block experiencing a velocity of 3 m/s. The support spacing is a function of the bedding thickness and energy-absorption capabilities of the tendons

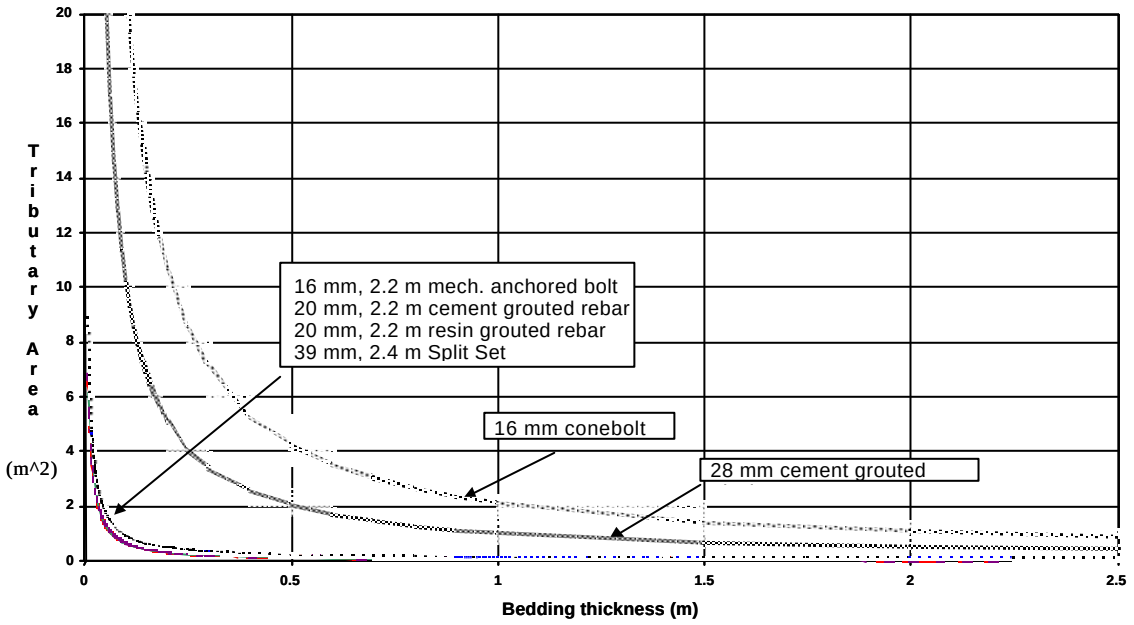

Figure 6.11 Maximum allowable support spacing for a block experiencing a velocity of 2 m/s. The support spacing is a function of the bedding thickness and energy-absorption capabilities of the tendons

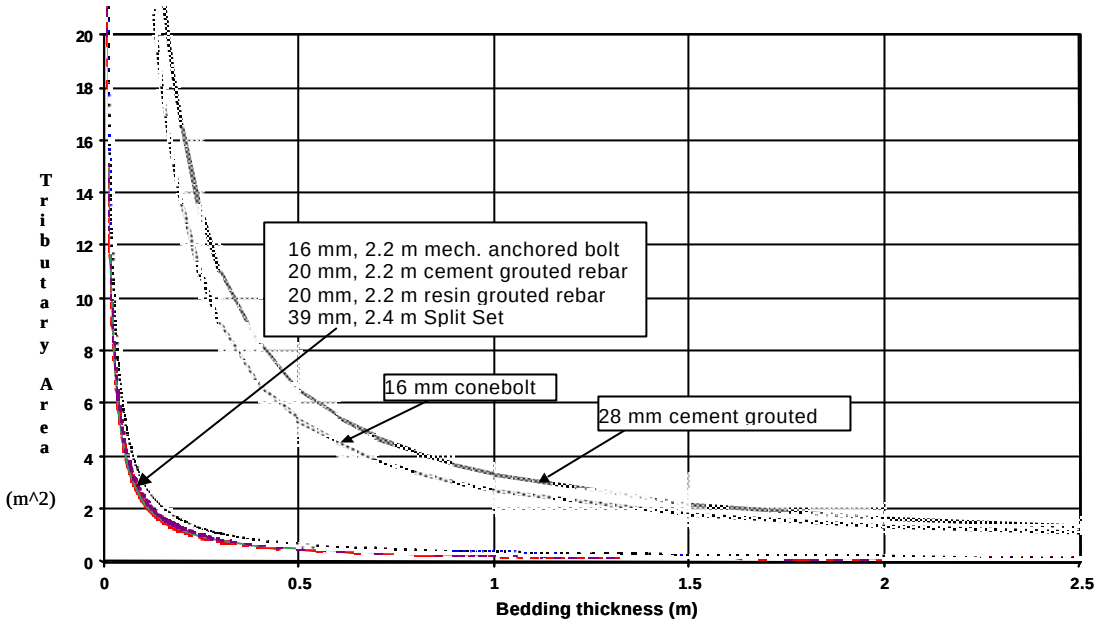

Figure 6.12 Maximum allowable support spacing for a block experiencing a velocity of 1 m/s. The support spacing is a function of the bedding thickness and energy-absorption capabilities of the tendons

At 3 m/s velocity (Figure 6.10), the Conebolt has the highest energy-absorption capability, followed by that of the Flexirope, and both tendons will therefore be suitable for use under dynamic conditions due to their high energy-absorption capacity. They are therefore suitable to use as rockburst-resistant support. The other tendons tested have similar, and comparatively low, energy-absorption capabilities, making their use under dynamic conditions and as rockburst-resistant support unsuitable.

6.2 Hangingwall stability during the interaction with Rayleigh waves

This section is based on M. van Zyl's M.Sc. project. The thesis was developed in the course of this project. Some editorial changes, simplifications as well as some important corrections were made. A major extension involving underground measurements was also carried out.

The tributary area energy-absorption criterion assumes a continuous hangingwall slab. It is known, however, that the hangingwall combines discrete fractures and joints. It is therefore necessary to take the effects of these discontinuities on the stability of the hangingwall into account when rockbursts occur.

The energy-absorption criterion would be adequate, however, when waves interact with the mining excavations: the fractures and joints will affect the reflection and refraction of body and surface waves. An alternative rockburst model, which investigates the interaction between Rayleigh waves and mining excavations, and which takes the discontinuous nature of the hangingwall into account, was developed. The model focuses on the stress changes caused by the passage of Rayleigh waves along a stope. The importance of maintaining horizontal clamping stresses is also emphasised by this rockburst model.

6.2.1 Introduction

When a portion of an elastic body is deformed by a transient elastodynamic disturbance, some time elapses before the remainder of the body is affected by the deformation. The velocity of the advance of the disturbance is controlled by the inertial and elastic properties of the body. In the bulk of an elastic, homogeneous body, only two fundamental type of waves propagate:

- compressional P-waves (P for primary), where the particle motion is along direction of propagation, and

- shear S-waves (S for secondary), where the particle motions are perpendicular to direction of propagation.

Both P- and S-waves, are also known as body waves as they propagate through the interior of the medium.

Only P- and S-waves can propagate in an unbounded elastic medium. Where boundaries exist as in the half-space problem, a third type of wave exists, the effects of which are confined close to the surface. Lord Rayleigh (1887) first discovered and investigated these so-called surface waves.

The particle motion (SV type) of the Rayleigh wave at the free surface is elliptical in motion and retrograde with respect to the direction of motion. The amplitude of the displacement in the direction of propagation decreases with increasing distance from surface and the rate of attenuation is dependent on the frequency of the wave. The waves propagate in a homogeneous half-space without dispersion.

Surface waves of the SH type are observed to occur in the Earth's surface. Love waves (named after A.E.H. Love, 1911) travel by a transverse motion of particles that is parallel to the ground surface. The particle motion is traverse and horizontal with velocities greater than Rayleigh waves. Love waves arise when it is assumed that a surface parallel layer of different density and elastic properties exists

As Rayleigh waves are the principal cause of major damage to structures on the surface during earthquakes, it is anticipated that they also play a major role in destabilising the hangingwall during seismic events. It is therefore important, from a mining point of view, to understand whether keyblocks may be ejected during the passage of a Rayleigh wave.

Most mine seismic studies focus on parts of the seismograms that are normally identified as P-waves or S-waves, for several reasons, for example:

- P-wave and often S-wave arrivals are easy to identify and are used to obtain source hypocentral locations.

- Geophones in mine seismic networks are placed in sites remote from stopes which are the most obvious source of surface waves.

- Surface waves of natural earthquakes are associated with the earth's surface and they dominate the seismograms at large distances.

- Well-developed dispersion due to the strong velocity gradient in the earth results in Rayleigh waves being visible for many cycles of motion.

Rayleigh waves are produced when S-waves are incident on a free surface at an angle of more than about 35^0 from the normal. This is illustrated in Figure 6.13 which shows the reflected amplitude of P- and S-waves at a free surface.

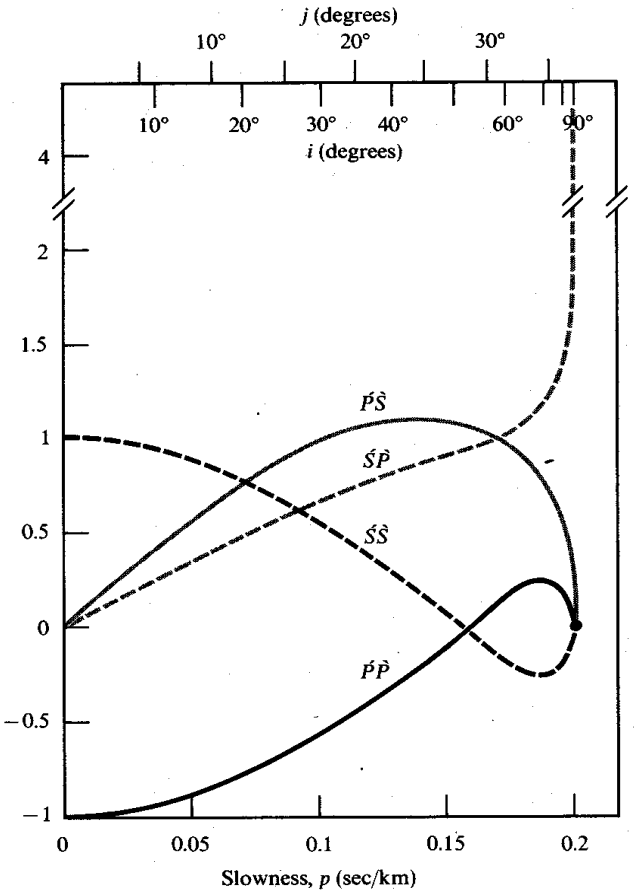

Figure 6.13 Reflected amplitude from P- and S-waves incident at a free surface, for Poisson solid (n = 0.25). The first character (P- or S-wave accented) denotes the incoming wave and the second character (P- or S-wave accented) denotes the amplitude of the reflected wave. From Aki and Richards (1980), p 142.

Some important features that can be read from this figure are:

- Normal incidence results in doubling of ground motion.
- P-wave incidence of $j = 40^0$ results in considerable amplitude of reflected S-waves.
- There is no real solution for reflected amplitudes of S-waves at incidence angle of $j \geq 37^0$

Strong ground motion from mining-induced events (say $V_{MAX} \geq 100$ mm/s) occurs in the near field of each event. Mine seismic systems report the hypocentral location and some indication of size (e.g. Brune radius) for each event. The systems do not give any details of the spatial (or temporal) spread of the (assumed) shear slip that constitutes the source. It is therefore impossible in practice to predict the history of near-field strong ground motion.

One partial solution to this problem is through generation of synthetic ground motion from modelled sources and mine geometries (Hildyard et al., 2001) and this work does provide some useful insights into likely ground motions, including the possibility that Rayleigh waves dominate at fairly close distances.

Even if the full history of shear slip at the source is know, ground motions in the stope are strongly affected by in homogeneity and inelastic behaviour of the fractured ground around the stopes. This takes place in at least two different ways:

- A shear source in the solid ahead of the face does not daylight into workings. This results in the situation that there are volumes of rock that, in principle, will be subject to increasing stress. It is believed that this, on occasion, has the unfortunate effect of compressing the fractured ground ahead of the face so severely that it responds by moving rapidly into the face area of the stope itself.

- Through "site" effects caused by the induced fracturing around any point of the hangingwall or footwall of the stope (Milev, et al., 1999).

Rayleigh waves measured in a mine stope are shown in Figure 6.14.

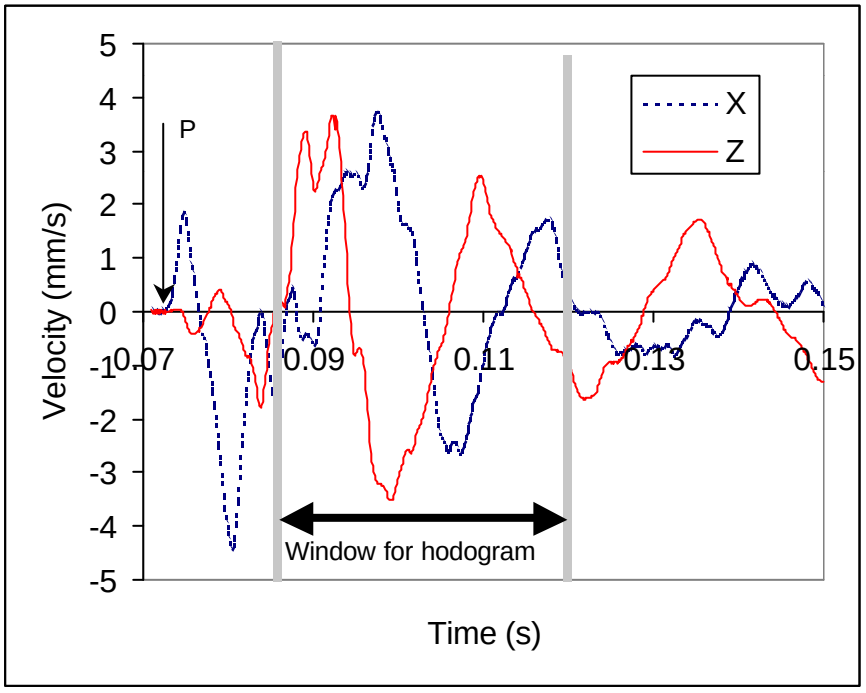

Figure 6.14 Portion of an unfiltered seismogram recorded underground

The following features can be noted from Figure 6.14: (i) the horizontal X component shows the largest initial, P-wave, motion; (ii) the linear polarisation of the early part of the seismograms that is normally seen in recordings from geophones placed in solid rock away from mine

excavations is absent (this is very common for in-stope recordings); (iii) the marked time window shows that the X component lags 90^0 behind the Z component.

The polarisation diagram for these seismograms in the SV plane is shown in Figure 6.15.

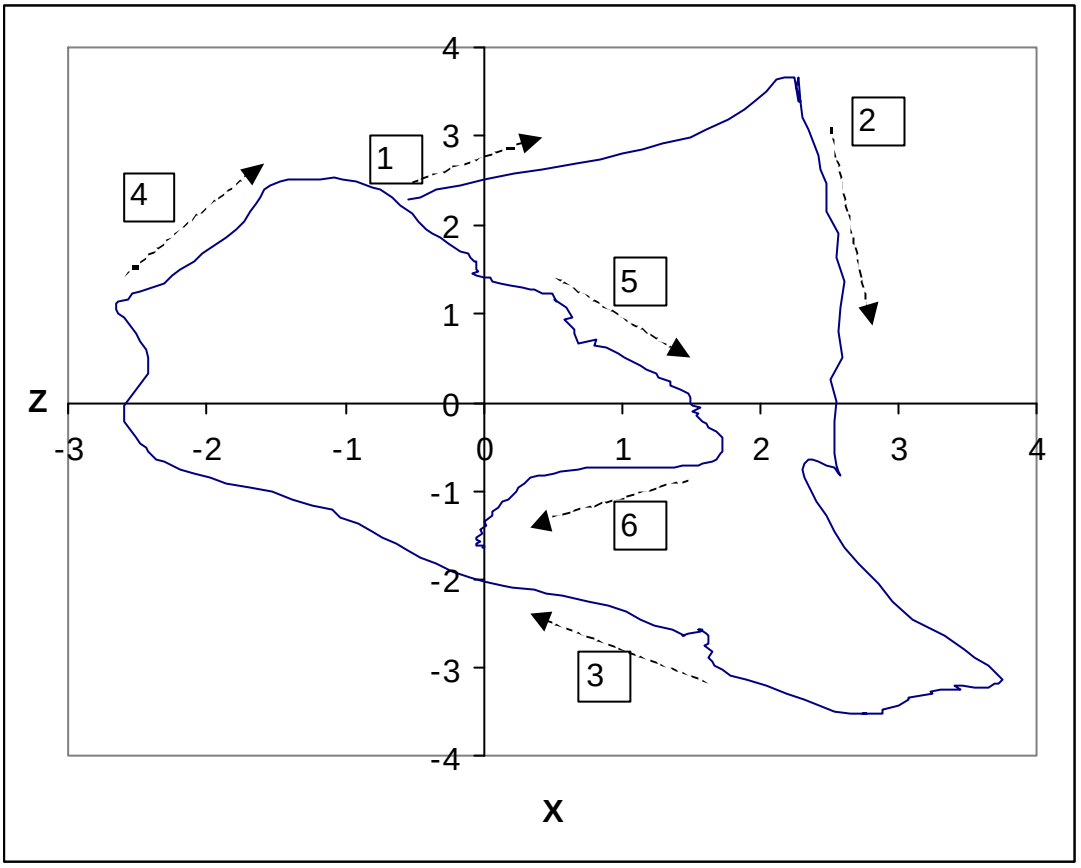

Figure 6.15 Particle motion plot in the SV plane (in this case SV is the plane normal to the surface of the excavations). The arrows numbered from 1 to 6 indicated the direction of particle motion

The identification and use of Rayleigh waves in the seismic data recorded underground is a new area in the filed of mining seismology. However, the consideration of the this type of waves in understanding the rockmass behaviour and the relevant support strategies could play an important role as they are very often associated with the strongest ground motion.

6.2.2 Rayleigh waves

In many texts, Rayleigh waves are shown to be a consequence of an assumed plane wave solution to the equations of motion such that the stress-free boundary condition is satisfied. The interaction of P- and SV-waves with the free surface gives rise to an interference Rayleigh wave that effectively travels along the surface.

At a free surface ($x_3 = 0$), the tractions disappear, thus, $\sigma_{33} = \sigma_{13} = \sigma_{23} = 0$. In the plane co-ordinate system used here, the plane waves are confined to the x_1 x_3 plane ($u_2 = 0$, $\frac{\partial u_i}{\partial x_2} = 0$). The subscript *I* refers to an incident wave, while the subscript *R* indicates that a wave is reflected.

The wave speeds are related to the angle of incidence and reflection by Snell's law:

$$\frac{\sin i_1}{c_p} = \frac{\sin i_2}{c_s} \tag{6.14}$$

Since $C_P > C_S$, a critical angle of incidence, $j_c = \sin^{-1}\left(\frac{c_s}{c_p}\right)$, exists, such that the reflected *P* wave travels along the free surface (i.e. $i_2 = \frac{p}{2}$), $j_c = 35°$ for a Poisson solid with v = 0.25

A plane P-wave can propagate along a boundary, an evanescent P-wave cannot. The same applies to a horizontally propagating SV-wave. The surface stress condition precludes the existence of purely SV- and P- evanescent waves on the boundary. Simultaneous, coupled evanescent P- and SV-waves do satisfy the surface boundary condition, yielding a new form of wave solution, the Rayleigh wave.

The potentials for the P- and S-waves are represented by ϕ and ψ respectively:

$$f = Ae^{iw\left(px_1 + h_a x_3 - t\right)} = Ae^{-wh_a x_3} e^{iw\left(px_1 - t\right)}, \tag{6.15}$$

$$y = Be^{iw\left(px_1 + h_b x_3 - t\right)} = Be^{-wh_b x_3} e^{iw\left(px_1 - t\right)}, \tag{6.16}$$

where *p* is inversely proportional to the apparent velocity (or Rayleigh wave velocity) C_R, and *A* and *B* are wave amplitudes, and ω is angular frequency,

$$p = \frac{1}{c_R}, \tag{6.17}$$

and

$$h_a = \sqrt{\frac{1}{a^2} - p^2}, \tag{6.18}$$

$$h_b = \sqrt{\frac{1}{b^2} - p^2}. \tag{6.19}$$

Furthermore, $C_R < C_S < C_P$, confines the energy to propagate along the surface with exponential decay of the potentials away from the surface. This decay of the velocities of the waves away from the surface is illustrated and confirmed (by Hildyard, 2001) and can be shown in Figure 6.16.

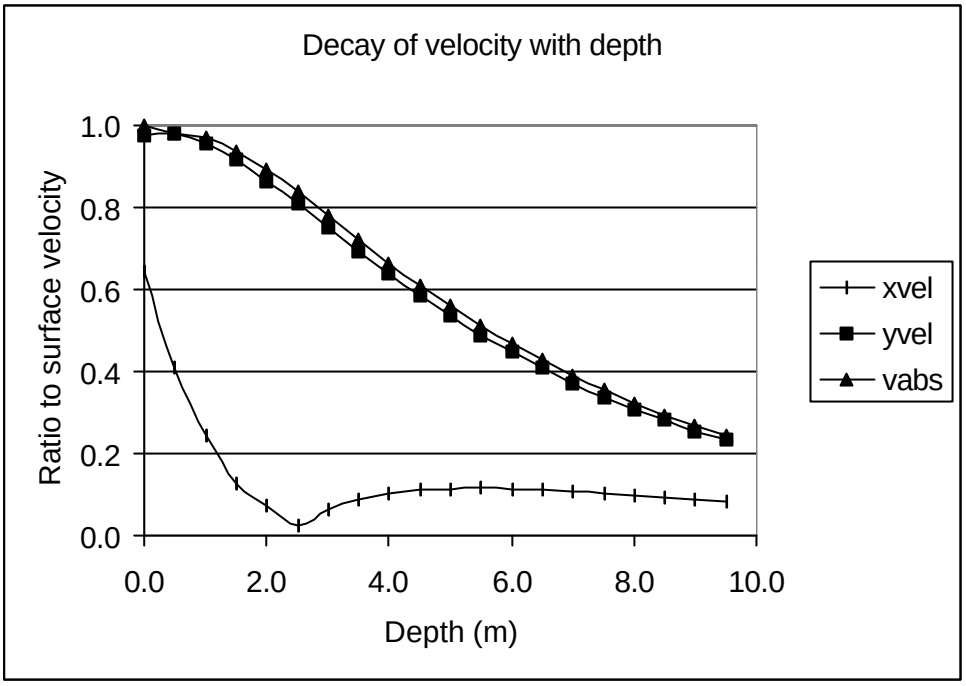

Figure 6.16 Decay of velocity with depth into the hangingwall (Hildyard, 2001): xvel is velocity in horizontal direction (parallel to the hangingwall); yvel is velocity in vertical direction (normal to the hangingwall); vabs is defined as: $vab = \sqrt{xvel^2 + yvel^2}$

The surface wave motion involves a mixture of P- and S-wave motion, with relative amplitudes *A* and *B*, respectively (note that *A* and *B* are the amplitudes of the potentials, and not the amplitude of the stress wave, i.e. displacement, velocity, acceleration, stress etc., and have units of m^2), and

$$B = \frac{-A}{2c_R \boldsymbol{h}_{cs}} \left(\frac{c^2{}_R}{c^2{}_s} - 2 \right) \tag{6.20}$$

to satisfy the surface boundary conditions:

$$\boldsymbol{s}_{33} \mid_{x_3=0} = 0 \text{ and } \boldsymbol{s}_{13} \mid_{x_3=0} = 0. \tag{6.21}$$

The displacements are given as:

$$u_1 = \frac{\partial \boldsymbol{f}}{\partial x_1} - \frac{\partial \boldsymbol{y}}{\partial x_3}, \tag{6.22}$$

$$u_3 = \frac{\partial f}{\partial x_3} + \frac{\partial y}{\partial x_1}. \tag{6.23}$$

If equations (6.22) and (6.23) are substituted into the equations of motion and a solution form similar to (6.15) and (6.16) is assumed, it is possible to derive the relations (6.24) and (6.25).

$$u_1 = -A\omega p \sin[\omega(px_1 - t)]\left(e^{-\omega\hat{\hbar}_{cp}x_3} + \frac{1}{2}\left(\frac{c^2 R}{c^2_s} - 2\right)e^{-\omega\hat{\hbar}_{cs}x_3}\right), \tag{6.24}$$

$$u_3 = -A\omega p \cos[\omega(px_1 - t)]\left(c_R\hat{\hbar}_{cp}e^{-\omega\hat{\hbar}_{cp}x_3} + \frac{1}{2c_R\hat{\hbar}_{cs}}\left(\frac{c^2{}_R}{c^2_s} - 2\right)e^{-\omega\hat{\hbar}_{cs}x_3}\right). \tag{6.25}$$

In the coordinate system used here, the plane waves are confined to the x_1 x_3 plane ($u_2 = 0,\ \frac{\partial u_i}{\partial x_2} = 0$), thus the equation for the horizontal stress associated with the Rayleigh wave can be obtained from Hooke's Law:

$$\sigma_{11} = \lambda\theta + 2\mu\varepsilon_{11}, \text{ or} \tag{6.26}$$

$$\sigma_{11} = \lambda\left(\frac{\partial u_1}{\partial x_1} + \frac{\partial u_3}{\partial x_3}\right) + 2\mu\left(\frac{\partial u_1}{\partial x_1}\right), \tag{6.27}$$

where

$$\frac{\partial u_1}{\partial x_1} = -A\omega^2 p^2 \cos[\omega(px_1 - t)]\left(e^{-\omega\hat{\hbar}_{cp}x_3} + \frac{1}{2}\left(\frac{c^2{}_R}{c^2_s} - 2\right)e^{-\omega\hat{\hbar}_{cs}x_3}\right), \tag{6.28}$$

and

$$\frac{\partial u_3}{\partial x_3} = A\omega^2 p^2 \cos[\omega(px_1 - t)]\left(c_R\omega\hat{\hbar}^2{}_{cp}e^{-\omega\hat{\hbar}_{cp}x_3} + \frac{\omega}{2c_R}\left(\frac{c^2{}_R}{c^2_s} - 2\right)e^{-\omega\hat{\hbar}_{cs}x_3}\right). \tag{6.29}$$

For the Poisson solid (i.e. v = 0.25); $c = 0.919$; $\beta = 0.531\alpha$; and letting $k = \omega p = \frac{\omega}{c}$ be the Rayleigh wave number, equation (6.24) and (6.25) becomes:

$$u_1 = -Ak\sin(kx_1 - \omega t)\times(e^{-0.85kx_3} - 0.58e^{-0.39kx_3}), \tag{6.30}$$

$$u_3 = -Ak\cos(kx_1 - \omega t)\times(0.85e^{-0.85kx_3} - 1.47e^{-0.39kx_3}). \tag{6.31}$$

Equations (6.30) and (6.31) can be used to calculate the displacements at the surface ($x_3 = 0$) for a Poisson solid (v = 0.25), with $\lambda = m$:

$$u_1 = -0.42\,Ak\sin(kx_1 - \omega t) \tag{6.32}$$

$$u_3 = 0.62\,Ak\cos(kx_1 - \omega t)\,. \tag{6.33}$$

6.2.3 Rayleigh wave interaction with mining excavations

The Wagner rockburst criterion is only based on a relatively simple energy criterion. Wave interactions with hangingwall blocks are not taken into account.

As Rayleigh waves are the principal cause of damage to structures on the surface during earthquakes, it is anticipated that they may also play a major role in destabilising the hangingwall during seismic events. It is therefore considered important that the mechanisms of Rayleigh wave interaction with hangingwall blocks be better understood.

In this section, an attempt is made to quantify and understand the mechanisms leading to keyblock ejections during the passage of a Rayleigh wave.

Actual wave traces are used and compared to theoretical wave displacement and stress equations to determine how hangingwall stability is affected by Rayleigh waves, which travel along the stope hangingwall.

Model conditions:

An attempt was made to consider the simplest possible model of an unsupported hangingwall block that would be stable under quasi-static conditions and that would move downwards relative to the surrounding rock during the passage of a seismic wave. Such a block is sketched in Figure 6.17 below.

Assumptions made:

- The analysis is for continuous half-space and possible motions are then inferred from the displacements and stresses.
- The wavelength of a passing seismic wave is assumed to be much larger than the block itself.
- In the plane-strain section there are no displacements out of the plane.

These downward movements are small compared to the height H of the block.

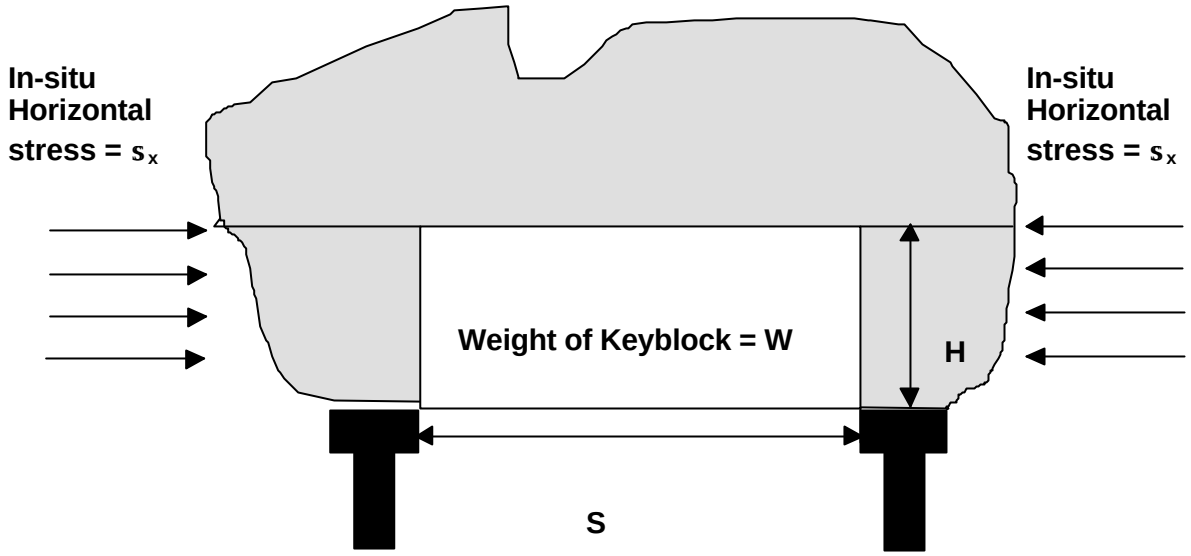

Figure 6.17 Keyblock geometry

A Cartesian co-ordinate system was chosen with x_3 positive to the interior of the solid and the wave travelling towards the x_1 direction in an x_1 - x_3 plane (See Figure 6.20).

In agreement with the classic diagram from Bolt (1978), shown in Figure 6.18, work was done with regard to this topic of vertical acceleration versus horizontal stress by Van Zyl (2001). However, as her results were in conflict with work briefly reported by Spottiswoode (GAP 530) and a graphic simulation by Russel (1999) (Figure 6.16) and Hildyard (2001), it was decided to repeat the analysis.

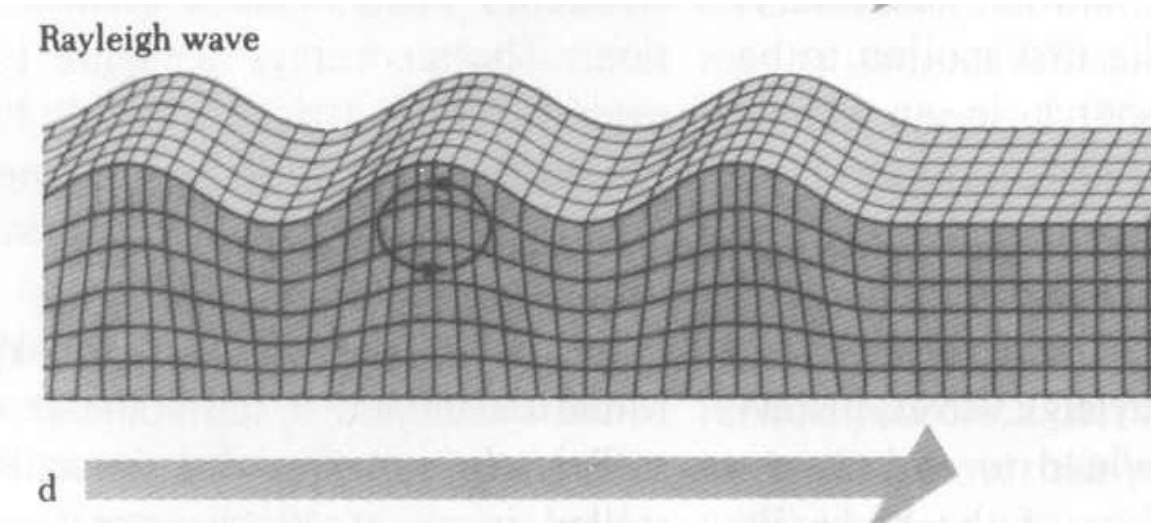

Figure 6.18 Classical picture of Bolt 1978 showing the skin strain and stress are maximum compression at points A and B

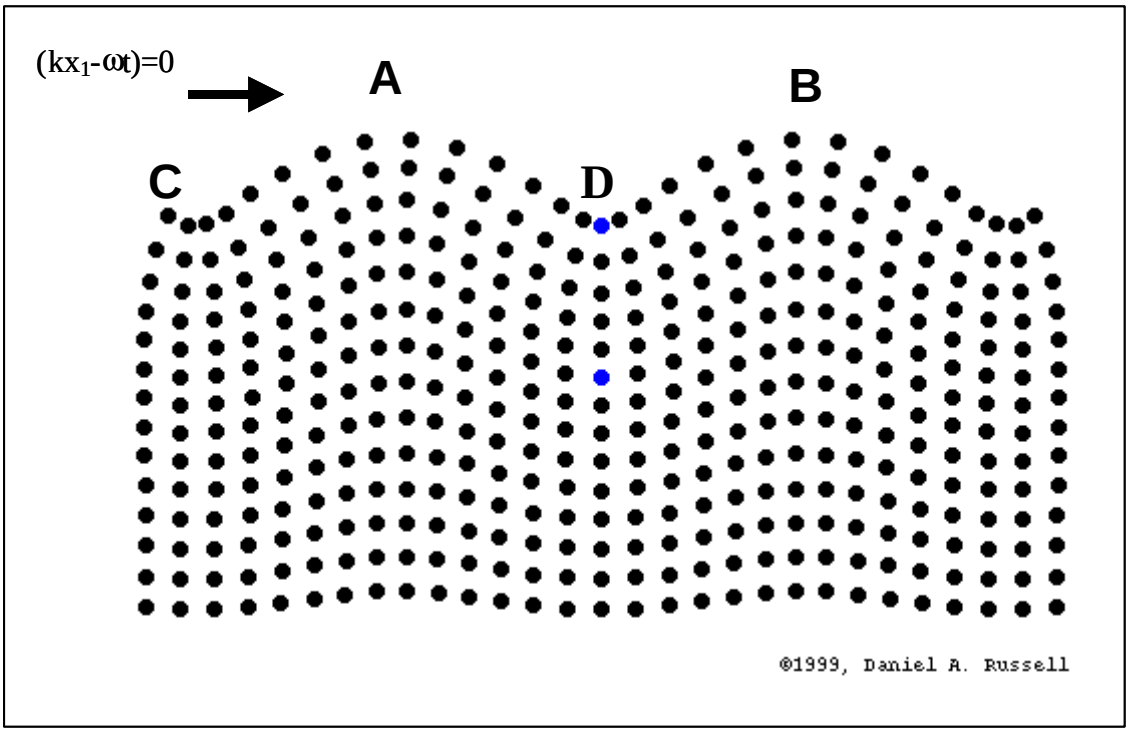

Figure 6.19 Rayleigh wave travelling from left to right along the surface of a solid (Russell, 1999)

From Figure 6.19, note that the skin tensile strain and stress reach their maximum at points A and B, the displacement is also maximally up and, therefore, the acceleration maximally downwards. Moving any block at A or B downwards must be done despite the reduction of confinement caused by the induced tensile strain. This result is in contrast with where the skin stress is at maximum compression at points C and D.

From Figure 6.20, the sign convention is shown and has been used when referring to the hangingwall, to avoid any problems with sign convention with regard to vertical acceleration versus horizontal stress in the hangingwall.

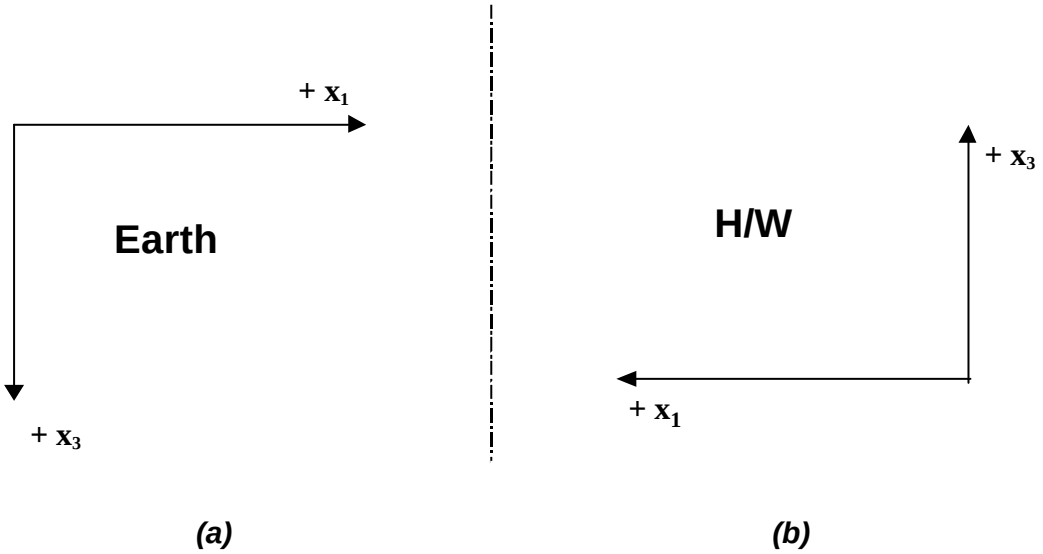

Figure 6.20 Local Cartesian coordinates of the hangingwall and earth surface: $X_3 = 0$ represents the free surface

The velocities, v_1 and v_3 can be obtained by differentiating equations (6.34) and (6.35), respectively with respect to *t*. This gives:

$$v_1 = \frac{\partial u_1}{\partial t} = 0.42Ak\omega\cos(kx_1 - \omega t) \tag{6.34}$$

$$v_3 = \frac{\partial u_3}{\partial t} = 0.62Ak\omega\sin(kx_1 - \omega t) \tag{6.35}$$

The vertical acceleration associated with a Rayleigh wave is found from equation (6.35) to be

$$a_3(t) = \frac{\partial v_3}{\partial t} = -0.62\,Ak\,\omega^2\,\cos(kx_1 - \omega t). \tag{6.36}$$

Note that:

At time $t = x_1 = 0, \quad a_3 = -0.62Ak\omega^2 < 0$ if A > 0

Hooke's Law relating stress and strain can be written as:

$$\sigma_{ij} = \lambda\theta\delta_{ij} + 2\mu\varepsilon_{ij}, \tag{6.37}$$

Where:

$$\theta = \varepsilon_{11} + \varepsilon_{22} + \varepsilon_{33} = \frac{\partial u_1}{\partial x_1} + \frac{\partial u_2}{\partial x_2} + \frac{\partial u_3}{\partial x_3} \quad = \lambda\left(\frac{\partial u_1}{\partial x_1} + \frac{\partial u_2}{\partial x_2} + \frac{\partial u_3}{\partial x_3}\right) + 2\mu\left(\frac{\partial u_1}{\partial x_1}\right)$$

In this model $\frac{\partial u_2}{\partial x_2}$ = 0 and for a Poisson solid λ = μ

Hence, $\sigma_{11} = \lambda\left(3\frac{\partial u_1}{\partial x_1} + \frac{\partial u_3}{\partial x_3}\right)$ (6.38)

From equation (6.29)

$$\frac{\partial u_1}{\partial x_1} = -0.42Ak^2\cos(kx_1 - \omega t) \quad \text{when } x_3 = 0 \tag{6.39}$$

From equation (6.30):

$$\frac{\partial u_3}{\partial x_3} = -Ak^2\cos(kx_1 - \omega t) \times (-0.85^2 + 1.47 \times 0.39) \quad \text{where } x_3 = 0 \tag{6.40}$$

$$\frac{\partial u_3}{dx_3} = 0.15Ak^2 \cos(kx_1 - \omega t) \tag{6.41}$$

Substituting into equations (6.38) gives

$$\sigma_{11} = \lambda\left(-1.26Ak^2 \cos(kx_1 - \omega t) + 0.15Ak^2 \cos(kx_1 - \omega t)\right)$$

$$\sigma_{11} = -1.11\lambda Ak^2 \cos(kx_1 - \omega t) \tag{6.42}$$

Note that compression is negative.

The horizontal stress (equation 6.42) and the vertical skin acceleration associated with the Raleigh wave (equation 6.36), are in phase i.e. the stress associated with the Rayleigh wave in the hangingwall is tensile, while the hangingwall accelerate upwards.

$$\frac{\sigma_{11}}{a_3} = \frac{-1.11A\lambda k^2 \cos(kx_1 - \omega t)}{-0.62Ak\omega^2 \cos(kx_1 - \omega t)} = 1.79\frac{\lambda}{\omega c_R} \tag{6.43}$$

because $c_R = \frac{\omega}{k}$

From equation (6.42)

$$\sigma_{11} = \frac{1.79\lambda a_3}{\omega c_R}. \tag{6.44}$$

6.3 Application

The stability of the largest keyblock is investigated: i.e. the block geometry is defined by extension and shear fractures terminating at the hangingwall surface immediately next to the support units.

All partings are assumed to have no cohesion. This is a realistic assumption as shearing parallel to the bedding is common in immediate and deep mines, destroying any inherent cohesion. The horizontal hangingwall stress acting perpendicular to the stope face is generated by two mechanisms, namely rock dilation and block rotation (Daehnke et al., 1999; and Napier et al., 2001).

Note:

Assuming a local coordinate system in the hangingwall as shown in Figure 6.20 (b).

$g = -9.8\ m/s^2$ is a downward acceleration, thus W will be negative (i.e. a downward-acting force)

Compression is negative

V_1	=	Frictional resistance
m_f	=	Coefficient of friction
s_x	=	*In-situ* compressive stress
s_{11}	=	Stress associated with Rayleigh wave
s_h	=	Resultant horizontal stress
W	=	Weight of the keyblock
H	=	Keyblock height
S	=	Maximum unsupported span = length of keyblock
L	=	Width of keyblock

6.3.1 Static conditions

Consider a keyblock with the geometry shown in Figure 6.17.

Under static conditions, this keyblock is unconditionally stable if the following requirements are met:

$$V_1 \geq -\frac{1}{2}W \quad (6.45)$$

where V_1 = Frictional resistance

$$W = \rho g V \quad (6.46)$$

and

$$V = SHL \quad (6.47)$$

Thus, in order for the keyblock to be stable, under static conditions:

$$V_1 \geq -\frac{1}{2}\rho\, g\, SHL \quad (6.48)$$

6.3.2 Dynamic conditions

Under static conditions, the horizontal stress, and the weight of the keyblock remain constant. Under dynamic conditions, neither the weight of the keyblock nor the horizontal stress remains constant. The vertical acceleration of the keyblock due to the Rayleigh wave can be calculated from the displacement (u_3). Considering a Poisson solid for which $l = m$ and v=0.25, the vertical acceleration associated at the free surface with the Rayleigh wave is given by equation (6.49) and (6.36).

$$a_3(t) = \frac{\partial v_3}{\partial t} = -0.62\, Ak\, w^2 \cos(kx_1 - wt). \qquad (6.49)$$

An upward acceleration will give a positive value for a_3, while a downward acceleration will give a negative value for a_3. The effective weight of the keyblock can be calculated using equation

$$W_{eff} = m[a_3(t) - g] = rV[a_3(t) - g] \qquad (6.50)$$

Thus from Equation 6.49, if the hangingwall is accelerated upwards, the effective weight of the keyblock increases, and if the hangingwall is accelerated downwards, the effective weight of the keyblock decreases.

For stability under dynamic conditions:

$$V_1 \geq -\tfrac{1}{2}W_{eff} \qquad (6.51)$$

Note also that equation (6.50) only holds at the free surface.

6.3.3 Dynamic stress due to the Rayleigh wave interaction with the stope

The resisting force V_1 will hold the keyblock in place, depending on the magnitude of the horizontal compressive stress, s_x:

$$s_h(t) = -s_x + s_{11}(t) \qquad (6.52)$$

where $s_{11}(t)$ is positive, as the stress associated with the Rayleigh wave in the hangingwall is tensile. Thus, $s_h(t)$ is negative if the resultant horizontal stress is compressive and positive if the resultant stress is tensile.

s_x = *In-situ* compressive stress

s_{11} = Stress associated with Rayleigh wave

s_h = Resultant horizontal stress

For, $V_1 = m_f s_h$ there exists a critical stress, s_h^{crit} *(t),* such that resisting force will hold the keyblock in place, $V_1 \geq -\frac{1}{2}W_{eff}$ *(t)*

$$s^{crit}{}_h(t) = \max\left\{\frac{-W_{eff}}{2m_f}\right. . \tag{6.53}$$

6.3.4 Behaviour of a small hangingwall block in a Rayleigh wave

From equation (6.52), it can be seen that the resisting forces V_1 which will hold the keyblock in place depend on the magnitude of the horizontal compressive stress σ_x.

$$s_h(t) = s_x - s_{11}(t) \tag{6.54}$$

where:

σ_x = *In-situ* compressive stress (positive = compressive)

(Note that tensile stress is unsustainable in heavily fractured rock, such as the hangingwall of a deep-level stope). As most rock is therefore stress free, or in compression, it is convenient to call this stress "state positive",

σ_{11} = Skin stress associated with a Rayleigh wave (positive tension, as in previous sections),

σ_h = Resultant horizontal stress (positive compression).

The horizontal stress and vertical acceleration associated with the Rayleigh wave are in phase at each frequency: i.e. when the stress associated with the Rayleigh wave is tensile, the hangingwall will be accelerated upwards.

In this brief analysis, we will use a sign convention that keeps as positive (≥ 0) the "normal" or "desirable" condition encountered when describing the behaviour of this block. A positive sign will be used for:

1. Vertical displacement, velocity and acceleration of the block upwards, as in Figure 6.20.

2. Weight, or downward force, of the block. It will be expressed in terms of the weight per unit area of exposed hangingwall.

3. Support resistance in an upward direction. This resistance is provided by frictional resistance to compressive stresses acting on the sides of the block. As for the block weight, the support resistance will be expressed in terms of the weight per unit area of exposed hangingwall.

Note that the block is stationary if the two vertical forces acting on it are equal and opposite. For the quasi-static case of no seismic waves, use

σ_W = weight / area of H/W

= frictional support acting on the side of the block / area of H/W.

$$\sigma_W = \frac{\rho \times H \times L \times W \times (g - a_3)}{L \times W} = \rho \times H \times (g - a_3) \quad (6.55)$$

Let s_F be the maximum absolute vertical stress on the block from friction equal to:

$$\sigma_F = MAX(0.0, \frac{-\sigma_h \times m \times 2 \times L \times H}{S \times L}) \quad (6.56)$$

$$\sigma_F = MAX(0.0, \frac{-\sigma_h \times m \times 2 \times H}{S}) \geq 0 \quad (6.57)$$

Assume:

Height (H) = 1.0m

Span (S) = 1.5 m

Friction (μ) = 0.6

Each recorded seismogram consists of many swings of positive and negative values of displacement, velocity and acceleration. In this analysis, the relative motions of the block with respect to the surrounding rock mass need to be established.

Taking

a_B as relative acceleration; block – country rock

v_B as relative velocity; block – country rock

u_B as relative displacement; block – country rock

If $|\sigma_W| \leq \sigma_F$ is always true, than the block will be held firmly by the surrounding country rock, there will be no relative motion and it will move up and down as part of the overall rock mass. This scenario and four others are listed here.

Table 6.2 Effect of forces on hangingwall stability

σ_W and σ_F	v_B	Friction	a_B	Comments
$\|\sigma_W\| \leq \sigma_F$	0.0	0	0.0	Stable
$\sigma_W > \sigma_F$	All	Up	$(-\sigma_W + \sigma_F) / (\rho H)$	Downwards unstable
$\sigma_W < -\sigma_F$	All	Down	$(-\sigma_W - \sigma_F) / (\rho H)$	Upwards unstable
$\|\sigma_W\| \leq \sigma_F$	$v_B > 0$	Down	$(-\sigma_W - \sigma_F) / (\rho H)$	Decelerate upwards velocity
$\|\sigma_W\| \leq \sigma_F$	$v_B < 0$	Up	$(-\sigma_W + \sigma_F) / (\rho H)$	Decelerate downwards velocity

In principal, if the block is in contact with the overlying rock, than we have a restriction that u_B may not be positive, or $u_B \leq 0$. This is unlikely to be tested for several reasons.

1 The weight of the block due to gravity is always working downwards, giving a bias towards u_B.

2 From equation ($s_{11} = \frac{1.79\, l a_3}{\omega c_R}$) above, a single-frequency Rayleigh wave induces compressional skin stress ($s_{11} < 0.0$) when the rock mass is accelerating downwards ($a_3<0$).

This will assist in clamping the block so that it will follow the country rock downwards. In contrast, tensile stresses are induced ($s_{11} > 0.0$) while the country rock is accelerating upwards ($a_3<0$). This will lead to a tendency for leaving the behind. Although this is true of any single frequency, there might be events for which the net effect is upward acceleration and final displacement of the block.

The sides of the hangingwall blocks are neither vertical nor parallel. Blocks wider at the bottom than the top will be preferentially ejected.

Points 1 and 2 above are supported by the numerical simulations presented by Hildyard in the final report for SIMRAC's GAP 601b, output 3.1. These simulations resulted in downward movement of the block due to a "ratcheting" process.

When working with digitised seismograms, such as those recorded by underground networks, the relative block velocity and displacement can be obtained from relative acceleration as follows:

$$v_B^i = v_B^{i-1} + a_B^i \times \Delta t \qquad (6.58)$$

and

$$u_B^i = u_B^{i-1} + v_B^i \times \Delta t \qquad (6.59)$$

where *Ät* is the sampling interval.

6.3.5 Application of a block model to a sample seismogram

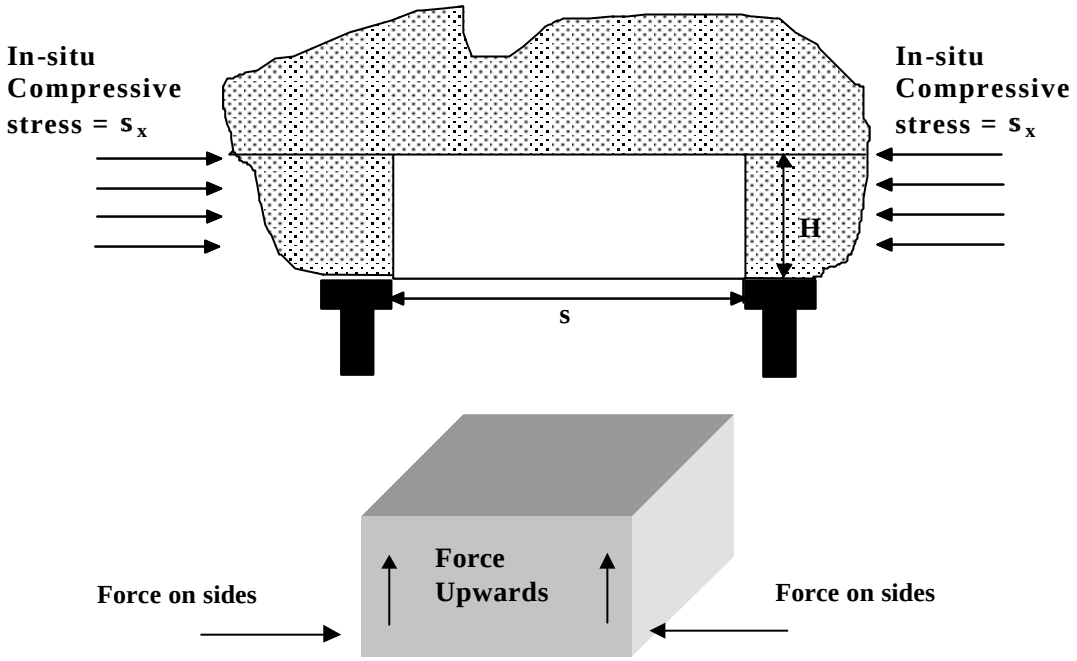

Figure 6.21 Diagram showing a hangingwall block set within the country rock

A sample seismogram from a vertical geophone recorded from a M = 0.8 event was used. The entire seismogram was amplified until the peak velocity was 0.18 m/s. The block model documented above was applied using the following parameters:

Density ρ = 2 700 kg/m^3

H = 1.0 m

σ_x = 1.0 MPa and 2.0 MPa compressive

μ = 0.6

λ = 30 000 MPa

c_R = 3 300. m/s

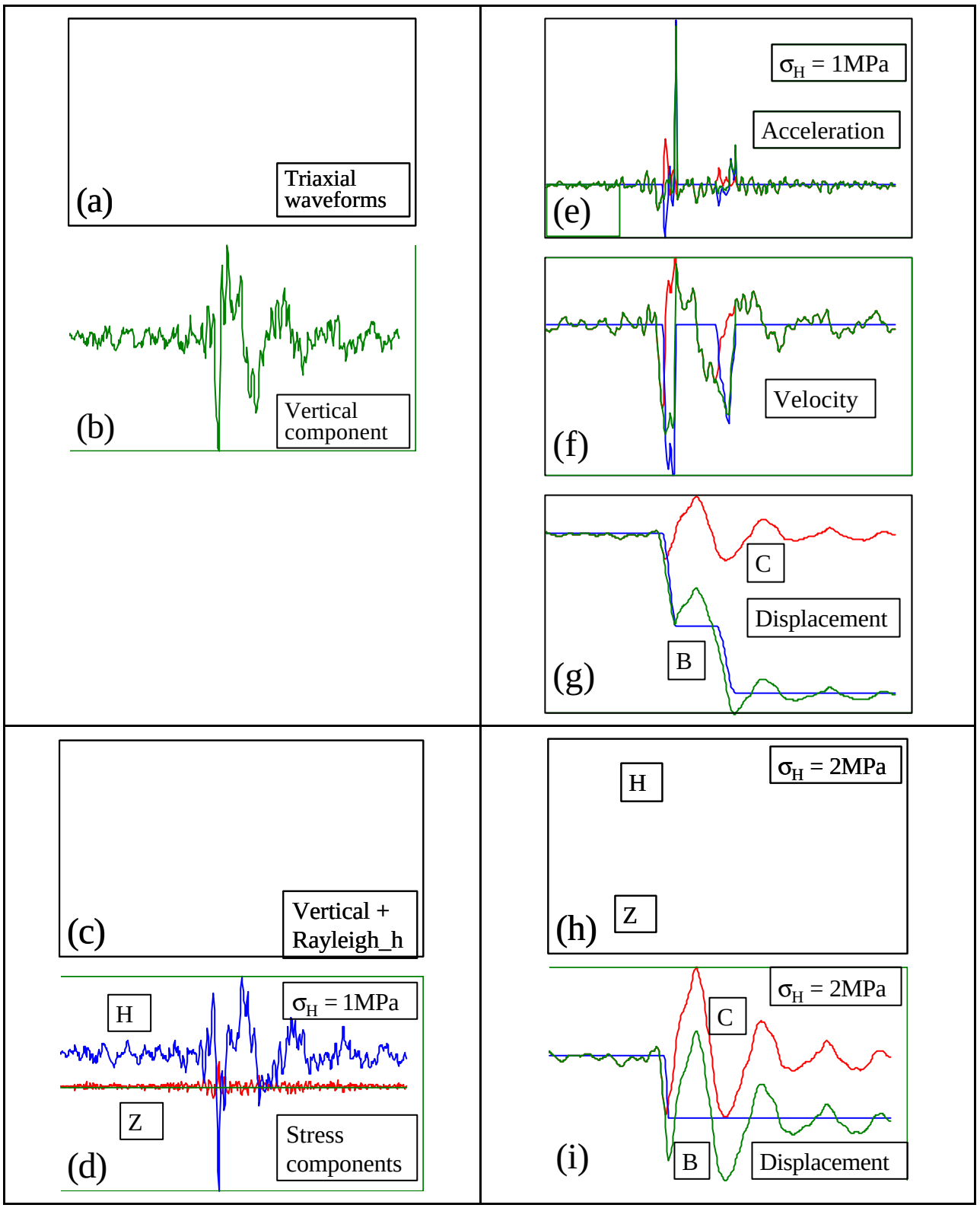

Figure 6.22 Interpretation of seismograms in terms of Rayleigh-wave block model. Pictures (a) to (i) are described in Table 6.3. For black and white printing, the annotations are: H = horizontal, Z = vertical, C = country; B = block and block-country. Signal duration about 400 msec. Corner frequency 45 Hz

Table 6.3 Description of the nine pictures in Figure 6.23

Figure 1.	Description	σ_{11}, MPa	Red	Blue	Green
(a)	Seismograms	-	H1	H2	Z
(b)	Vertical only	-			Z
(c)	Rayleigh velocities	-	Z	H	0
(d)	Stress components	1	Weight (Z)	Friction (H)	0
(e)	Acceleration	1	Country	Block - country	Block
(f)	Velocity	1	Country	Block - country	Block
(g)	Displacement	1	Country	Block - country	Block
(h)	Stress components	2	Weight (Z)	Friction (H)	0
(i)	Displacement	2	Country	Block - country	Block

Table 6.4 Values of peak ground motion of the country rock and relative motion of the block with respect to the country rock

Type		σ_x, MPa	Country	Block-country	Units
Displacement	Min	1.0	-0.52	-1.74	mm
	Max		+0.71	0.00	
Displacement	Min	2.0	-0.52	-0.64	mm
	Max		+0.71	0.00	
Velocity	Min	1.0	-0.18	-0.33	m/s
	Max		+0.15	+0.02	
Acceleration	Min	1.0	-110	-237	m/s^2
	Max		+204	+387	

6.3.6 Stability diagram from Rayleigh-wave block model

Sub-section 6.2.3 provides equations that relate ground velocity, ground acceleration and skin stress of a single-frequency Rayleigh wave to an amplitude factor *A*, wavelength *k*, frequency w and Lamé's constants l=m. Maximum values of velocity (v_3), acceleration (a_3) and skin tensile stress (s_{11}) and Rayleigh wave velocity (c_R) are provided by:

$$v_3 = 0.62Ak\boldsymbol{w} \tag{6.60}$$

$$a_3 = 0.62\ Ak\,\boldsymbol{w}^2 \tag{6.61}$$

$$\boldsymbol{s}_{11} = -1.11\,\boldsymbol{l}Ak^2 \tag{6.62}$$

$$c_R = \frac{\boldsymbol{w}}{k} \tag{6.63}$$

The PVD directly provides estimates of vertical velocity v_3 and vertical acceleration a_3. From equations (6.60), (6.61), and (6.63), the skin stress can be directly estimated from the vertical velocity through:

$$\boldsymbol{s}_{11} = \frac{-1.79\,\boldsymbol{l}v_3}{c_R} \tag{6.64}$$

From the block model analysis, the following relationships apply:

$$\boldsymbol{s}_W = \boldsymbol{r} \times H \times (g + a_3) \tag{6.65}$$

$$\boldsymbol{s}_F = \frac{-\boldsymbol{s}_h \times \boldsymbol{m} \times 2 \times H}{S} \tag{6.66}$$

From these equations, if we are to be assured of no relative movement between the hanging wall block and the country rock, the quasi-static compressive skin stress must overcome the induced tensile stress accompanying the Rayleigh wave (s_W) as well as provide enough frictional resistance to accelerate the block upwards (s_F). For each event, such as that marked "A", the skin stress required for stability is obtained by applying equation (6.64) to point "C". This point is derived from the sum of two stress values, namely:

- the skin stress required to overcome induced tension (0 – B), and
- the skin stress required to move the block against both gravity and measured upward acceleration (B – C).

The effect of (s_W) and (s_F) is illustrated in Figure 6.23.

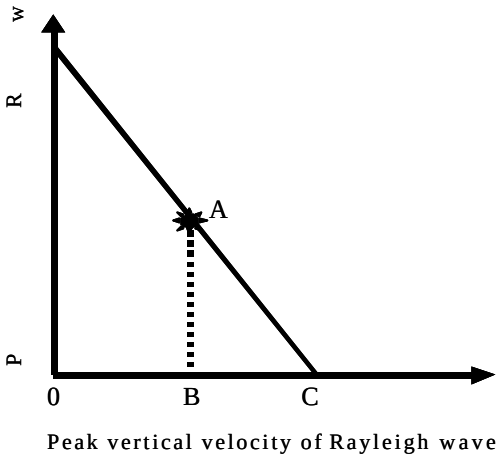

Figure 6.23 A diagram illustrating the stability of hangingwall block during interaction with Rayleigh wave

This model was applied on real seismic data recorded underground at TauTona mine. The velocity against the acceleration was plotted for the largest pulse of each event. The results are illustrated in Figure 6.24.

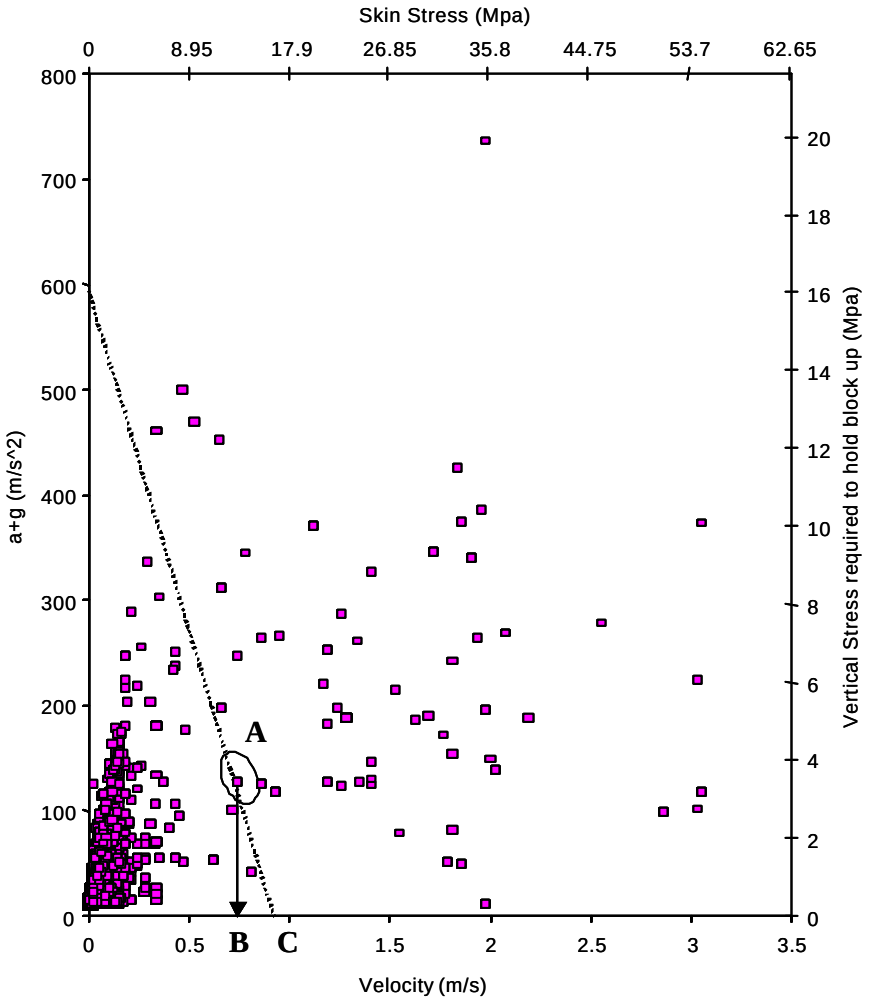

Figure 6.24 Maximum velocity against maximum acceleration, on the left hand scale, and vertical stress against skin stress, on the right hand scale

It is, however, interesting to note that the equations used to calculate the skin stresses were empirically defined on the bases of homogeneous material. Applying these equations to a real strata leads to extremely high skin stresses visible in Figure 6.24.

6.4 Discussion on Rayleigh waves

The work described in this section is more extensive than previous work on Rayleigh waves around deep-level stopes, but should still be viewed as preliminary. The identification of Raleigh waves within seismograms recorded on the hanging wall is still needed.

Previous attempts to do this have followed the classical seismological approach of using hodograms. The hodograms are plots of one component of ground motion against another for data over limited time windows. These hodograms show the elliptical motion characteristic of single-frequency data. The strong velocity increase of wave velocities with depth in the earth causes the frequency dispersion that is developed over thousands of kilometres of earth's surface. The stope hangingwall does not even approximate these ideal conditions. The following method is suggested for the identification of Raleigh waves.

Generate two functions, each containing the maximum cross correlation coefficient for overlapping windows of a function of the vertical component with each of resolved directions of the horizontal components resolved into many directions. The two functions of the vertical seismograms will be:

- Simply the seismogram itself. For pure P- or S-waves, a good cross-correlation will indicate the direction of propagation for P-waves and a direction normal to the direction of propagation for S-waves. Inspection of seismograms recorded in stopes dose not reveal obvious linear polarisation, as typically seen in seismograms recorded in solid rock.

- The equivalent horizontal seismogram assuming that the vertical component is a Rayleigh wave, as shown in Figure 6.22 (point "C") above.

- Good cross-correlations between the vertical and the radial component and the recorded horizontal motions will indicate the presence of Rayleigh waves.

6.5 Summary and recommendations

Rayleigh waves have been identified as possible mechanisms for producing falls of ground, particularly between support elements.

The stability of the hangingwall is controlled by vertical and horizontal ground accelerations and by horizontal stress induced by Rayleigh wave motion.

The horizontal stress is controlled by ground velocity and the effective modulus of the hanging wall.

It is recommended that:

- Future studies are carried out in underground sites to measure and quantify how the ground velocity, effective modulus and the stability of the hangingwall influence horizontal stresses.

- To estimate the maximum velocity that can influence hangingwall stability, it would be useful to investigate how fracture zones of varying length within the hangingwall would be influenced by wave velocity.

- GAP 601 has shown that the effect of Rayleigh waves becomes more complicated with more hangingwall blocks: further work investigating the effect of Rayleigh waves on multiple layers of blocks would give some interesting insights into how Rayleigh waves affect hangingwall fracture zones.

The development of these tasks will benefit some of the fundamental rock mass and support engineering criteria where the discontinuous nature of the hangingwall was taken in to account. The tensile stresses associated with the propagation of Rayleigh waves through the hangingwall have the ability to open up the existing joints and fractures, thus relaxing the horizontal clamping stresses. Whether or not a keyblock can be displaced relative to the surrounding rock mass is dependent on the magnitude of the horizontal compressive stress, the magnitude of the tensile stress associated with the Rayleigh waves, the frequency and amplitude of the Rayleigh waves. The support design criteria such as areal coverage, support spacing, zones of support influence as well as type of support and consistency of support performance are directly involved in this process.

7 Application of the PPV results and improved rockburst support criteria to formulate a new rockburst support design methodology

The current design methodology used in South African gold and platinum mines is based predominantly on experience and practices, and cost considerations. The most widely used support design criterion for rockburst-prone mines is based on the work of Wagner (1984), which takes into account the kinetic and potential energy of the keyblocks. The criterion for effective rockburst-resistant support systems is thus to absorb the kinetic and potential energy associated with the hangingwall moving with an initial velocity of 3 m/s. The validity of this velocity criterion was investigated in this project based on large number of underground measurements.

The hangingwall stability during the interaction with passing Rayleigh waves was investigated independently in the course of this project.

New Improved Stope Support Design Methodology (ISSDM) for rockburst conditions is proposed in this chapter. The new support design methodology incorporates the existing stope support methodology based on zones of influence, keyblock stability and tributary area theories, and the physics of hangingwall stability during the interaction with passing Rayleigh waves.

7.1 Re-evaluation and optimisation of rockburst support criteria for stopes and tunnels

The velocity criterion used in the design of rockburst-resistant support systems was verified based on a large number of underground measurements of peak particle velocities made in different geotechnical areas. Special attention was paid to understand the variations of the site response in respect of peak particle velocities and some important seismic parameters that have a direct influence on stope support. Statistical analyses, including probability evaluations were made to complete the picture.

The maximum recorded PPVs were 3 054 mm/s at TauTona; 2 846 mm/s at Kloof and 2 338 mm/s at Mponeng.

The velocity criterion of 3 m/s was found to be appropriate for the design of rockburst-resistant support systems. In particular, the analysis of the recorded data during the project rejected any alternative support design criterion based on PPV = 2 m/s or less.

Following the statistical analysis described in section 5, a bimodal distribution of the PPVs was found in all data sets recorded at TauTona, Kloof and Mponeng mines. Some of the features common to the PPV (v) distributions shown in Figures 5.5, 5.6 and 5.7 are listed below:

- The maximum expected PPVs estimated using the maximum likelihood approach (with a minimum and a maximum) were 3548 mm/s at TauTona; 3311 mm/s at Kloof and 3 162 mm/s at Mponeng.

- the smallest value of v, above which the data appears to be complete, is v_M = 10 mm/s to 30 mm/s (limited by the amount of memory available)

- a power-law behaviour ($N \sim v^{-P}$) with $p \gg 1$ provides a good fit to the TauTona data and a less accurate fit to the data from Kloof and Mponeng;

- all three mines, particularly Kloof and Mponeng, show a distinct deviation from the $N \sim v^{-1}$ fit for 0.1 m/s < v < 1.0 m/s; and

- the $N \sim v^{-1}$ fit is good for 0.01 m/s < v < 0.1 m/s for all mines, except for some flattening at lower values for the Mponeng data.

These distributions are commonly described as bimodal behaviour with peaks at 0.1 m/s and 1.0 m/s. A physical model was suggested to describe this behaviour. The model would consider the effect of the near-field strong ground motion on the underground mining excavations.

7.1.1 Sources of near-field strong ground motion

Brune (1970) proposed a model of a seismic shear-slip source in terms of an instantaneous stress drop over a circular fault patch. The best-known result of this model is a relationship between the corner frequency of shear waves and the source radius. This relationship is still

commonly accepted. Brune also showed that the maximum ground velocity in this model is related to the instantaneous stress drop by:

$$v = \frac{tb}{G} \tag{7.1}$$

where v is PPV; t is the instantaneous stress drop; b is shear-wave velocity and G is the modulus of rigidity.

Ryder (1988) has suggested various stress drops: 20 MPa (on p.29) and 30 MPa (on p.31) for intact rock. For typical values of β = 3700 m/s and G= 30 GPa, this converts to $v \approx 3$ m/s. 3 m/s is specified as the required yield values of rockburst-resistant support. Although the choice of 3 m/s is not very clearly motivated, this line of reasoning played a part in the final decision to use 3 m/s for design of rockburst-resistant support.

Without reference to equation (7.1), McGarr (2001) has proposed a number of lines of evidence and available data that suggests an upper limit of 1.5 m/s in the source region. However, his concluding statements read:

"The main caveat to this possibility (of a limit of 1.5 m/s) is the possibility, supported by many observations underground (Ortlepp, 1997), that the shear zone of a mining-induced earthquake ruptures previously-intact rock, at least over small regions. If so, then near-fault ground velocities several time greater than 1.5 m/s would be anticipated locally in these higher strength zones."

Natural earthquakes most often involve slip on faults with no cohesive strength at all, with the fault filled with crushed rock, or gouge. In this case the stress drop that sets off the earthquake is understood in terms of static and dynamic friction. A large body of literature refers to "rate- and state-dependent friction" (e.g. Marone, 1998). Laboratory experiments performed and also summarised by Marone (1998) and work reported by McGarr (1993) indicate that the stress drop from static to dynamic friction is no more than a few percent. Assuming that the loading shear stress is 40 MPa, a stress drop of 1 MPa is not unreasonable. This converts to $v \approx 0.1$ m/s.

In a simple sense, two possible near-field ground velocities can be worked with:

- v = 3.0 m/s when driven by failure of intact rock, and
- v = 0.1 m/s when driven by dynamic stress drop on previously failed shear planes.

Note that these velocity values have not been ascribed to individual seismic events. What is suggested in this simple model is that every point, or patch, on the active area of every event is subject to one or the other of these mechanisms, with some modifications that will be motivated later on in this report.

7.1.2 Near- and far-field behaviour

The previously proposed equations that describe the strong ground motion on the (extended) plane of a shear slip (Daehnke et al., 1999a) were used in this model. The change from near-field to far-field on the extension of the slip plane can be approximated by:

$v_N = (bt / G)$ for $R \leq r_0$, (7.2)

$v_F = (bt / G) * (r_0/R)$ for $R \geq r_0$ (7.3)

where r_0 = source radius, R is the distance from the centre of the source and v_N and v_F are the near-field (on-patch) and far-field ground velocities respectively.

7.1.3 Spatial distributions of patches

It can be assumed that each strong ground motion is caused by a circular patch centred on the reef horizon at the face of an infinitely long longwall and that the peak velocities are also measured at the face. For a single randomly placed patch, the cumulative distribution function, from large to small, of v along the face is:

$P(v) = 0$ for $v > v_N$

$P(v) = 1$ for $v = v_N$ (7.4)

$P(v) = (v / v_N)^{-1}$ for $v < v_N$

Equations (7.3) and (7.4) are truncated power-law distributions. Equation (7.3) could be used to describe the data for TauTona if the nearest, or largest patch for all events was failure of intact rock. Note that the patch size (radius r_0) does not appear in the equation at all. The dip shown in Figures 5.5, 5.6 and 5.7 is between 0.1 m/s and 1.0 m/s and then the increase at about 0.1 m/s requires further explanation. Several mechanisms can now be considered:

1 Most of the slip on failure of intact rock acts to close up the stope. The stope face outside the near-field is therefore close to the “B” axis in the radiation pattern and has a zero amplitude for homogeneous conditions. In practice, the amplitude will be reduced.

2 Strong ground motions can stimulate further slip and positive stress drop. This slip, could increase the peak velocity from “far-field” to reduced “near-field” conditions (point A in Figure 7.1). This will increase $P(v)$ for $v < v_N$.

3 Strong ground motions can increase stress above the strength and stimulate further slip although the stress drop will be negative, with the final stress higher than the initial stress (point B in Figure 7.1). This will decrease $P(v)$ for $v < v_N$. Items 3 and 4 will work together to reduce the number of observations of $v < v_N$ for observations outside the source region.

4 As suggested for stress drops due to the dynamic friction drop, another population can start acting with $v_N \approx 0.1$ m/s. This would occur if previously formed slip zones are repeatedly mobilised, driving by velocity weakening.

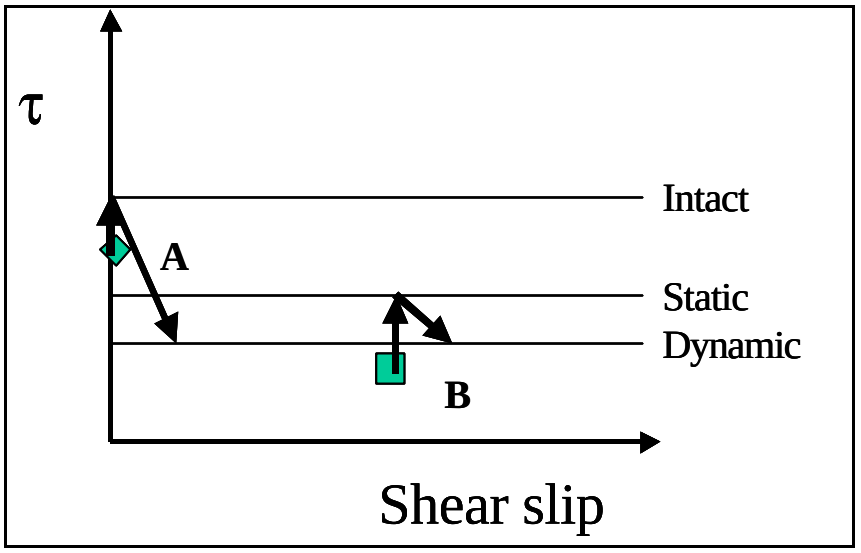

Figure 7.1 Cartoon illustrating (A) reduced stress drop and (B) negative stress drop

7.2 Improved Stope Support Design Methodology for rockburst conditions

An engineering approach to quantify stable spans of discontinuous hangingwalls is proposed. This approach combines the zones of support influence with the hangingwall stability controlled by buckling, rotating and shearing keyblocks. Many of these principles were developed under SIMRAC projects GAP 330, GAP 335 and GAP 627 and therefore less description is given in this report. A new approach involving the physical processes during the interaction between the hangingwall and propagating Rayleigh waves has been incorporated in a new engineering approach. The proposed design tool is of practical value and enables the rock engineer to make initial designs of appropriate support spacing. Figure 7.2 is a flowchart illustrating the principles of the Improved Stope Support Design Methodology (ISSDM) for rockburst conditions. Figures 7.3 and 7.4 are zoomed segments of ISSDM for cases where the support spacing is not known (most commonly the case) and the Rayleigh waves interaction with the hangingwall. A shortcut overtaking the segments shown in Figures 7.3 and 7.4 was introduced when the support spacing is known by back analyses.

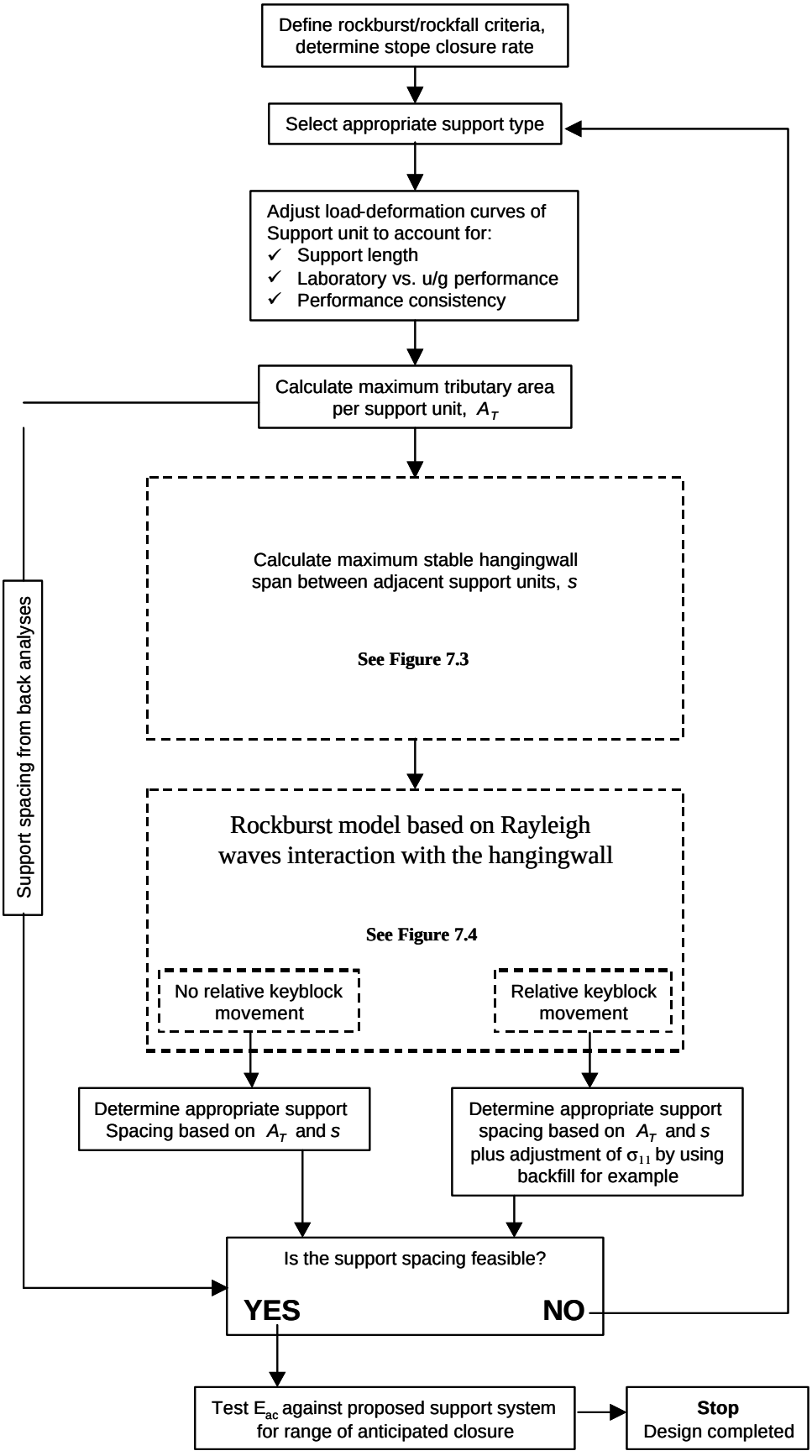

Figure 7.2 Flowchart illustrating the principles of Improved Improved Stope Support Design Methodology for rockburst conditions

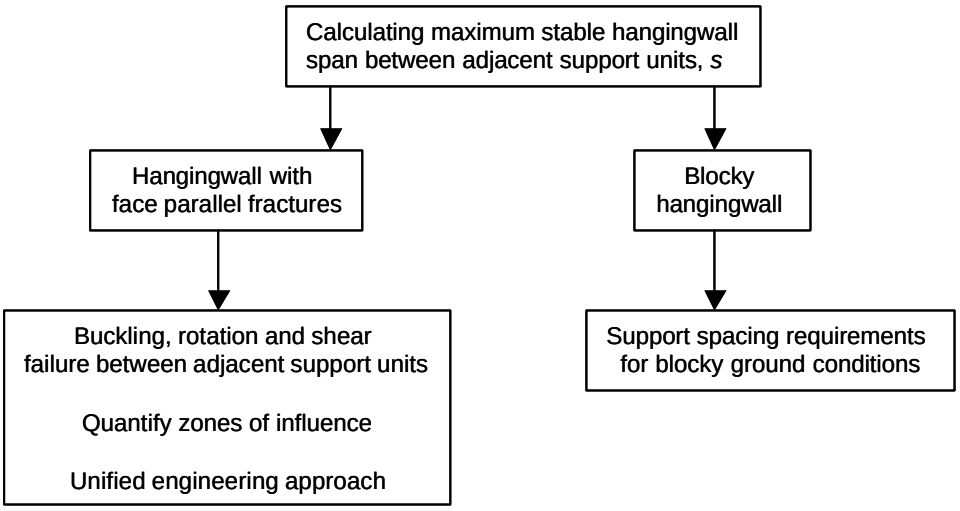

Figure 7.3 Flowchart illustrating section of support design methodology in a case when the support spacing is not known

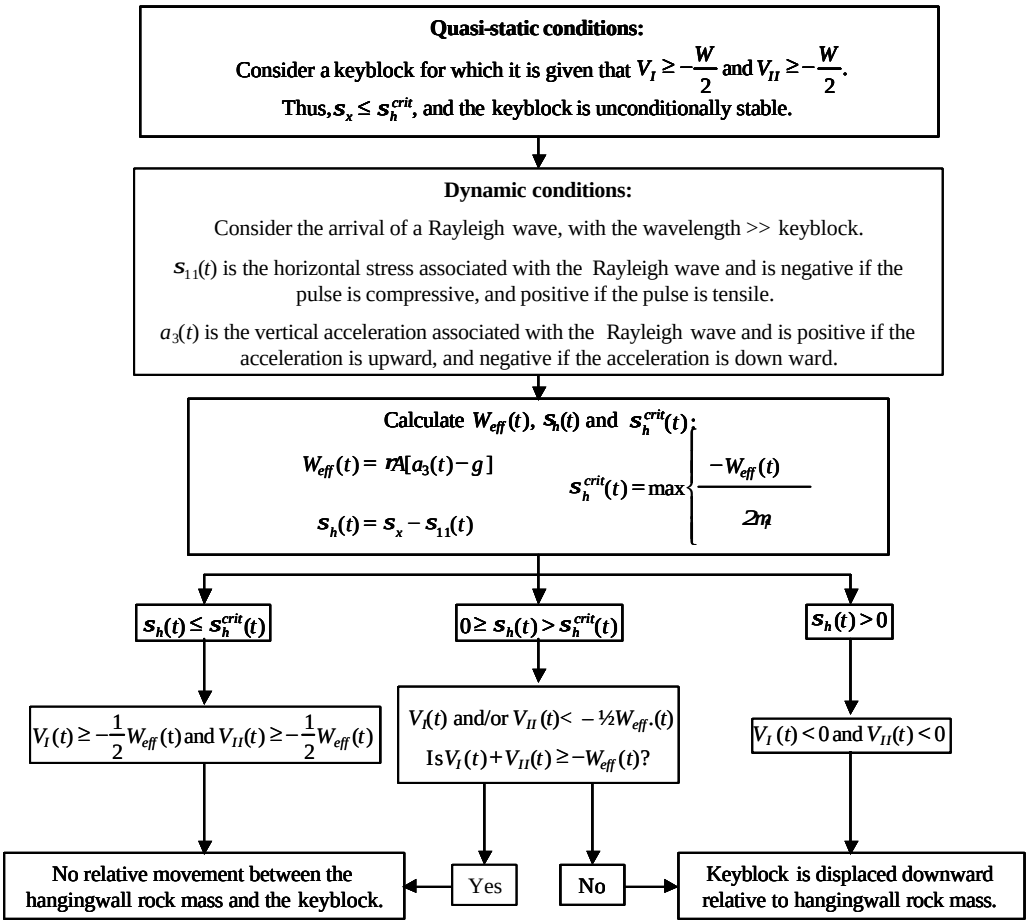

Figure 7.4 Flowchart illustrating a rockburst model based on Rayleigh wave interaction with the hangingwall

The following applies to the amount of relative displacement between a keyblock and the surrounding hangingwall rock mass, *s*:

$$s \propto v_3^{\max} \text{ and } s \propto \frac{1}{f_o}$$

The degree to which the hangingwall will unravel due to relative displacements between keyblocks and the surrounding hangingwall rock mass is a function of the keyblock shape. It is crucial to maintain compressive hangingwall stresses to ensure hangingwall stability, and support systems should be designed with this in mind. This again highlights the need for extensive areal support, i.e. headboards, safety nets, etc.

7.3 Conclusions and recommendations

7.3.1 Principles of stope support

Support design methodologies must be based on sound engineering principles to optimise support systems in terms of safety and cost. Some of the fundamental rock mass and support engineering criteria, that form the basis of an improved support design methodology, are:

(i) height of potential fall;

(ii) quasi-static stope closure rates;

(iii) dynamic stope closure rates;

(iv) compressive hangingwall stresses;

(v) discontinuity spacing, orientation and interface properties;

(vi) effect of support length (stoping width);

(vii) effect of compression rate;

(viii) consistency of support performance;

(ix) areal coverage;

(x) support spacing; and

(xi) zones of support influence.

The development of an improved support design methodology for rockfall and rockburst conditions has led to the potential for significant increases in worker safety and support cost savings. The site specific methodology consists of two stages: (i) a tributary area analysis, and (ii) a zone of support influence and a stability analysis, considering hangingwall failure due to buckling, shear and block rotation, which gives maximum safe spacing of individual support units.

For hangingwall conditions in which both the stability of keyblocks, as well as the unravelling of a blocky rock mass structure governs the rock mass integrity, it is recommended that the maximum stable spans for both blocky hangingwalls and hangingwalls with face parallel fractures be determined. In this case, the ultimate support spacing to be used should be the minimum of the blocky hangingwall and hangingwall with face parallel fractures analyses.

In deep-level mines, horizontal clamping stresses play a large role in the support design, whereas in shallower mines, where such clamping stresses are absent, probabilistic keyblock theory is used to determine appropriate support spacing.

Finally, the rock engineer should at all times apply his/her engineering judgement to design support systems offering a high probability of rock mass stability. For particularly complex rock mass structures and/or poorly understood failure mechanisms, support spacing should be further reduced and support resistance and energy-absorption capacities increased.

7.3.2 Rockburst model based on Rayleigh waves interaction with a hangingwall

An alternative rockburst model, which takes the discontinuous nature of the hangingwall into account, has been developed during the course of this project. The model focuses on the stress changes caused by the passage of Rayleigh waves along a stope.

It has been found that Rayleigh waves can indeed compromise hangingwall stability. The tensile stresses associated with Rayleigh waves have the ability to open up existing flaws (joints and/or fractures), thus relaxing the horizontal clamping stresses. Whether or not a keyblock can be displaced relative to the surrounding rock mass is dependent on the magnitude of the horizontal compressive stress, the magnitude of the tensile stress associated with the Rayleigh waves, the frequency and amplitude of the Rayleigh waves, and the source distance.

A procedure for determining the effect of a passing Rayleigh wave on the hangingwall stability has been developed.

The importance of maintaining horizontal clamping stresses is again highlighted by this alternative rockburst model. The model also emphasises the need for good areal coverage to be provided by support systems.

8 Conclusions and recommendations

8.1 Summary of the results

The following main results were found during the course of the project:

(i) Development and manufacture of a PPV measuring instrument.

A cost-effective instrument especially designed for recording strong ground motion was developed and manufactured. The instrument, a Peak Velocity Detector (PVD) is a portable battery powered stand-alone device with backed-up memory capable of storing up to 512 peak particle velocities for the largest excursion exceeding some threshold during each time window of 25 seconds. Five parameters are stored per event: peak particle velocities; time of the peak; slope at the first zero crossing; slope at the second zero crossing; and peak width, measured between the nearest zero crossings - before and after.

(ii) An enlarged database of measured PPVs in stopes and tunnels in various geotechnical areas, was accumulated.

Extensive underground seismic measurements at Carbon Leader Reef and Ventersdorp Contact Reef sites were carried out. A total number of 41 sites was monitored:

a. TauTona gold mine: a total number of 15 139 seismic events with a maximum value of 3 m/s was recorded during 2 437 site days;

b. Kloof gold mine: a total number of 6 066 seismic events recorded during 659 site days with a maximum value of 3 m/s; and

c. Mponeng gold mine: a total number of 1183 seismic events recorded during 403 site days with a maximum value of 2.3 m/s.

(iii) Back-analyses of mine network data to derive the velocity amplification factors on the skin of the excavations were conducted.

The site response obtained at the surface of excavations was found to attenuate with the hypocentral distance. The exponential attenuation of the following type;

$$x = a\,e^{-bR}$$

where *a* and *b* are coefficients different for the different geotechnical areas; is proposed. However, due to the limited number of seismic events correlated at hypocentral distances longer then 500 m, the correlation coefficient for the exponential trend line is very low.

The relationship between the site response and additional seismological parameters, such as hypocentral distance, source radius, wavelength (Lambda) and maximum velocity were discussed in this report. In addition, the relationship between source radius and hypocentral distance, and source radius and magnitude was outlined in an attempt to characterise the comprehensive rock mass behaviour under dynamic loading.

(iv) A statistical procedure to estimate the probability of the occurrence of a particular PPV, was applied.

The maximum likelihood curve fits, using a maximum and a minimum, appeared to match the data recorded at TauTona very well, whereas the trend calculated using just the minimum predicted unrealistically high PPVs.

The curve fits to PPV data recorded at Kloof and Mponeng were less satisfactory, particularly towards the high end of the velocity range. This is possibly as a result of the recording period being four to six times lower than that of TauTona.

The maximum expected PPVs estimated using the maximum likelihood approach (with a minimum and a maximum) were 4 295 mm/s at TauTona; 1 799 mm/s at Kloof; and 1 862 mm/s at Mponeng.

The frequency-log(PPV) distributions for Kloof and Mponeng appeared to be bimodal. The source of the bimodality is not known, and could be an effect introduced by the instrumentation or an indication of a fundamental difference in the mechanisms of failure. It is strongly suggested that further work be done to investigate the source of the bimodality so that the appropriate statistics can be applied.

(v) Investigation was conducted into improved rockburst support criteria (in addition to the PPV criterion) for stopes and tunnels.

A rockburst model, which takes the discontinuous nature of the hangingwall into account, was developed. The model focuses on the stress changes caused by the passage of Rayleigh waves along a stope. The importance of maintaining horizontal compressive stress, to ensure hangingwall stability, is emphasised.

(vi) The PPV results and the improved rockburst support criteria were applied to formulate a new rockburst support design methodology.

The velocity criterion of 3 m/s was found to be an adequate value to meet the requirements of support systems during a rockburst. In general, the present support systems and technologies do not need to be modified significantly to cater for rockfall and rockburst conditions.

A new physical model explaining the near-field and far-field distribution of the strong ground motion was proposed.

An Improved Stope Support Design Methodology (ISSDM) was developed for rockburst conditions combining zones of support influence with hangingwall stability controlled by buckling, rotating and shearing keyblocks and the physical processes during the interaction between the hangingwall and propagating Rayleigh waves.

8.2 Recommendation for further work

Additional work is recommended in the following areas:

- The physics behind the strong ground motion in the near- and far- fields. Hypothesis to explain all causes.
- Spatial and temporal distribution of the stress drop driving strong ground motion.
- Mechanism of amplification of PPV involving the dynamic behaviour of hangingwall fractures.
- Underground measurements to quantify how the ground velocity, effective modulus and the stability of the hangingwall influence the horizontal stresses.
- Investigation of how fracture zones of varying persistence within the hangingwall would be influenced by wave velocity and especially by interaction with Rayleigh waves.
- Identification of Rayleigh waves on the seismograms recorded underground.
- Investigation of Love wave effect in geotechnical areas with prominent bedding planes e.g. “Green bar”.
- Categorization of all source distances in terms of ray-paths along the skin of the stops, backfilled areas and unmined ground.
- Assessment and reduced the location error of mine data used in this project by applying the high accuracy location procedure currently being developed under project SIM 02 03 04.

References

Aki, K. and Richards, P. G., 1980. Quantitative seismology, Freeman, San Francisco. 932 p.

Bandis, S.C., Lumsden, A.C. & Barton, N.R. 1981. Experimental studies of scale effects on the shear behaviour of rock joints. International Journal of Rock Mech. Min. Sci. & Geomech. Abstr., pp. 1-21.

Bolt, B.A. 1978. Earthquakes: a primer**,** W.H. Freeman and Company, San Francisco. 241 p.

Brune, J.N. 1970. Tectonic stress and the spectra of seismic shear waves from earthquakes, J. Geophys. Res., vol. 75, pp. 4997 – 5009. (Correction, J. Geophys. Res., vol. 76, 1971, p 5002.

Butler, A.G. and van Aswegen, G. 1993. Ground velocity relationships based on a large sample of underground measurements in two South African mining regions. Proc. of Rockburst and Seismicity in Mines, P. Young (Editors), Balkema, Roterdam, pp. 41-56.

Cichowicz, A., Milev A .M. and Durrheim, R. J., 2000. Rock mass behaviour under seismic loading in a deep mine environment, Journal of SAIMM, V 100, No 2, pp.121-128.

Cichowicz, A., 2001. The meaningful use of peak particle velocities at excavation surfaces for the optimisation of the rockburst criteria for tunnels and stopes SIMRAC Final Project Report GAP 709b. Pretoria: Department of Minerals and Energy, 28 p.

Cichowicz, A. 2001. Personal communication, ISS International, Stellenbosh

Daehnke, A., Anderson, L.M., de Beer, D., Esterhuizen, E., Glisson, F.J., Jaku, E.P., Kuijpers, J.S., Peake, A.V., Piper, p., Quaye, G.B., Reddy, N., Roberts, M.K.C., Schweitzer, J.K. & Stewart, R.D. 1998. Stope Face Support Systems, SIMRAC Final Project Report GAP 330, Pretoria: Department of Minerals and Energy, 407 p.

Daehnke, A., Van Zyl, M. & Le Bron, K.B., 1999. Quantifying zones of support influence in a discontinuous rock mass. SIMRAC Project 627. CSIR: Division of Mining Technology. Auckland Park, South Africa.

Daehnke, A., Andersen, L.M., Kuijpers, J.S. & Ntuli, J. 1999a. Quantitative rock engineering criteria for effective stope support. Final Project Report, Deepmine Task 4.1.2, CSIR Mining Technology, pp. 1-89.

Daehnke, A., Salomon, M.D.J. and Roberts, M.K.C. 2000. Quantifying stable hangingwall span between support units. Journal of The South African Institute of Mining and Metallurgy, October 2000.

Daehnke, A., Van Zyl, M. and Roberts, M.K.C. 2001. Review and application of stope support design criteria. Journal of The South African Institute of Mining and Metallurgy, May/June 2001.

Durrheim, R.J., Milev, A.M., Spottiswoode, S.M. & Vakalisa, B. 1997. Improvement of worker safety through the investigation of the site response to rockbursts, SIMRAC Final Project Report GAP 201. Pretoria: Department of Minerals and Energy, 530 p.

Driefontein gold mine, 2000. Rock Mechanics Department, Personal communication.

Geyser, D. 2001. Rock Mechanics Department, Kloof gold mine - personal communication.

Gibowicz, S.J. & Kijko, A. 1995. An introduction to mining seismology. Vol. 55, International Geophysics Series, Academic Press, San Diego, California, 399 pp.

Goodman, R.E., and Shi, G. 1985. Block theory and its application to Rock Engineering, Prentice Hall.

Gutenberg, B. & Richter, C.F. 1944. Frequency of earthquakes in California, Bull. Seism. Soc. Am., Vol. 34, 185-188.

Gutenberg, B. & Richter, C.F. 1954. Seismicity of the earth and related phenomena, 2nd Ed., Princeton University Press, Princeton, N.J.

Hagan, T.O., Milev A.M., Spottiswoode S.M., Vakalisa B. and Reddy N., 1998. Improvement of worker safety through the investigation of the site response to rockbursts. SIMRAC Final Project Report GAP 530, Pretoria: Department of Minerals and Energy, 147 p.

Haile, A.T., Grave, D.M., Sevume, C. & Le Bron, K.B. 1998. Strata control in tunnels and an evaluation of support units and systems currently used with a view to improving the effectiveness of support, stability and safety of tunnels. SIMRAC Final Project Report GAP 335, Pretoria: Department of Minerals and Energy.

Handley, M, F, 2004. Improved Seismic Locations and Location Techniques, SIMRAC GAP 9, currently in progress.

Hildyard, M.W., Napier, J.A.L., Young, R.P. 2001. The Influence of an excavation on ground motion. Proc. RASiM 5, G. van Aswegen, R.J. Durrhem and W.D. Ortlepp (Editors), SAIMM, Johannsburg'01, pp. 443-452.

Hildyard, M. 2001. Wave Interaction with Underground Openings In Fractured Rock. PhD. Thesis, University of Liverpool, 252 p.

Love, A.E.H. 1911. Some problems of geodynamics. Cambridge, England, Cambridge, at The University Press.

Marone, C. 1998. Laboratory-derived friction laws and their application to seismic faulting. Annu. Rev. Earth Planet. Sci., 26, pp. 643-696.

McGarr,A.; Green, R.W.E. and Spottiswoode, S.M. 1981. Strong ground motion of mine tremors: some implications for near-source ground motion parameters, Bull. Seism. Soc. Am., 71, pp. 295 – 319.

McGarr, A. 1991. Observations constraining near-source ground motion estimated from locally recorded seismograms. Journal of geophysical research, vol. 96. No. B10. pp. 595–508.

McGarr, A. 1993. Keynote address: Factors influencing the strong ground motion from mining-induced tremors, 3rd Intl Symp. on Rockbursts and Seism. in mines, Balkema, pp. 3-12.

McGarr, A. 2001 Control of strong ground motion of mining-induced earthquakes by the strength of the seismogenic rock Proc. RASiM 5, G. van Aswegen, R.J. Durrhem and W.D. Ortlepp (Editors), SAIMM, Johannsburg'01, pp. 69-74.

Milev, A. M., Spottiswoode S. M. and Stewart, R. D. 1999. Dynamic response of the rock surrounding deep level mining excavations. Proc. 9th ISRM, G. Vonille & P. Berset (Editors), Paris'99: 1109-1114.

Milev, A.M., Spottiswoode S.M., Rorke A. J. and Finnie G.J, 2001. Seismic monitoring of a simulated rockburst on a wall of an underground tunnel, Journal of The South African Institute of Mining and Metallurgy, August 2001.

Milev, A. M. and Spottiswoode, S.M. 1997. Integrated seismicity around deep level stopes in South Africa, Int. J. of Rock. Mech. Mining Sci. & Geo. Abstr. Vol. 34, No 3/4., p 681.

Murphy, S. K. 2000. Rock Mechanics Department, TauTona gold mine - personal communication.

Murphy, S. K. 2001. An evaluation of the effect of extensive backfilling on seismicity in longwall mining. Proc. RASiM 5, G. van Aswegen, R.J. Durrhem and W.D. Ortlepp (Editors), SAIMM, Johannsburg'01, pp. 229-236.

Murphy, S. K. 2000. Rock Mechanics Department, TauTona mine - personal communication.

Napier, J A.L. Drescher K., Hildyard, M.W., Kataka M.O., Malan D.F. and Sellers, E.J. 2002. Experimental investigation of fundamental processes in mining induced fracturing and rock instability SIMRAC Final Project Report GAP 601, Pretoria: Department of Minerals and Energy, 230 p.

Ortlepp, W.D. 1997. Rock fracture and rockbursts, South African Inst. Mining Metallurgy, Johannesburg, 98 p.

Page, R. 1968. Aftershocks and microaftershocks of the great Alaska earthquake. Bull. Seism. Soc. Am., Vol. 58, pp. 1131-1168.

Palmstrøm, A. 1996. Characterising rock masses by the RMi for use in practical rock engineering Part 1: The development of the Rock mass Index (RMi), Tunnelling and Underground Space Technology, 11(2), Pergamon Press.

Rayleigh, J.W.S. 1887. On waves propagating along the surface of an elastic solid. Proc. Lond. Math. Soc., 17, pp. 4-11.

Roberts, M.K.C., Jager, A.J. & Riemann, K. 1987. The performance characteristics of timber props. Chamber of Mines Report no. 35/87.

Roberts, M.K.C. 1995. Final Report on Stope and Gully Support, CSIR: Division of Mining Technology, Project Gap 032. Auckland Park, South Africa

Roberts, M.K.C. 1999. The design of stope support systems in South African gold and platinum mines. University of Witwatersrand. Ph. D. thesis.

Russel, D. 1999. Acoustic Animations, Kettering University, Applied Physics.

Ryder, J.A. 1988. Excess shear stress in the assessment of geologically hazardous structures. J. S. Afr. Inst. Min. Metall. 88, pp. 27-39.

Squelch A.P., Milev A. M., Dlokweni, T., Acheampong, E., Janse van Rensburg A and Watson B.P. 2002. Influence of regional support systems (pillars and backfill) on local areas and internal support requirements adjacent to that regional support. SIMRAC Final Project Report GAP 615, Pretoria: Department of Minerals and Energy, 130 p.

Smit, J., Erasmus, N. & Grobler, R. 1998. Report on Durapak® design methodology and findings of the rapid load tests conducted in Germany, March 1998.

Spottiswoode, S.M. Durrheim, R.J. Vakalisa B. and Milev A.M. 1997 Influence of fracturing and support on the site response in deep tabular stopes Proc. 1st Southern African Rock Engineering Symposium, (Editors) R.G. Gurtunca and T.O. Hagan, SANGORM, pp 62-68.

Stilborg, B. 1986. Professional users handbook for rock bolting. Series on Rock and Soil Mechanics. Vol 15. Atlas Copco. Sweden.

Taggart, P.N. 1994. Dynamic laboratory testing of pack based support elements. Part I. The laboratory evaluation of timber and composite packs, single rise pack elements and grout based prestressing. Interim Report for SIMRAC Project GAP 032, CSIR: Division of Mining Technology.

Taggart, P.N. 1994a. Dynamic laboratory testing of pack based support elements. Part II. The laboratory evaluation of two types of grout based pack prestressing. Interim Report for SIMRAC Project GAP 032, CSIR Mining Technology.

Lay, T. and Wallace, T.C. 1995. Modern Global Seismology, Academic Press, London.

Wagner, H. 1984. Support requirements for rockburst conditions. Proc. of the 1st International Congress on Rockbursts and Seismicity in Mines, Johannesburg, 1982. SAIMM, N.C. Gay and E.H. Wainwright (Editors) Johannesburg, pp. 209-218.

Van Zyl, M. 2001. Development of an extended support design methodology and alternative rockburst model (MSc Topic), Johannesburg

Ward, A. 2002. Rock Mechanics Department Mponeng mine – personal communication.

Appendix A

The mathematical formulation to estimate maximum velocities using methodology described in Gibowicz & Kijko (1995)

The equation describing Gutenberg-Richter frequency-magnitude distribution can be rewritten in terms of velocity as:

$$\log n = c - d(\log v) \tag{A1}$$

where n is the number of seismic events having velocity v; and c and d are parameters. Parameters c and d can be calculated from the y-intercept and slope of the linear portion of the curve.

If the logarithms of the velocity of the seismic events are assumed independent, identically distributed random variables, equation (A1) (Gibowicz & Kijko, 1995) can be written as:

$$f(\log(v)) = \begin{cases} 0 & for \quad \log(v) < \log(v_{\min}) \\ \beta \exp[-\beta(\log(v) - \log(v_{\min}))] & for \quad \log(v) \geq \log(v_{\min}) \end{cases} \tag{A2}$$

$$F(\log(v)) = \begin{cases} 0 & for \quad \log(v) < \log(v_{\min}) \\ 1 - \exp[-\beta(\log(v) - \log(v_{\min}))] & for \quad \log(v) \geq \log(v_{\min}) \end{cases} \tag{A3}$$

where $f(\log(v))$ and $F(\log(v))$ are the probability density and cumulative distribution functions of $\log(v)$, and $\beta = d\ln(10)$. The cumulative distribution function of $\log(v)$ (equation (A3)) does not have a restriction on the upper limit to the PPV and hereafter is referred to as “unbounded”.

It can be shown that this equation takes the same form as equation (A1) by rearranging the terms and taking the natural logarithm of both sides of the equation:

$$F(\log(v)) - 1 = -\exp(-\beta(\log(v) - \log(v_{\min}))) \qquad for \qquad \log(v) \geq \log(v_{\min}) \tag{A4}$$

$$\ln(1 - F(\log(v))) = -\beta(\log(v) - \log(v_{\min})) = \beta\log(v_{\min}) - \beta\log(v) \tag{A5}$$

To convert to $\log_{10}$:

$$\frac{\ln(1 - F(\log(v)))}{\ln(10)} = \frac{\beta\log(v_{\min})}{\ln(10)} - \left(\frac{\beta}{\ln(10)}\right)\log(v) \tag{A6}$$

This equation has the same form as equation (A1) if

$$\frac{\ln(1-F(\log(v)))}{\ln(10)} = \log(n), \qquad \frac{\beta\log(v_{\min})}{\ln(10)} = c \qquad \text{and} \qquad \frac{\beta}{\ln(10)} = d \qquad \text{(A7)}$$

The maximum likelihood estimate of β can be calculated using

$$\hat{\beta} = \frac{1}{\langle\log(v)\rangle - \log(v_{\min})} \qquad \text{(A8)}$$

where $\hat{\beta}$ is the maximum likelihood estimate of β and $\langle\log(v)\rangle$ is the mean of the sample such that $\langle\log(v)\rangle = \sum_{i}^{n}\frac{\log(v_i)}{n}$ where $\log(v_i) \geq \log(v_{\min})$.

The maximum-likelihood procedure just described has a significant shortcoming in that the $\log(v)$ are unbounded from the top (i.e. no $\log(v_{\max})$ is considered). Many seismologists believe that there must exist an upper limit to the earthquake magnitude. Equivalently, there must also exist an upper limit to the peak particle velocity.

If an upper limit for $\log(v)$ is introduced, the density and cumulative probability distribution functions take the following form (Page,1968):

$$f(\log(v)) = \begin{cases} 0 & \textit{for} \quad \log(v) < \log(v_{\min}) \quad \textit{and} \quad \log(v) > \log(v_{\max}) \\ \dfrac{\boldsymbol{b}\exp[-\boldsymbol{b}(\log(v)-\log(v_{\min}))]}{1-\exp[-\boldsymbol{b}(\log(v_{\max})-\log(v_{\min}))]} & \textit{for} \quad \log(v_{\min}) \leq \log(v) \leq \log(v_{\max}) \end{cases} \qquad \text{(A9)}$$

$$F(\log(v)) = \begin{cases} 0 & \textit{for} \quad \log(v) < \log(v_{\min}) \\ \dfrac{1-\exp[-\boldsymbol{b}(\log(v)-\log(v_{\min}))]}{1-\exp[-\boldsymbol{b}(\log(v_{\max})-\log(v_{\min}))]} & \textit{for} \quad \log(v_{\min}) \leq \log(v) \leq \log(v_{\max}) \\ 1 & \textit{for} \quad \log(v) > \log(v_{\max}) \end{cases} \qquad \text{(A10)}$$

where $f(\log(v))$ and $F(\log(v))$ are the probability density and cumulative distribution functions of $\log(v)$ and the maximum-likelihood equation for β is:

$$\frac{1}{\boldsymbol{b}} = \langle\log(v)\rangle - \log(v_{\min}) + \frac{(\log(v_{\max})-\log(v_{\min}))\exp[-\boldsymbol{b}(\log(v_{\max})-\log(v_{\min}))]}{1-\exp[-\boldsymbol{b}(\log(v_{\max})-\log(v_{\min}))]} \qquad \text{(A11)}$$

The cumulative distribution function of $\log(v)$ given in equation (A11) has a restriction of the upper limit to the PPV and is refer to as “bounded”.

Comparison of β computed using equation (A8) and equation (A11) reveals that β calculated using equation (A11) is smaller than that calculated using equation (A8).